NASS
NAN YANG ACADEMY OF SCIENCES

# Earth and Planetary Science

Volume 2 · Issue 1 · April 2023 ISSN 2810-9732

Volume 2 Issue 1 • April 2023 ISSN 2810-9732 (Online)

# Earth and Planetary Science



NASS
NAN YANG ACADEMY OF SCIENCES

NASS
NAN YANG ACADEMY OF SCIENCES

Volume 2 | Issue 1 | April 2023 | Page1-67
Earth and Planetary Science

# Contents

## Editorial



## Research Articles



## Review

Earth and Planetary Science
https://ojs.nassg.org/index.php/eps

RESEARCH ARTICLE

# Hydraulic Flow Unit Characterization in Sandstone Reservoirs, Niger Delta, Nigeria

**Esomchi U. Nwokoma*** **Boniface I. Ijeh** **Chukwunenyoke Amos-Uhegbu**

Department of Physics, College of Physical Science, Micheal Okpara University of Agriculture, Umudike, 02155, Nigeria

ARTICLE INFO

*Article history*
Received: 31 January 2023
Revised: 6 March 2023
Accepted: 21 March 2023
Published Online: 4 April 2023

*Keywords*:
Flow units
Hydraulic units
Modified Lorenz Plot (MLP)
Reservoir

ABSTRACT

The key factor in a successful oil field development plan is understanding the reservoir. The effectiveness of oil extraction is determined by variations in the reservoir, specifically the distribution of porosity and permeability. To create an accurate model of the reservoir, the vertical distribution of its qualities must be determined and separated into flow units, each with its own unique characteristics that affect fluid flow. By identifying these flow units, the preferred flow zones can be discovered. The aim of this study is to identify the number and distribution of hydraulic units, their important characteristics, and the flow performance in two specific wells in the Niger Delta, Nigeria, using the Modified Lorenz Plot (MLP) method. In the hydrocarbon-rich intervals of the wells, a total of 18 flow units were found, with 12 in Well 1 and 6 in Well 2. The number of flow units indicates the level of heterogeneity in the reservoir. This study showed that the Modified Lorenz Plot (MLP) is an efficient and low-cost method for defining petrophysical flow units. This research study aims to transform the conventional approach to reservoir characterization by conducting a thorough analysis of hydraulic flow units in sandstone reservoirs located in the complex geological setting of the Niger Delta, Nigeria. By examining the hydraulic properties of reservoir rocks, the study seeks to gain a better understanding of subsurface fluid flow behavior and the potential for hydrocarbon accumulation.

## 1. Introduction

The Niger Delta region in Nigeria is known for its abundant oil and gas reserves contained in sandstone reservoirs. To optimize production and maximize recovery, it is crucial to understand the flow behavior of fluids within these reservoirs. Hydraulic flow unit characterization is a key tool used in this evaluation, which involves the analysis of the flow properties of subsurface rock formations. This approach helps identify the most permeable zones within a reservoir, which can inform well placement and production strategies [1]. By combining data from various sources, such as well logs, core samples, and seismic sur-

*Corresponding Author:
Esomchi U. Nwokoma,
Department of Physics, College of Physical Science, Micheal Okpara University of Agriculture, Umudike, 02155, Nigeria;
*Email: nwokoma.esomchi@mouau.edu.ng*

DOI: http://dx.doi.org/10.36956/eps.v2i1.808

veys, geologists can gain a comprehensive understanding of the hydraulic flow units within sandstone reservoirs in the Niger Delta. This information is crucial for effective reservoir management and, ultimately, the success of oil and gas operations in the region [2].

The upstream petroleum industry relies on reservoir characterization to gain a comprehensive understanding of the reservoir. The current priority is to enhance these characterization techniques. These advancements are beneficial as they give a more accurate representation of the storage and flow abilities of the petroleum reservoir and significantly decrease the number of residual hydrocarbons [2]. By comprehending essential reservoir features such as pore geometry, tortuosity, and permeability, geologists and engineers can improve reservoir characterization and achieve better reservoir performance and development over time.

Historically, permeability has been evaluated through a linear regression model that assumes a linear relationship between core porosity and permeability [3]. This method fails to account for data dispersion and assumes it's due to measurement errors, ignoring the possibility of high and low permeability zones with similar porosities existing in the same reservoir [4]. Limestone formations with low porosity and high permeability further challenge this assumption [5].

Recognizing these limitations, researchers have shifted their focus to the interdependence of permeability and various depositional characteristics such as grain size, pore geometry, and tortuosity, which are influenced by diagenetic factors like cementation, fracturing, and solution [6]. This calls for a new approach to reservoir characterization that considers geological principles and the physics of fluid flow in porous media [7-9]. The hydraulic flow unit (HFU) approach is proposed as this solution.

An HFU is a rock volume unit with similar fluid flow properties, differentiating it from other units. Unlike lithofacies, which focus on the distribution of lithologies, HFU clusters comparable fluid pathways in the reservoir in [2]. The study on Hydraulic Flow Unit Characterization in Sandstone Reservoirs, Niger Delta, Nigeria, addresses the scientific problem of understanding the distribution of reservoir properties and heterogeneity in sandstone reservoirs, which can impact hydrocarbon production. By accurately characterizing hydraulic flow units, the study seeks to improve field development strategies for the oil and gas industry. This research study aims to examine the impact of various HFUs and RQIs (Reservoir Quality Indicators) on the pressure behavior, flow regimes, and productivity index of horizontal wells in limited reservoirs.

## 2. Regional Geology and General Stratigraphy of the Niger Delta

The research area is within the Niger Delta Basin, which has been extensively studied [10]. The basin is a large delta on the continent's margin that was built out into the Central South Atlantic Ocean during the Eocene near the mouths of the Niger-Benue and Cross River systems [11]. The delta is affected by tides and waves and has sand bodies whose thickness can be altered by growth faulting [12]. It is the world's second-largest delta, with a shoreline that spans over 450 km and ends at the Imo River's mouth [13]. The region spans approximately 20,000 $km^2$ and is known as Africa's largest wetland, including freshwater swamps, mangrove swamps, beaches, bars, and estuaries.

Short and Stauble [10] identified the Benin, Agbada, and Akata formations as three subsurface offshore units in the southern Nigerian sedimentary basin, which includes the Niger Delta (as shown in Figure 1). The surface outcrops of these units are referred to as the Benin Formation, Ogwashi-Asaba Formation, and Ameki Formation.

The geology of the Niger Delta is characterized by thick sedimentary sequences that have been deposited over a long period of time. The deposition of these sediments has been influenced by a variety of factors, including sea-level changes, tectonic activity, and climate change, and most reservoirs in the Niger Delta region are sandstone reservoirs. The sedimentary deposits in the Niger Delta have given rise to a vast amount of hydrocarbon resources, making it an important region for oil and gas exploration and production.

## 3. Methodology

### 3.1 Materials

This study makes use of wireline log data from three wells in an X field in Nigeria's Niger Delta region. The wireline log data from a field in Nigeria's Niger Delta Region, which included Sonic, Neutron, Density Gamma Ray, and Resistivity logs, was utilized to evaluate hydraulic flow units (HFU) in reservoirs in the Niger Delta Region. Because of existing restrictions inside Nigerian oil companies, the precise site of the wells would not be revealed and is referred to as an X-field for secret or security reasons.

The Interactive Petrophysics (IP v. 4.5) advanced interpretation approach is used for data analysis (2018). Shell Petroleum Development Company would provide the data for this project (SPDC).

### 3.2 Porosity

Porosity in good logs refers to the measurement of the

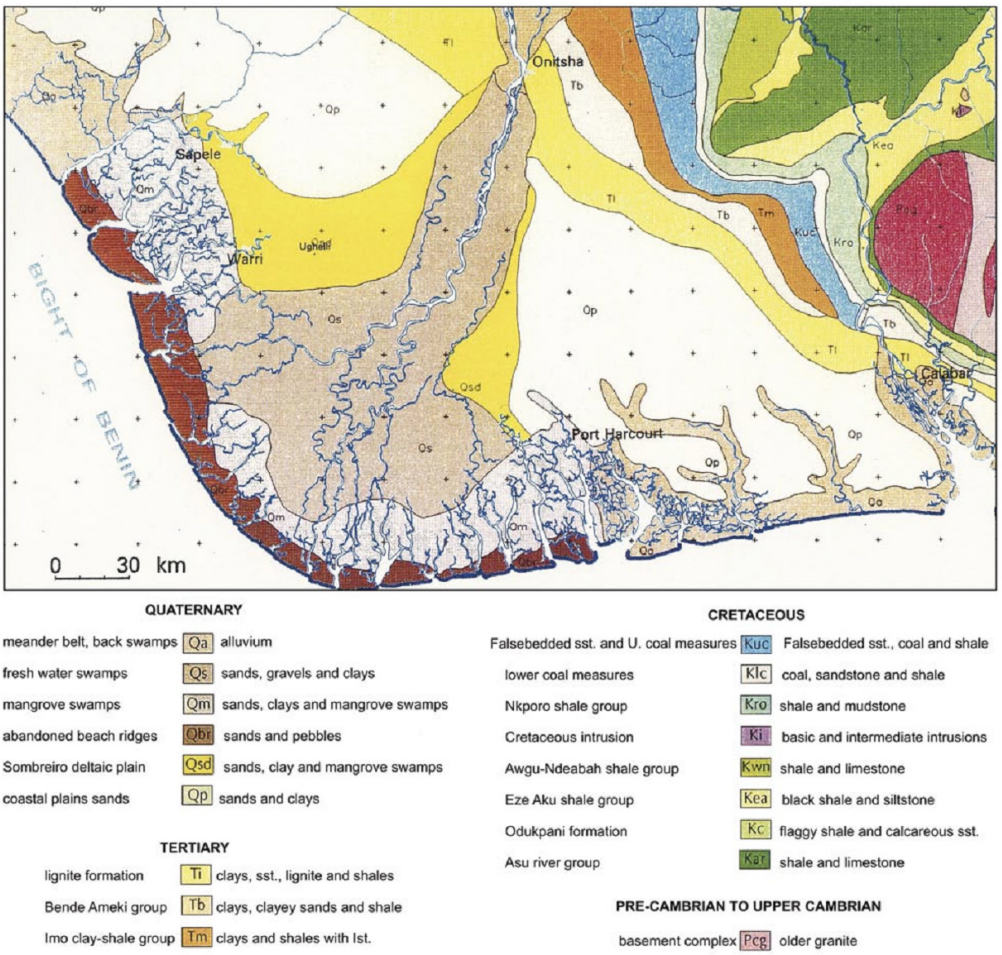


**Figure 1.** Geological map of Niger Delta and its surroundings.

volume of void space or the pore space within subsurface rock formations [14]. It is commonly used in the oil and gas industry to evaluate the potential for hydrocarbon production from a well [2]. Porosity can be measured using various well-logging tools such as neutron, density, and sonic logs [14]. The results of these logs provide a representation of the rock's porosity as a function of depth, allowing geologists to identify permeable formations and make predictions about fluid flow within the subsurface.

Porosity in sands and sandstones is essentially determined by the degree of connectivity of pores, grain size and shape, packing distribution and arrangement, cementation, and clay concentration [14]. To determine porosity, we must simulate a rock sample and calculate the bulk volume and matrix volume.

$$\phi_{sonic} = \frac{\Delta t_{log} - \Delta t_{ma}}{\Delta t_f - \Delta t_{ma}} \quad (1)$$ [2]

$\phi_{sonic}$ = sonic derived porosity in clean formation
$\Delta t_{ma}$ = interval transit time of the matrix
$\Delta t_{log}$ = interval transit time of formation
$\Delta t_f$ = interval transit time of the fluid in the well bore

### 3.3 Permeability

To put it simply, the ease at which fluid can flow through a rock (permeability) is determined by the presence of channels for fluid flow, which is impacted by the rock's qualities such as grain shape and size, pore distribution, and fluid-rock friction. Also, pore spaces can contain more than one fluid, such as gas, oil, and water, and the permeability of each fluid depends on its saturation and properties at varying rates. If there is only one fluid present, the permeability of the rock is at its maximum [2]. When multiple fluids are present in the pore spaces, the permeability of each fluid is called the "effective permeability", and it can differ from each other and not be the same as the permeability of the rock with a single fluid.

Timur equation is given as:

$$K = \frac{0.136\phi^{4.4}}{S_{wi}^2} \quad (2)$$ [2]

where $K$ = permeability
$\phi$ = porosity
$S_{wi}$ = irreducible water saturation

### 3.4 RQI (Reservoir Quality Index)

The Reservoir Quality Index (RQI) is a well-log-based index used to quantify the reservoir quality of a subsurface rock formation. It is calculated using multiple well-log measurements, such as resistivity, porosity, and sonic velocity, which are used to estimate key parameters that affect fluid flow in a reservoir, such as permeability and fluid saturations [1]. The RQI provides a single value that summarizes the reservoir quality of a formation, making it easier to compare different formations and rank them in terms of their potential for hydrocarbon production. The RQI is commonly used in exploration and development efforts to help identify the most prospective areas for further investigation and drilling [2,15].

A method called the reservoir quality indicator (RQI) was introduced by Amaefule et al. [16] to categorize reservoir data into different hydraulic flow units (HFUs) with distinct characteristics. This methodology provides a reliable and efficient way to describe the reservoir.

$$\text{Permeability } K = 1014\,\frac{\phi e^3}{(1-\phi e)^2}\left(\frac{1}{F_S \tau^2 S_{gv}^2}\right) \quad (3)\ [15]$$

They expressed the permeability (k) in terms of effective porosity ($\phi_e$), shape factor ($T_s$) for turosity (t) and surface area per unit grain volume ($S_{gr}$).

The parameters $F_s$ and $\tau$ were grouped into a term called Kozeny constant.

The Kozeny constant is related to the permeability of the rock, which is a measure of how easily fluids can flow through it [15]. The higher the Kozeny constant, the higher the permeability of the rock. In sandstone reservoirs, the Kozeny constant can be used to classify the rocks into different hydraulic flow units (HFUs) based on their permeability and porosity properties.

$$K = 1014\frac{\phi e^3}{\phi_e(1-\phi_e)} \text{ x } \left(\frac{1}{F_S \tau^2 S_N^2}\right) \quad (4)\ [15]$$

$$\sqrt{\frac{K}{\phi e}} = \sqrt{\frac{\sqrt{\phi e^2}}{\sqrt{(1-\phi_e)^2}}} \text{ x } \left(\frac{\sqrt{1}}{\sqrt{F_S \tau^2 S_{gv}^2}}\right) \quad (5)\ [15]$$

$$\sqrt{\frac{K}{\phi_e}} = \frac{\phi e}{(1-\phi e)} \text{ x } \left(\frac{1}{\sqrt{F_S \tau^2 S_{gv}^2}}\right) \quad (6)\ [15]$$

The Reservoir Quality Index (RQI), Pore Volume to Grain Ratio ($\phi e$), and Flow Zone Indicator (FZI) are metrics used in oil and gas exploration and production to evaluate the productivity of hydrocarbon reservoirs. The RQI measures the quality of a reservoir rock based on its permeability and porosity, while the $\phi e$ measures the storage capacity of the rock relative to its grain size [15]. The FZI is a measure of fluid flow properties in the reservoir. These metrics are used together to identify and evaluate potential reservoirs, with a high RQI, high $\phi e$, and high FZI indicating a high-quality reservoir rock with good storage and flow properties, making it a prime target for oil and gas exploration and production [15].

$$RQI = 0.0314\ \sqrt{\frac{K}{\phi e}} \quad (7)\ [2]$$

$$\phi_e = \frac{\phi_e}{1-\phi_e} \quad (8)\ [2]$$

$$\phi_e = \frac{\phi_e}{1-\phi_e} \quad (9)\ [2]$$

Substituting Equations (7), (8) and (9) into related parameters as shape factor, tortuosity and surface area per unit grain volume to the ratio of permeability and effective porosity.

### 3.5 FZI (Flow Zone Indicator)

The Flow Zone Indicator (FZI) is a tool used in well-log analysis to locate permeable zones or flow units within a subsurface formation. It is a computer-generated tool that builds a graphical picture of the rock's permeability using data from many well logs, including resistivity and sonic [2]. The FZI shows places in a hydrocarbon reservoir where fluid flow is expected to happen, which is helpful for identifying probable production zones [17]. The efficiency of hydrocarbon recovery can be increased by optimizing drilling and completion techniques using this information.

The flow zone indicator (FZI) is a valuable tool that connects the flow characteristics of a reservoir between small-scale petroleum physical parameters, such as core plugs, and large-scale measurements, like well bore level. It provides a mathematical representation of flow zones based on surface area and tortuosity [18].

$$FZI = \frac{0.314\sqrt{K/Q}}{\frac{\phi}{1-\phi}} \quad (10)\ [18]$$

where FZI = flow zone indicator, μm
$\phi$ = porosity
K = permeability, mD

### 3.6 Stratigraphic Modified Lorenz Plot (SMLP)

A Stratigraphic Modified Lorenz Plot (SMLP) is a type of well log plot used to visualize and interpret subsurface stratigraphic information from well logs [19]. It is a modified version of the Lorenz plot, a plot that displays the cumulative frequency of values on one axis and the cumulative proportion of values on the other axis [19]. In an SMLP, the cumulative frequency is replaced with the stratigraphic position of the log values, and the cumulative proportion is replaced with the deviation from the mean or

median value of the log data. The plot allows geologists to identify patterns, trends, and anomalies in the subsurface stratigraphic data, which can be used to help inform interpretations of the subsurface geology.

The Lorenz plot is a diagram used in petrophysics to evaluate the heterogeneous nature of a reservoir. The Lorenz coefficient, provides a single metric to gauge the level of heterogeneity based on the reservoir's porosity and permeability [20,21]. The Lorenz coefficient ranges from 0 to 1. The diagram shows the relationship between flow capacity (KH) and storage capacity (H) in a simple manner but does not indicate the spatial distribution of either flow or storage capacity.

## 4. Results

Interactive petrophysics was used for the analysis of petrophysical parameters and the hydraulic flow unit. Microsoft Excel was also used for data analysis and graph plotting.

Water saturation ($S_w$), Volume of Shale ($V_{sh}$), Bulk Volume of Water (BVW), Permeability (k) and Porosity ($\phi$) where the petrophysical parameters estimated in the two wells. The results of the petrophysical and hydraulic parameters are presented in Log panels, graphs and tables. Fractional permeability, fractional porosity, cumulative storage capacity and cumulative flow capacity were the hydraulic flow unit characteristics that were calculated. Alongside RQI and FZI for each flow unit.

Two reservoirs were identified in each of the two wells, based on the sand unit and water saturation values. The hydrocarbon saturation value was inferred from the value of water saturation, where:

$$S_w + S_h = 1 \quad (11)\ [2]$$

$$S_h = 1 - S_w \quad (12)\ [2]$$

where $S_w$ is water saturation and $S_h$ is hydrocarbon saturation.

Figure 2 shows the correlation based on the sand units and saturation properties. The identified reservoirs in the two wells are between 9976 ft to 12123 ft and net pay zone is between 33 ft to 63.4 ft.

The reservoirs in Well 1, have a net pay zone between 37-63.5 ft as seen in Figure 3 and Table 1. The mean gamma ray values (57.342-57.540 gAPI) correspond to the values of the Volume of Shale (0.394-0.396) indicative of sand units. The resistivity values of the reservoir for Well 1 are between 4.106-45.552 Ohmm. This shows a low value of resistivity corresponding to high hydrocarbon saturation and low water saturation. The mean Bulk Volume of Water in the reservoirs in Well 1 is between 0.082-0.137. The porosity is seen to decrease with depth in Well 1. The porosity values for the reservoirs in Well 1 are between 0.154-0.274, which fall within the range of a good porosity reservoir. The reservoirs are highly permeable, having permeability values ranging from 6.987 mD to 1180.531 mD. In Well 1, the reservoirs are between 9976-10012.5 ft.

The modified Lorenz plot for reservoir 1 is shown in Figure 4. Seven (7) flow units were identified in reservoir 1.

The reservoirs in Well 2, have a net pay zone between

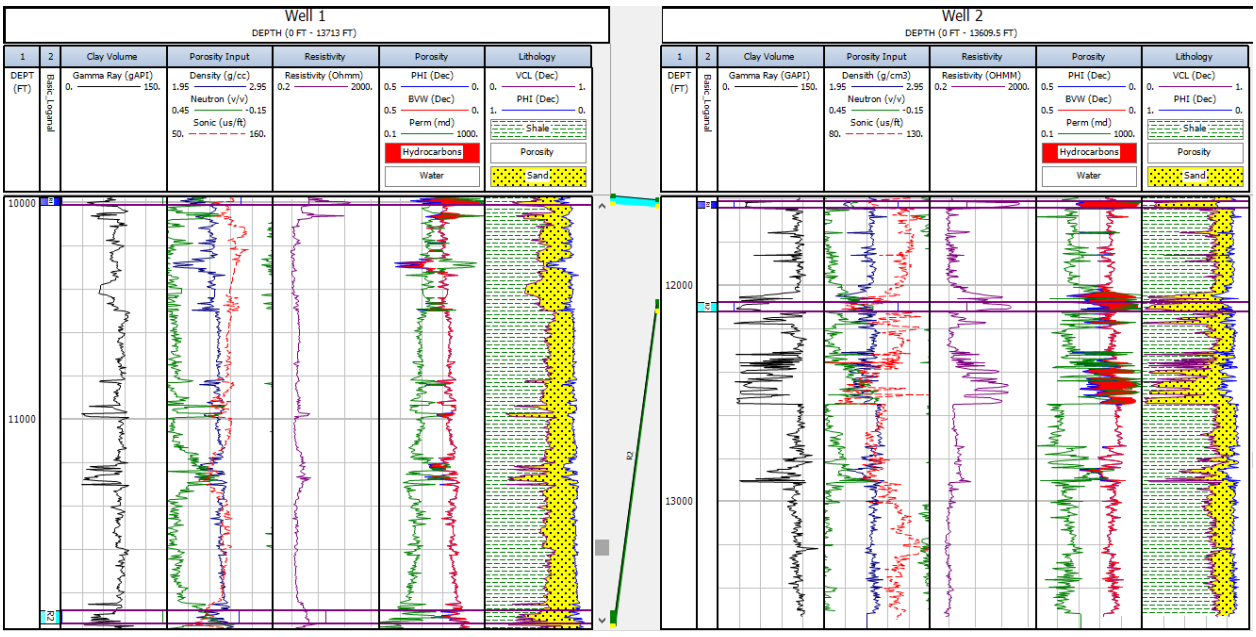


**Figure 2.** Composite well for well tie for the two wells.

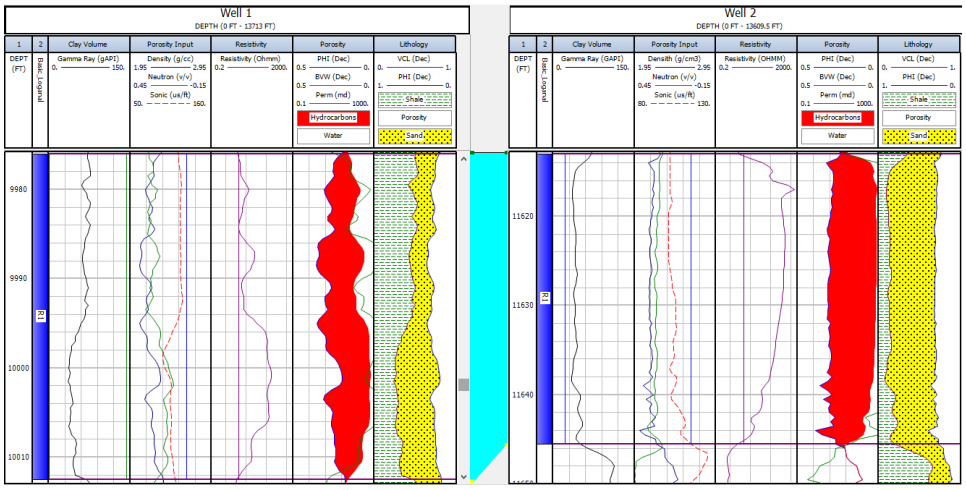


**Figure 3.** Composite well for (a) Well 1 reservoir 1 (b) Well 2 reservoir 1.

**Table 1.** Petrophysical properties of the two reservoirs in Well 1.

| **Well / Reservoir** | | **Top:9976 ft, Bottom: 10012.5 ft, Net: 37 ft** | | | **Top: 11882 ft, Bottom: 11944.5 ft, Net: 63.5 ft** | | |
|---|---|---|---|---|---|---|---|
| Curve | Units | Min | Max | Mean | Min | Max | Mean |
| Bulk Volume of Water | Dec | 0.024 | 0.167 | 0.082 | 0.062 | 0.198 | 0.137 |
| Density | g/cc | 2.062 | 2.358 | 2.198 | 2.221 | 2.54 | 2.387 |
| Gamma Ray | gAPI | 35.74 | 77.278 | 57.54 | 31.118 | 88.169 | 57.342 |
| Neutron | v/v | 0.129 | 0.337 | 0.242 | 0.062 | 0.356 | 0.211 |
| Permeability | md | 4.753 | 5989.262 | 1180.531 | 0.043 | 46.567 | 6.987 |
| Porosity | Dec | 0.177 | 0.356 | 0.274 | 0.062 | 0.255 | 0.154 |
| Resistivity | Ohmm | 3.605 | 171.457 | 45.553 | 2.55 | 8.499 | 4.106 |
| Sonic | us/ft | 93.894 | 120.684 | 111.352 | 67.07 | 100 | 88.262 |
| Water Saturation | Dec | 0.094 | 0.941 | 0.311 | 0.662 | 1 | 0.92 |
| Volume of Shale | Dec | 0.241 | 0.536 | 0.396 | 0.208 | 0.613 | 0.394 |

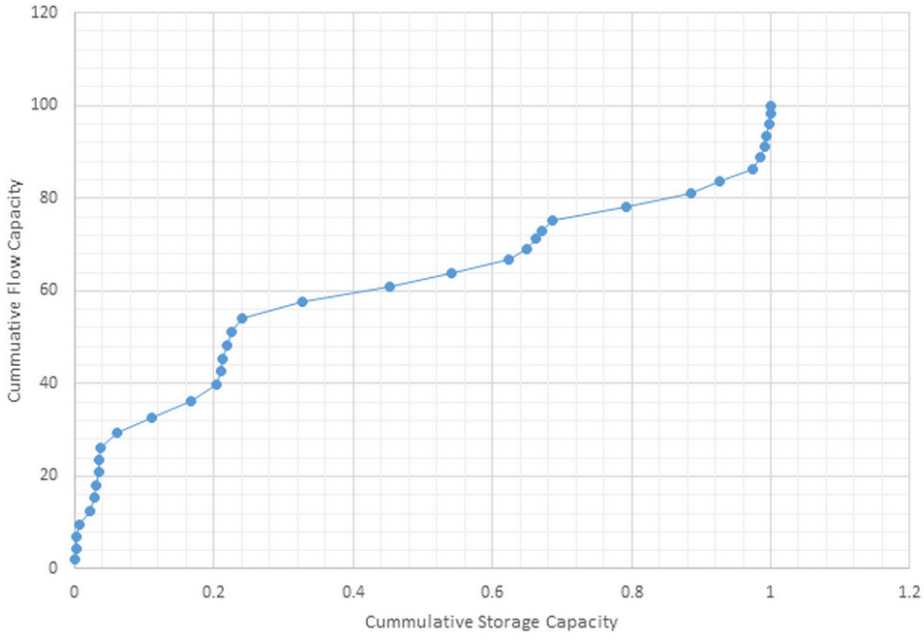


**Figure 4.** Modified Lorenz plot for reservoir 1, Well 1.

33-44 ft as seen in Figure 5 and Table 2. The mean gamma ray values (42.774-45.683 gAPI) correspond to the values of the Volume of Shale (0.148-0.170) indicative of sand units. The resistivity values of the reservoir for Well 1 are between 106.605-259.063 Ohmm. This shows a low value of resistivity corresponding to high hydrocarbon saturation and low water saturation. The mean Bulk Volume of Water in the reservoirs in Well 1 is between 0.038-0.049. The porosity is seen to decrease with depth in the Well 1. The porosity values for the reservoirs in the Well 1 are between 0.201-0.301, which fall within the range of a good porosity reservoir. The reservoirs are highly permeable, having permeability values ranging from 661.540 mD to 10541.705 mD. In Well 1, the reservoirs are between 11613-12123 ft.

The modified Lorenz plot for reservior 1 is shown in Figure 6, while Table 3, shows hdraulic flow units paprameters for well 1 reservior 1. Figure 7 shows the modified Lorenz plot for reservoir 2. Four (4) flow units were identified in reservoirs 2.

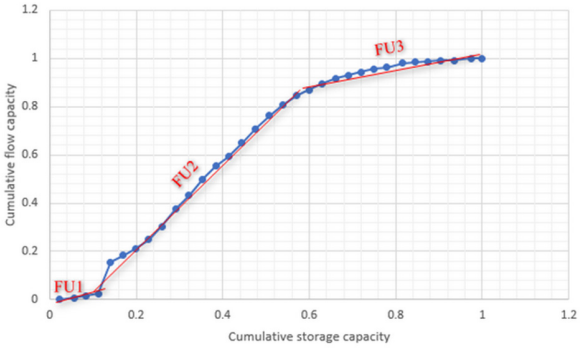


**Figure 6.** Modified Lorenz plot for reservoir 1, Well 2.

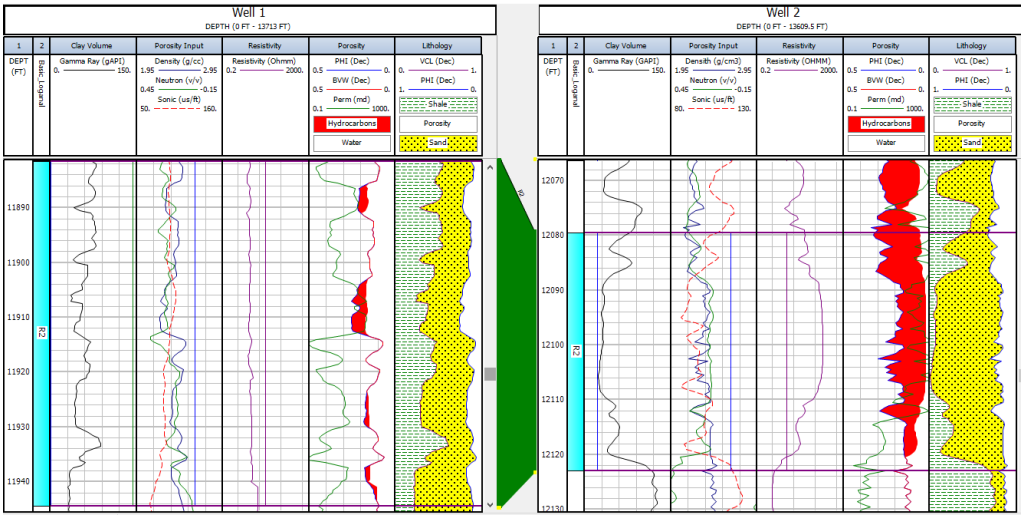


**Figure 5.** Composite well for (a) Well 1 reservoir 2 (b) Well 2 reservoir 2.

**Table 2.** Petrophysical properties of the two reservoirs in Well 2.

| **Well / Reservoir** | | **Top: 11613 ft, Bottom: 11645.5 ft, Net: 33 ft** | | | **Top: 12080 ft, Bottom: 12123 ft, Net: 44 ft** | | |
|---|---|---|---|---|---|---|---|
| Curve | Units | Min | Max | Mean | Min | Max | Mean |
| Bulk Volume of Water | Dec | 0.008 | 0.209 | 0.038 | 0.021 | 0.208 | 0.049 |
| Density | g/cm$^3$ | 2.010 | 2.268 | 2.154 | 2.111 | 2.49 | 2.318 |
| Gamma Ray | GAPI | 33.885 | 70.51 | 42.774 | 24.38 | 116.69 | 45.683 |
| Neutron | v/v | 0.243 | 0.356 | 0.287 | 0.153 | 0.440 | 0.227 |
| Permeability | mD | 20.010 | 46269.836 | 10541.705 | 0.299 | 8097.911 | 661.546 |
| Porosity | Dec | 0.231 | 0.388 | 0.301 | 0.097 | 0.327 | 0.201 |
| Resistivity | OHMM | 2.283 | 1495.330 | 259.063 | 1.268 | 224.667 | 106.605 |
| Sonic | us/ft | 100.939 | 114.659 | 103.968 | 85.943 | 115.888 | 96.844 |
| Water Saturation | Dec | 0.028 | 0.826 | 0.13 | 0.072 | 1.000 | 0.277 |
| Volume of Shale | Dec | 0.082 | 0.354 | 0.148 | 0.012 | 0.697 | 0.170 |

**Table 3.** Hydraulic flow unit for reservoir 1, Well 1.

| Depth | K | Porosity | Fractional Permeability | Fractional Porosity | Cumulative storage capacity | Cumulative flow capacity | Cumulative storage capacity | Cumulative flow capacity | RQI | FZI |
|---|---|---|---|---|---|---|---|---|---|---|
| 9976 | 13.1262 | 0.2042 | 0.0003 | 0.0202 | 0.0202 | 0.0003 | 2.0157 | 0.0300 | 2.5175 | 9.8111 |
| 9977 | 62.4081 | 0.2491 | 0.0014 | 0.0246 | 0.0447 | 0.0017 | 4.4746 | 0.1726 | 4.9701 | 14.9821 |
| 9978 | 65.0172 | 0.2527 | 0.0015 | 0.0249 | 0.0697 | 0.0032 | 6.9690 | 0.3213 | 5.0366 | 14.8947 |
| 9979 | 141.3055 | 0.2667 | 0.0032 | 0.0263 | 0.0960 | 0.0064 | 9.6016 | 0.6442 | 7.2277 | 19.8727 |
| 9980 | 666.4240 | 0.3085 | 0.0152 | 0.0305 | 0.1265 | 0.0217 | 12.6468 | 2.1675 | 14.5941 | 32.7125 |
| 9985 | 95.0038 | 0.2667 | 0.0022 | 0.0263 | 0.2605 | 0.0377 | 26.0537 | 3.7702 | 5.9264 | 16.2947 |
| 9986 | 1002.5278 | 0.3448 | 0.0229 | 0.0340 | 0.2946 | 0.0606 | 29.4573 | 6.0616 | 16.9315 | 32.1737 |
| 9987 | 2175.3958 | 0.3382 | 0.0497 | 0.0334 | 0.3280 | 0.1103 | 32.7957 | 11.0340 | 25.1833 | 49.2794 |
| 9988 | 2523.7854 | 0.3509 | 0.0577 | 0.0346 | 0.3626 | 0.1680 | 36.2595 | 16.8026 | 26.6296 | 49.2598 |
| 9989 | 1577.9307 | 0.3467 | 0.0361 | 0.0342 | 0.3968 | 0.2041 | 39.6818 | 20.4092 | 21.1834 | 39.9168 |
| 9990 | 271.3282 | 0.2988 | 0.0062 | 0.0295 | 0.4263 | 0.2103 | 42.6312 | 21.0294 | 9.4621 | 22.2049 |
| 9997 | 3862.6177 | 0.2939 | 0.0883 | 0.0290 | 0.6381 | 0.5417 | 63.8136 | 54.1654 | 35.9974 | 86.4843 |
| 9998 | 3548.2642 | 0.2927 | 0.0811 | 0.0289 | 0.6670 | 0.6228 | 66.7029 | 62.2757 | 34.5721 | 83.5424 |
| 9999 | 1137.1512 | 0.2430 | 0.0260 | 0.0240 | 0.6910 | 0.6487 | 69.1015 | 64.8749 | 21.4801 | 66.9153 |
| 10000 | 612.5842 | 0.2085 | 0.0140 | 0.0206 | 0.7116 | 0.6628 | 71.1597 | 66.2751 | 17.0200 | 64.6107 |
| 10001 | 413.8050 | 0.1952 | 0.0095 | 0.0193 | 0.7309 | 0.6722 | 73.0865 | 67.2209 | 14.4573 | 59.6068 |
| 10002 | 571.0463 | 0.2139 | 0.0131 | 0.0211 | 0.7520 | 0.6853 | 75.1979 | 68.5261 | 16.2241 | 59.6248 |
| 10003 | 4651.8062 | 0.3048 | 0.1063 | 0.0301 | 0.7821 | 0.7916 | 78.2066 | 79.1588 | 38.7912 | 88.4765 |
| 10004 | 4125.7285 | 0.2939 | 0.0943 | 0.0290 | 0.8111 | 0.8859 | 81.1077 | 88.5890 | 37.2032 | 89.3813 |
| 10005 | 1797.7697 | 0.2564 | 0.0411 | 0.0253 | 0.8364 | 0.9270 | 83.6387 | 92.6981 | 26.2929 | 76.2534 |
| 10006 | 2065.7144 | 0.2648 | 0.0472 | 0.0261 | 0.8625 | 0.9742 | 86.2525 | 97.4197 | 27.7336 | 77.0005 |
| 10007 | 498.2383 | 0.2539 | 0.0114 | 0.0251 | 0.8876 | 0.9856 | 88.7588 | 98.5586 | 13.9097 | 40.8744 |
| 10008 | 211.0224 | 0.2467 | 0.0048 | 0.0244 | 0.9119 | 0.9904 | 91.1940 | 99.0409 | 9.1835 | 28.0419 |
| 10009 | 162.0880 | 0.2388 | 0.0037 | 0.0236 | 0.9355 | 0.9941 | 93.5512 | 99.4114 | 8.1807 | 26.0767 |
| 10010 | 170.8218 | 0.2376 | 0.0039 | 0.0235 | 0.9590 | 0.9980 | 95.8966 | 99.8018 | 8.4193 | 27.0156 |
| 10011 | 78.2902 | 0.2309 | 0.0018 | 0.0228 | 0.9818 | 0.9998 | 98.1758 | 99.9808 | 5.7819 | 19.2588 |

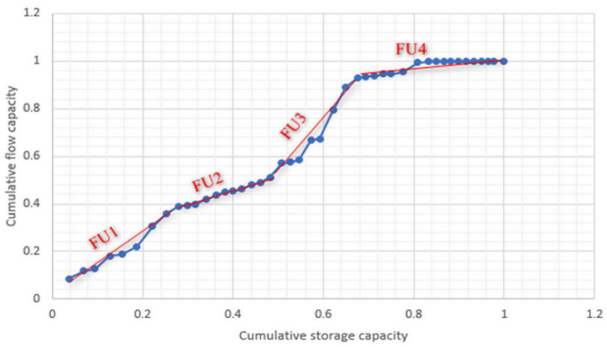


**Figure 7.** Modified Lorenz plot for reservoir 2, Well 2.

## 5. Discussion

In this study, two wells (Well 1 and Well 2) were investigated to evaluate their respective hydrocarbon reservoirs. The results indicate that Well 1 has a net pay zone ranging from 37 feet to 63.5 feet, while Well 2 has a net pay zone ranging from 33 feet to 44 feet. The net pay zone refers to the thickness of the rock formation that contains hydrocarbons and can be economically produced.

The gamma-ray values for both wells show values that correspond to sand units, as indicated by the volume of shale values ranging from 0.394 to 0.396 for Well 1 and from 0.148 to 0.170 for Well 2. These results suggest that both wells contain sandstone reservoirs, which are known to be good reservoirs for hydrocarbons due to their high porosity and permeability. The resistivity values for Well 1 range from 4.106 Ohmm to 45.552 Ohmm, indicating high hydrocarbon saturation and low water saturation. A similar trend is observed in Well 2, with resistivity values ranging from 106.605 Ohmm to 259.063 Ohmm. These results suggest that both wells have a high potential for

producing hydrocarbons.

The bulk volume of water in both wells ranges from 0.038 to 0.137 for Well 1 and from 0.038 to 0.049 for Well 2. This indicates that the water saturation in both wells is relatively low, further supporting the potential for hydrocarbon production. The porosity values for both wells decrease with depth, with values ranging from 0.154 to 0.274 for Well 1 and from 0.201 to 0.301 for Well 2. Despite the decrease in porosity with depth, the values fall within the range of a good porosity reservoir. The permeability values for both wells are high, ranging from 6.987 mD to 1180.531 mD for Well 1 and from 661.540 mD to 10541.705 mD for Well 2. This suggests that both wells have good flow properties, further supporting the potential for hydrocarbon production.

The modified Lorenz plot was used to identify flow units within the reservoirs. Three flow units were identified in reservoir 1, and four flow units were identified in reservoir 2, as shown in Figures 6 and 7, respectively. These flow units are important for characterizing the reservoirs and understanding the fluid flow properties within them. Overall, the results suggest that both wells have good potential for producing hydrocarbons.

## 6. Conclusions

In summary, this study aimed to characterize hydraulic flow units in sandstone reservoirs located in the Niger Delta region of Nigeria using well-log data and the Modified Lorenz Plot (MLP) method. Four hydrocarbon-rich intervals from two wells were evaluated, and the analysis revealed variations in reservoir properties, including thickness, porosity, and permeability. The number of flow units determined the level of heterogeneity in the reservoir, with a greater number indicating more challenges in hydrocarbon production. The ultimate goal of identifying flow units is to enhance our understanding of reservoir behavior and minimize uncertainties in field development economics.

Two wells were evaluated using well log data that had four hydrocarbon-rich intervals. The analysis showed the thickness of the reservoirs varied from 33 ft to 63.5 ft, with porosity ranging from 15.4% to 35.6% and permeability from 6.987 mD to 1054.17 mD. The Modified Lorenz Plots (MLP) were used to define flow units based on the slope inflection of flow capacity. Well 1 had 12 flow unit intervals with a thickness of 37 ft to 63.5 ft, while Well 2 had 6 flow units with a thickness of 33 ft to 44 ft. More flow unit intervals indicate greater heterogeneity in the reservoir, leading to poor hydrocarbon production.

The MLP method proved to be a reliable and cost-effective approach for defining petrophysical flow units. Well 1 had 12 flow unit intervals, while Well 2 had 6, suggesting a higher level of heterogeneity in Well 1. Overall, the study contributes valuable insights into the hydraulic flow unit characterization of sandstone reservoirs in the Niger Delta region of Nigeria and can potentially aid in the optimization of field development strategies for the oil and gas industry.

## Authors Contributions

The research was a collaborative effort, with Boniface I. Ijeh responsible for drafting the protocol and Esomchi U. Nwokoma designing the study. The initial draft of the manuscript was written by Chukwunenyoke Amos-Uhegbu and Esomchi U. Nwokoma. Esomchi U. Nwokoma supervised the field investigation, while Boniface I. Ijeh and Chukwunenyoke Amos-Uhegbu carried out the analysis of the geophysical data. Chukwunenyoke Amos-Uhegbu also oversaw the literature searches. All authors read and approved the final manuscript.

## Conflicts of Interest

There is no conflict of interest.

## References

[1] Stolz, A.K., Graves, R.M., 2003. Sensitivity study of flow unit fefinition by use of reservoir simulation. SPE Annual Technical Conference and Exhibition; 2003 Oct 5-8; Denver, Colorado. p. SPE-84277-MS. DOI: https://doi.org/10.2118/84277-MS

[2] Onuh, H.M., David, O.O., Onuh, C.Y., 2016. Modified reservoir quality indicator methodology for improved hydraulic flow unit characterization using the normalized pore throat methodology (Niger Delta field as case study). Journal of Petroleum Exploration and Production Technology. 7(2), 409-416. DOI: http://dx.doi.org/10.1007/s13202-016-0297-8

[3] Lawal, K.A., Onyekonwu, M.O., 2005. A robust approach to Flow Unit Zonation: SPE Paper 98830. Society of Petroleum Engineers: Richardson. pp. 15.

[4] Khalid, M., Desouky, S.E.D., Rashed, M., et al. 2019. Application of hydraulic flow units' approach for improving reservoir characterization and predicting permeability. Journal of Petroleum Exploration and Production Technology. 10(2), 467-479. DOI: http://dx.doi.org/10.1007/s13202-019-00758-7

[5] Ebanks, W.J., 1987. Flow Unit Concept-Integrated Approach for Engineering Projects. AAPG Annual Meeting, AAPG Bulletin. 71(5), 551-552.

[6] Soto B.R., Torres, F., Arango, S., et al., 2001. Improved reservoir permeability models from flow units

and soft computing techniques: A case study, Suria and Reforma-Libertad Fields, Colombia; 2001 Mar 25-28; Buenos Aires, Argentina. p. SPE-69625-MS. DOI: http://dx.doi.org/10.2118/69625-ms

[7] Svirsky, D., Ryazanov, A., Pankov, M., et al. (editors), 2004. Hydraulic flow units resolve reservoir description challenges in a Siberian oil field. Proceedings, Society of Petroleum Engineers Asia Pacific Conference on Integrated Modeling and Asset Management; 2004 Mar 29-30. Kuala Lumpur, Malaysia. p. 15.

[8] Fang, Y., Yang, E., Guo, S., et al., 2022. Study on micro remaining oil distribution of polymer flooding in Class-II B oil layer of Daqing Oilfield. Energy. 254, 124479. DOI: https://doi.org/10.1016/j.energy.2022.124479

[9] Zhong, H., He, Y., Yang, E., et al., 2022. Modeling of microflow during viscoelastic polymer flooding in heterogenous reservoirs of Daqing Oilfield. Journal of Petroleum Science and Engineering. 210, 110091. DOI: https://doi.org/10.1016/j.petrol.2021.110091

[10] Short, K.C., Stauble, A.J., 1967. Outline of geology of Niger Delta. American Association of Petroleum Geologists Bulletin. 51, 761-779.

[11] Hospers, J., 1965. Gravity field and structure of the Niger Delta, Nigeria, West Africa. Geological Society of American Bulletin. 76, 407-422.

[12] Avbovbo, A.A., 1978. Tertiary lithostratigraphy of Niger Delta. American Association of Petroleum Geologists Bulletin. 62, 295-300.

[13] Awosika, L.F., 1995. Impacts of global climate change and sea level rise on coastal resources and energy development in Nigeria. Global Climate Change: Impact on Energy Development DAM TECH Nigeria Limited.

[14] Tiab, D., Donaldson, E.C., 2012. Petrophysics. Elsevier: Netherlands. pp. 85-219. DOI: http://dx.doi.org/10.1016/b978-0-12-383848-3.00003-7

[15] Nooruddin, H.A., Hossain, M.E., 2011. Modified Kozeny-Carmen correlation for enhanced hydraulic flow unit characterization. Journal of Petroleum Science and Engineering. 80(1), 107-115. DOI: https://doi.org/10.1016/j.petrol.2011.11.003

[16] Amaefule, J.O., Altunbay, M., Tiab, D., et al., 1993. Enhanced reservoir description: Using core and log data to identify hydraulic (flow) units and predict permeability in uncored intervals/wells. 1993 SPE Annual Technical Conference and Exhibition; 1988 Oct 3-6; Houston, TX. p. SPE-26436-MS. DOI: https://doi.org/10.2118/26436-MS

[17] Al-Dhafeeri, A . M., Nasr-El-Din, H.A., 2007. Characteristics of high-permeability zones using core analysis, and production logging data. Journal of Petroleum Science Engineering. 55(1-2), 18-36. DOI: https://doi.org/10.1016/j.petrol.2006.04.019

[18] Ross-Coss, D., Ampomah, W., Cather, M., et al. (editors), 2016. An improved approach for sandstone reservoir characterization. SPE Western Regional Meeting; 2016 May 23-26; Anchorage, Alaska, USA. p. SPE-180375-MS. DOI: https://doi.org/10.2118/180375-ms

[19] Mahjour, S.K., Al-Askari, M.K.G., Masihi, M., 2016. Flow-units verification, using statistical zonation and application of Stratigraphic Modified Lorenz Plot in Tabnak gas field. Egyptian Journal of Petroleum. 25(2), 215-220. DOI: https://doi.org/10.1016/j.ejpe.2015.05.018

[20] Doorwar, S., Purswani, P., Ambastha, A., et al., 2020. Application of tracer-based workflow for calibrating reservoir heterogeneity. SPE Reservoir Evaluation & Engineering. 24(03), 603-618. DOI: https://doi.org/10.2118/200374-pa

[21] El-Deek, I., Abdullatif, O., Korvin, G., 2017. Heterogeneity analysis of reservoir porosity and permeability in the Late Ordovician glacio-fluvial Sarah Formation paleovalleys, central Saudi Arabia. Arabian Journal of Geosciences. 10(18). DOI: https://doi.org/10.1007/s12517-017-3146-2

Earth and Planetary Science
https://ojs.nassg.org/index.php/eps

RESEARCH ARTICLE

# Curie Depth and Surface Heat Flow Estimation from Anomalous Magnetic Blocks in the Lower and Part of Middle Benue Trough and Anambra Basin

**Mukaila Abdullahi[1*] Yunis B. Valdon[2] Fartisincha P. Andrew[1] Bello Yusuf Idi[1]**

1. Department of Science Laboratory Technology, Modibbo Adama University, P.M.B. 2076, Yola, Nigeria
2. Department of Geology, Modibbo Adama University, P.M.B. 2076, Yola, Nigeria

ARTICLE INFO

*Article history*
Received: 28 February 2023
Revised: 7 April 2023
Accepted: 18 April 2023
Published Online: 23 April 2023

*Keywords*:
Curie depth
Surface heat flow
Geothermal energy
Magnetic data
Benue trough

ABSTRACT

Estimation of the bottom (Curie) depths and SHF values on blocks (A, B, C, …, Y) of magnetic anomalies in the lower and part of the middle Benue trough and Anambra basin have been presented. A Map of the result shows a shallow Curie depth of about 11 km around the area of Abakaliki with the deepest Curie depth of about 27 km obtained around Utukpa region. The overriding bottom (Curie) depth of 18 km is calculated around Iku mbur, Arufu and Igumale regions. Heat flow has also been calculated from the Curie depth results. The SHF vary from 54 $mWm^{-2}$ around Utukpa to the highest value of 132 $mWm^{-2}$ around Abakaliki. The obtained high SHF value could be of sufficiently good prospects for the exploration of geothermal energy resources in the region.

## 1. Introduction

Thermal anomaly is a manifestation of renewable and environmentally benign green geothermal energy resources. Geothermal studies are carried out based on magnetic anomaly [1-10]. Curie point depth/Curie depth is the point depth at which the magnetic sources at a particular geographic location within the Earth's crust lose their magnetism contents completely at a specific temperature known as the Curie point temperature [11].

The Curie (magnetic bottom) depths are often derived and computed from magnetic anomalies on the basis of spectral analysis [2,8-10,12-19]. Modification of the conventional spectral method was made for a robustly new method

*Corresponding Author:
Mukaila Abdullahi,
Department of Science Laboratory Technology, Modibbo Adama University, P.M.B. 2076, Yola, Nigeria;
*Email: mukailaa.agp@mau.edu.ng*

DOI: http://dx.doi.org/10.36956/eps.v2i1.821

called 'the centroid method' as presented [8,10,20,21].

Whereas, Surface Heat Flow (SHF) is the movement of heat energy from the interior part of the Earth to the surface. It can generally be estimated from the Curie depths using 1-D Fourier law based on heat transfer through conduction mode [2]. The process happens during the cooling of the Earth's core and the generation of radiogenic heat energy between 20 km and 40 km of the Earth's upper crust [19]. SHF is usually higher in the areas of high tectonic activity and thinner Earth's crust [19].

The Nigerian Benue trough despite a number of quantitative geothermal research based on magnetic anomalies in the region [20,22-27], which suggested Curie depths between 11 km and 33 km, SHF values between 51 $mWm^{-2}$ and 132 $mWm^{-2}$, there are still more to be interpreted about the geodynamic process of the region in terms of these values.

In the present study therefore, the computed Curie depths using modified centroid method were used in the calculation of SHF using 1-D Fourier's law in the study region.

## 2. Geological Formations and Tectonics of the Region

The Benue trough (Figure 1) is a mega rifted system for many forms of Earth sciences research [28-37]. The sedimentary rocks beneath the region under study are the Asu River Group, which comprises Albian marine shales and limestones with sandstone intercalations that formed the oldest formation beneath the region.

Asu River Group is observed around the areas of Abakaliki, Iku mbur, Ugba, Oturkpo and somewhere around the east of Ebeel area (Figure 2). The Cenomanian-Turonian Eze-Aku formation consists of the blackshales, siltstones and calcareous sandstones. The Awgu formation is a coal-bearing formation of the Late Turonian-Early Santonian. The Nkporo formation comprises the shales and mudstone of the Coniacian/Maestrichtian depositional cycle. Exposure of Nkporo formation is observed around the village of Otukpa area of Enugu (Figure 2). Bassange formation is composed of the sandstones and ironstones, which are also of the Coniacian/Maestrichtian depositional cycle. This formation (Bassange) is sandwiched between the Nkporo and Awgu shales (Figure 2). The lower coal formation comprising coal, sandstones and shales is overlain by the Nkporo formations in the Anambra basin. The Nsukka formation comprises the false-bedded sandstones that mark yet another transgression in the Anambra basin during the Paleocene [34,35]. Understanding the basement setup on the basis of gravity and magnetic anomalies in the region has been reported [36-39].

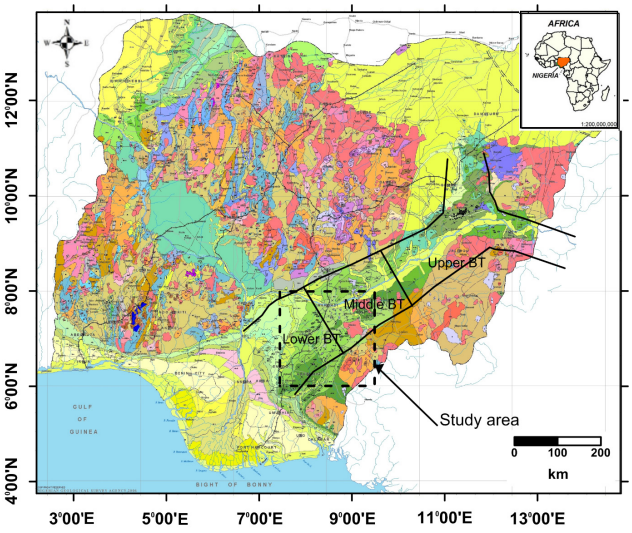


**Figure 1.** Geological map of Nigeria showing the NE-SW Benue trough, sub-divisions and location of study.

Interpretation of computed Curie depths has been done in terms of the different rock types found in the area [39]. The different basement rock types are; the Precambrian granites and gneisses [36,37,40,41]. Both the Cretaceous and Tertiary-recent sediments have been intruded by igneous intrusions [39].

Anticlinal axes within the sedimentary section have also been identified and interpreted in the region [38,40,42,43]. The intruded igneous rocks (Tertiary volcanic) and the anticlinal axes (Santonian) account for the shallow basement as well as the thinner crust in the region [28,29,31].

## 3. Data and Methodology

The aeromagnetic data presented in this work are part of the Nigeria's nation-wide high-resolution geophysical data project [36,39]. The high-resolution aeromagnetic data are obtained from the Nigerian Geological Survey Agency (NGSA) flown between 2006 and 2007 by Fugro Airborne Survey. The data acquisition was done on the basis of the dominant NE-SW regional strike (i.e., parallel to the orientation of the Benue trough). The traverse line spacing was set at 500 m and 2 km control line. The data were recorded 80 m above the ground's surface every 0.1 s. Figure 3 shows the reduced-to-the-magnetic-pole (RTP) of the TMI of the area. The RTP is obtained at a geomagnetic inclination of 15°, geomagnetic declination of 2° and amplitude correction of 40 m. On the map, the magnetic highs and lows were identified and interpreted in other reported research [36].

Depth calculation from susceptibility studies based on borehole data is more accurate and reliable [18,44-47]. Scaling of geology from the magnetization point of view showed that power law: $\varphi_m(l_x, l_y) \propto l^{-\beta}$ [48-52], where, $\varphi_m$ stands for

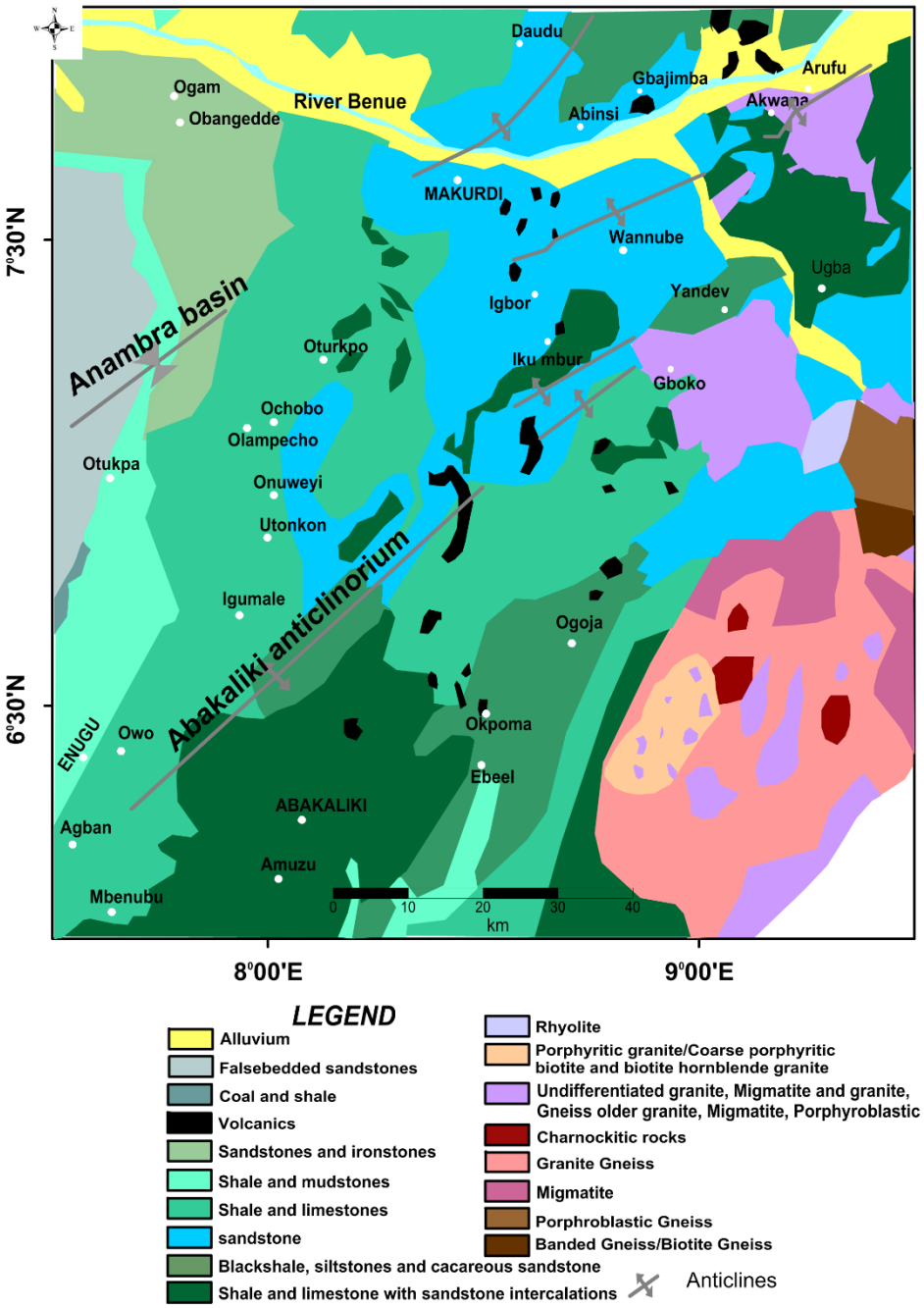


**Figure 2.** The geology and major structural features (anticlines) 68 of the study area.

magnetization power spectra, $l_x$ and $l_y$ are the wavenumbers in the **x** and **y** directions and their Euclidean norm $k = \sqrt{l_x^2 + l_y^2}$ measured in rad/km, and $\beta$ represents the scaling exponent which described the non-homogeneity of sources in a region [36,47,52].

The top depth ($Z_t$) of an anomalous body in terms of magnetic field ($\Phi_t(l)$) of 1-D radially averaged power spectrum is calculated as follows [7]:

$$\ln\left(\Phi_t(l)\right) = A_1 - 2lZ_t - \beta * \ln(l) \quad (1)$$

where $A_1$ is a constant.

Whereas, centroid depth ($Z_0$) of the anomalous magnetic body is as follows [8,10]:

$$\ln\left(\frac{\Phi_t(l)}{l^2}\right) = A_2 - 2lZ_0 - \beta * \ln(l) \quad (2),$$

where $A_2$ is a constant, which depends upon the magnetization of source body.

A combination of the two equations was used and computed for the bottom (i.e., Curie) depths ($Z_b$) as follows [2]:

$$Z_b = 2Z_0 - Z_t \quad (3)$$

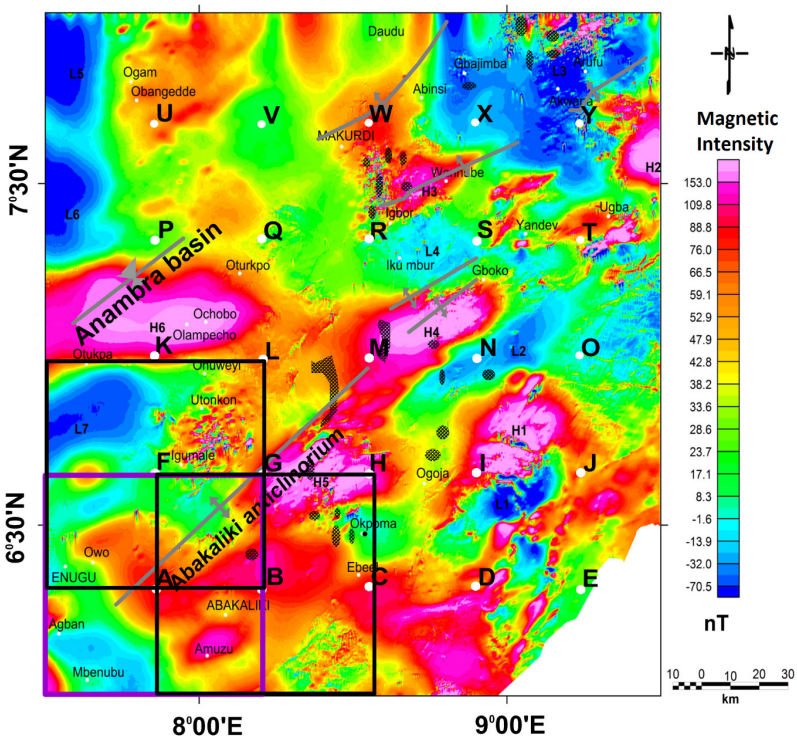


**Figure 3.** RTP-TMI anomaly map of the study area. Centers of block (A – Y) are shown in white dots for estimation of bottom magnetic (Curie) depths as well as the surface heat flow values (SHF) underneath the study area. Every block is 50% overlapped over the other as shown.

Because of the non-consistency in results of the simultaneous estimation of depths and scaling exponent (**β**) values [17,18,53] using Equations (1) and (2), for which others are of the option that scaling exponent (**β**) be given a constant value for a region of common geology [9,51,52]. Fixed fractal parameter (scaling exponent, **β**) of unity was used [39] on the basis of publication [20] and calculated the top ($Z_t$) depths (km) and centroid ($Z_0$) depths (km) from each of the power spectral blocks (A, B, C, …, Y) of the magnetic anomaly of the study area.

Curie depth ($Z_b$) results have been used in the estimation of SHF values for the study area [2], using the 1-D Fourier law based on a conductive mode of heat transfer [54]. The Fourier law works where there is no heat transportation by mode of convection, no radiogenic heat and constant temperature gradient (dT/dz). Empirically, the Fourier law [54], can be written as:

$$q_s = k\frac{dT}{dz} \tag{4}$$

where, $q_s$ stands for SHF, k is thermal conductivity (W/m°C) which depends upon the lithology, temperature and pressure. The average thermal conductivity for the region is 2.5 W/m°C [39]. The Curie temperature is written as a function of temperature gradient and Curie depth as follows [54]:

$$\theta_c = (\frac{dT}{dz})Z_b \tag{5}$$

From the above Equations (4) and (5), the SHF can be derived as:

$$q_s = \frac{k\theta_c}{Z_b} \tag{6}$$

Here, Curie temperature of $\theta_c$ =580°$C$ is used in the calculations of SHF in the region.

## 4. Results and Discussion

Figure 4 shows the power spectrum of block (C) and the calculated top, centroid and bottom depths of magnetic body.

Detailed results of the Curie depths as well as the computed SHF values in all of the blocks (A, B, C, …, Y) are shown in Table 1.

The interpretation of geophysical data because of ambiguity, is usually constrained on the basis of geological formations found in the region or other regions of similar geology/tectonic [29-31,38,40,41,55-58].

Detailed and critical analysis of results shows Curie depths (km) between 11 km and 27 km. Plot of the calculated curie depths between 12 km and 26 km at a 2 km contour interval is as shown (Figure 5). The shallowest depth of 11 km is calculated around the area of Abakali-

ki (A) whereas the deepest depth was calculated around Otukpa (K). The lowest Curie depth as calculated is related to the Abakaliki anticlinorium while the deepest result is in connection with the Anambra basin. It is stimulating to notice that lower Curie depths are noted over the basement rocks and areas affected by Tertiary volcanic [59,60]. Elucidation of geology and interpretation of geophysical data in the region has shown the animation of underplat-

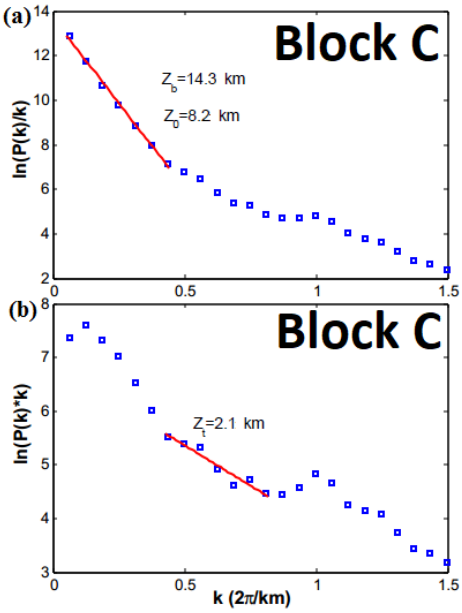


**Figure 4.** Plots of power spectrums for Block (C) for the bottom ($Z_b$) and centroid ($Z_o$) depths (a) and top ($Z_t$) depth (b) calculations. Best fits for computations of the depths on the spectra are shown (i.e., in red lines).

**Table 1.** Results of estimated magnetic bottom (Curie) depths surface heat flow (SHF) values for different blocks in the region.

| Magnetic Block | Curie depth (km) | Surface Heat Flow ($mWm^{-2}$) |
|---|---|---|
| A | 11 | 132 |
| B | 16 | 91 |
| C | 14 | 104 |
| D | 15 | 97 |
| E | 12 | 121 |
| F | 18 | 81 |
| G | 18 | 81 |
| H | 17 | 85 |
| I | 17 | 85 |
| J | 15 | 97 |
| K | 27 | 54 |
| L | 22 | 66 |
| M | 18 | 81 |
| N | 19 | 76 |
| O | 20 | 72 |
| P | 23 | 63 |
| Q | 23 | 63 |
| R | 22 | 66 |
| S | 16 | 91 |
| T | 17 | 85 |
| U | 19 | 76 |
| V | 19 | 76 |
| W | 23 | 63 |
| X | 22 | 66 |
| Y | 18 | 81 |

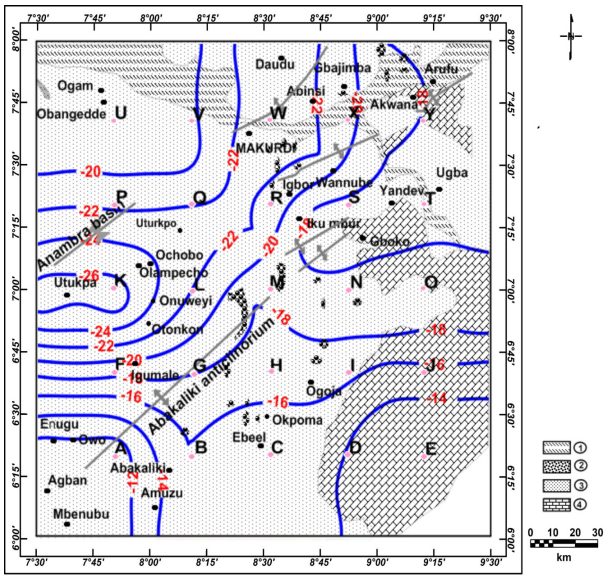


**Figure 5.** Computed Curie depths (km) underneath the area based on the modified centroid method is presented. The calculated depths are in the range between 11 km and 27 km. The map is prepared based on the overlapping blocks. The legends: (1) is the Tertiary-recent sediments (2) is the Tertiary volcanic (3) is the Cretaceous sediments and (4) is the Precambrian basement rocks.

**Table 2.** Calculated values of SHF over some major locations in the region.

| SHF Status | SHF Values ($mWm^{-2}$) | Block numbers | Locations |
|---|---|---|---|
| Lower | 54 | K | Utukpa |
| | 63 | P, Q & W | Uturkpo & Makurdi |
| Intermediate | 81 | F & G | Akwana & Igumale |
| | 76 | U & V | Ogam/Obangedde |
| | 66 | L, R & X | Onuweyi, Igbor & Akwana |
| Higher | 132 | A | Abakaliki |
| | 91 | B & S | Ebeel & Yandev |
| | 104 | C | Okpoma |
| | 85 | H | Ogoja |

ing in the crust underneath the region as the result of past tectonic activity [29-31,40,41].

We presented the lower, intermediate and higher calculated values of SHF in the region of study as shown in Table 2.

The lowest (i.e., in block K) SHF as calculated is along the Anambra basin with the highest (block A) result calculated along the Abakaliki anticlinorium axis (Figure 6). It is observed that the zones of the higher values of SHF are consistent with the areas of magmatic intrusions and basement complexes. The Abakaliki anticlinorium along which the highest result (132 $mWm^{-2}$) is the area strongly affected by intense tectonic and magmatic activities. Published geology and geophysical data show that the intrusion beneath the Abakaliki anticlinorium is beyond its surface exposure [30,31,38,40,41].

Results of the calculated Curie depths (km) [39] were compared with the previously calculated crustal thickness (Moho depths) in the region. The Moho depths results in the region come from regional gravity and seismological studies [30,55,61-63]. Studies of depths to the major density contrast beneath parts of the Benue trough show that Moho depth of about 24 km was reported around Makurdi [61]. The present study found Curie depth of 22-23 km around the Makurdi area. Along the Abakaliki axis, Moho depths of 10-20 km were reported [31,61-63]. The result is comparable with the calculated Curie depth of 11-20 km along this axis. Along the Anambra axis, Moho depths between 28-34 km were reported from gravity data [61-63] and

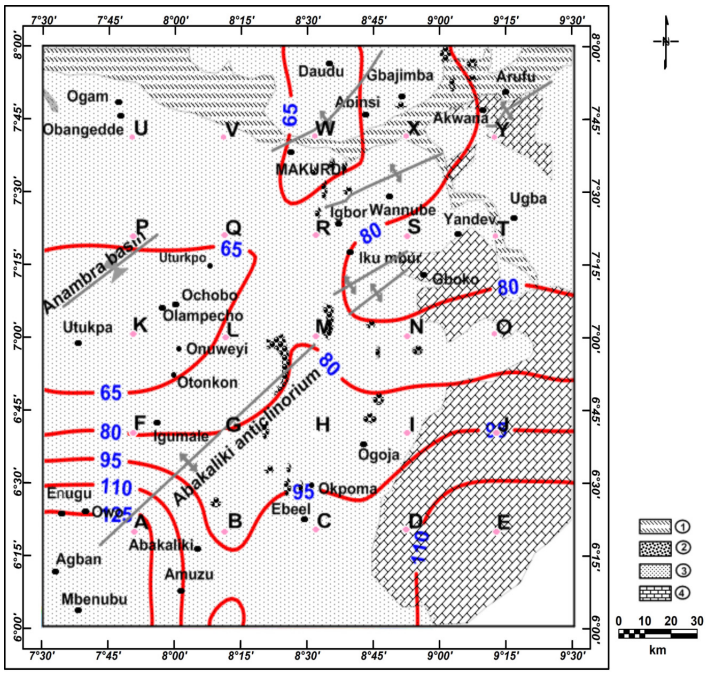


**Figure 6.** Calculated SHF values in the area based on 1-D Fourier's law. The estimated results in the region are between 54 $mWm^{-2}$ and 132 $mWm^{-2}$. The map is also prepared by extrapolation to visualize the entire region of the study. The legends: (1) is the Tertiary-recent sediments (2) is the Tertiary volcanic (3) is the Cretaceous sediments and (4) is the Precambrian basement rocks.

Moho depth of 23 km [55] from the broad band seismological station in the region.

The study found the only bore-hole heat flow measurements between 48-76 $mWm^{-2}$ [64-66], in the region from the Anambra basin. In the present study, SHF as calculated along the Anambra basin was between 54-81 $mWm^{-2}$. The Anambra basin is a rifted subsidiary that formed part of the lower Benue trough. It is of great importance with a high energy-rich in-filled sedimentary thickness of over 9 km [32,38]. In general, it is observed that, with the exception of the Makurdi area where there is surface exposure of Tertiary volcanic, areas where higher SHF values were recorded are consistent with the areas of volcanism and exposed basement rocks. This could indicate that basalts are perhaps deep beneath the sediments around Makurdi. In the region, volcanism intrudes on both the sediments and basement rocks [33]. It is interesting to observe that volcanism in the region is inseparable from the anticlinal folds. In the region, a hot spring (i.e., middle Benue spring) with the highest temperature of around 53.5 °C was recorded [67].

## 5. Conclusions

This study presents estimation of Curie depth and SHF values in the lower and part of middle Benue trough including part of Anambra basin. The recorded Curie depths in the region vary between 11 km and 27 km. The shallower (11-18 km) Curie depth was interpreted in terms of the Tertiary volcanic and the Precambrian metamorphic (basement) rocks. The computed SHF values are between 54 $mWm^{-2}$ and 132 $mWm^{-2}$ within the study area. Higher SHF (85-132 $mWm^{-2}$) accounts for the volcanic and metamorphics in the regions. Lower SHF values interpret zones of thick crustal architecture. The results presented are therefore, an attempt towards quantitatively assessing the viability of the thermal energy potentials, extractable of the energy and an installation of a power plant to ascertain the viability of generating electricity from the reservoir.

## Author Contributions

Mukaila Abdullahi (MA), Yunis B. Valdon (YBV), Fartisincha P. Andrew (FPA), Bello Yusuf Idi (BYI).

MA, FPA was responsible for project conceptualization, administration, data collection, analysis, literature work, funding acquisition and writing of the original draft of the article. MA, YBV, and BYI were responsible for the geological survey of the study area, data generation, review and final editing. All correspondence is to MA.

## Acknowledgement

The author is thankful to the Nigerian Geological Survey Agency (NGSA), Abuja office for providing the aeromagnetic data used in this work. The research was funded by Tertiary Education Trust Fund (TET Fund), Nigeria under the Institutional Based Research (IBR) fund. The authors also acknowledge the Research and Development (R&D) office of Modibbo Adama University Yola, Nigeria through which the research fund was released, and the Departments of Science Laboratory Technology where the research was conducted. The constructive comments and observations of three anonymous reviewers are highly acknowledged.

## Conflict of Interest

The authors declared that they have no conflict of interest.

## References

[1] Bhattacharyya, B.K., Leu, L.K., 1975. Analysis of magnetic anomalies over Yellowstone National Park: Mapping of Curie point isothermal surface for geothermal reconnaissance. Journal of Geophysical Research. 80, 4461-4465.

[2] Tanaka, A., Okubo, Y., Matsubayashi, O., 1999. Curie point depth based on spectrum analysis of the magnetic anomaly data in East and Southeast Asia. Tectonophysics. 306, 461-470.

[3] Chiozzi, P., Matsushima, J., Okubo, Y., et al., 2005. Curie-point depth from spectral analysis of magnetic data in central-southern Europe. Physics of Earth and Planetary Interior. 152(4), 267-276.

[4] Ross, H.E., Blakely, R.J., Zoback, M.D., 2006. Testing the use of aeromagnetic data for the determination of Curie depth in California. Geophysics. 71, L51-L59.

[5] Rajaram, M., Anand, S.P., Hemant, K., et al., 2009. Curie isotherm map of Indian subcontinent from satellite and aeromagnetic data. Earth and Planetary Science Letter. 281(3-4), 147-158.

[6] Trifonova, P., Zhelev, Z., Petrova, T., et al., 2009. Curie point depths of Bulgarian territory inferred from geomagnetic observations and its correlation with regional thermal structure and seismicity. Tectonophysics. 473(3-4), 362-374.

[7] Bansal, A.R., Gabriel, G., Dimri, V.P., et al., 2011. Estimation of the depth to the bottom of magnetic sources by a modified centroid method for fractal

distribution of sources: an application to aeromagnetic data in Germany. Geophysics. 76, L11-22.

[8] Bansal, A.R., Anand, S.P., Rajaram, M., et al., 2013. Depth to the bottom of magnetic sources (DBMS) from aeromagnetic data of central India using modified centroid method for fractal distribution of sources. Tectonophysics. 603, 155-161.

[9] Bansal, A.R., Dimri, V.P., 2013. Modelling of magnetic data for scaling geology. Geophysical Prospecting. 62(2), 385-396.

[10] Bansal, A.R., Dimri, V.P., Kumar, R., et al., 2016. Curie depth estimation from aeromagnetic for fractal distribution of sources. Fractal solutions for understanding complex system in earth sciences. Springer Earth System Sciences. Springer, Cham: Switzerland. pp. 19-31.

[11] Dunlop, D.J., Ozdemir, O., 1997. Rock magnetism: Fundamentals and frontiers. Cambridge University Press: Cambridge.

[12] Bhattacharyya, B.K., Leu, L.K., 1977. Spectral analysis of gravity and magnetic anomalies due to rectangular prismatic bodies. Geophysics. 42, 41-50.

[13] Shuey, R.T., Schellinger, D.K., Tripp, A.C., et al., 1977. Curie depth determination from aeromagnetic spectra. Geophysical Journal of Royal Astronomical Society. 50, 75-101.

[14] Okubo, Y., Graf, R.J., Hansen, R.O., et al., 1985. Curie point depths of the island of Kyushu and surrounding area, Japan. Geophysics. 50, 481-489.

[15] Blakely, R.J., 1996. Potential theory in gravity and magnetic applications. Cambridge University Press: Cambridge.

[16] Maus, S., Gordon, D., Fairhead, J.D., 1997. Curie temperature depth estimation using a self-similar magnetization model. Geophysical Journal International. 129, 163-168.

[17] Ravat, D., Pignatelli, A., Nicolosi, I., et al., 2007. A study of spectral methods of estimating the depth to the bottom of magnetic sources from near-surface magnetic anomaly data. Geophysical Journal International. 169, 421-434.

[18] Bouligand, C., Glen, J.M.G., Blakely, R.J., 2009. Mapping Curie temperature depth in the western United States with a fractal model for crustal magnetization. Journal of Geophysical Research. 114, B11104.

[19] Ravat, D., Morgan, P., Lowry, A.R., 2016. Geotherms from the temperature-depth-constrained solutions of 1-D steady-state heat-flow equation. Geosphere. 12(4), 1187-1197.

[20] Nwankwo, L.I., 2015. Estimation of depths to the bottom of magnetic sources and ensuing geothermal parameters from aeromagnetic data of Upper Sokoto Basin Nigeria. Geothermics. 54, 76-81.

[21] Melouah, O., Eldosouky, A.M., Ebong, E.D., 2021. Crustal architecture, heat transfer modes and geothermal energy potentials of the Algerian Triassic provinces. Geothermics. 96, 102211.

[22] Onwuemesi, A.G., 1997. One-dimensional spectral analysis of aeromagnetic anomalies and curie depth isotherm in the Anambra basin of Nigeria. Journal of Geodynamics. 23(2), 95-107.

[23] Nwankwo, C.N., Ekine, A.S., Nwosu, L.I., 2009. Estimation of the heat flow variation in the Chad basin, Nigeria. Journal of Applied Sciences and Environmental Management. 13, 73-80.

[24] Obande, G.E., Lawal, K.M., Ahmed, L.A., 2014. Spectral analysis of aeromagnetic data for geothermal investigation of Wikki Warm spring, north-east Nigeria. Geothermics. 50, 85-90.

[25] Abraham, E.M., Obande, E.G., Chukwu, M., et al., 2015. Estimating depth to the bottom of magnetic sources at Wikki warm spring region, northeastern Nigeria, using fractal distribution of sources approach. Turkish Journal of Earth Sciences. 24(5), 494-512.

[26] Chukwu, C.G., Udensi, E.E., Abraham, E.M., et al., 2017. Geothermal energy potential from analysis of aeromagnetic data of part of the Niger-delta basin, southern Nigeria. Energy. 143, 846-853.

[27] Lawal, T.O., Nwankwo, L.I., Iwa, A.A., et al., 2018. Geothermal energy potential of the Chad basin, north-eastern Nigeria. Journal Applied Science and Environmental Management. 22(11), 1817-1824.

[28] Carter, J.D., Barber, W., Tait, E.A., et al., 1963. The geology of parts of Adamawa, Bauchi and Bornu Provinces in northeastern Nigeria. Bulletin of Geological Society of Nigeria. 30, 109.

[29] Cratchley, C.R., Jones, G.P., 1965. An interpretation of the geology and gravity anomalies of the Benue Valley Nigeria. Oversea Geological Survey, Geophysics Paper. (1), 1-25.

[30] Ajayi, C.O., Ajakaiye, D.E., 1981. The origin and perculiarities of the Nigerian Benue Trough: Another look from recent gravity data obtained from middle Benue. Tectonophysics. 80, 285-303.

[31] Adighije, C., 1981. A gravity interpretation of the Benue Trough, Nigeria. Tectonophysics. 79, 109-128.

[32] Agagu, O.K., Adighije, C.I., 1983. Tectonic and sedimentation framework of the lower Benue Trough, southeastern Nigeria. Journal of African Earth Sciences. 1(3/4), 267-274.

[33] Ofoegbu, C.O., 1984. Interpretation of aeromagnetic anomalies over Lower and Middle Benue Trough of Nigeria. Geophysical Journal of Royal Astronomical Society. 79, 813-823.

[34] Benkhelil, J., 1989. The origin and evolution of the Cretaceous Benue Trough (Nigeria). Journal of African Earth Sciences. 6, 251-282.

[35] Ogunmola, J.K., Ayolabi, E.A., Olobaniyi, S.B., 2016. Structural-depth analysis of the Yola Arm of the Upper Benue Trough of Nigeria using high resolution aeromagnetic data. Journal of African Earth Sciences. 124, 32-43.

[36] Abdullahi, M., Kumar, R., Singh, U.K., 2019. Magnetic basement depth from high-resolution aeromagnetic data of parts of lower and middle Benue Trough (Nigeria) using scaling spectral method. Journal of African Earth Sciences. 150, 337-345.

[37] Obaje, N.G., 2009. Geology and mineral resources of Nigeria. Springer: Berlin. pp. 221.

[38] Abdullahi, M., Singh, U.K., 2018. Basement geology derived from gravity anomalies beneath the Benue Trough of Nigeria. Arabian Journal of Geosciences. 11, 694.

[39] Abdullahi, M., Kumar, R., 2020. Curie depth estimated from high-resolution aeromagnetic data of parts of lower and middle Benue trough (Nigeria). Acta Geodaetica et Geophysica. 55(4), 627-643.

[40] Anudu, G.K., Stephenson, R.A., Macdonald, D.I.M., 2014. Using high-resolution aeromagnetic data to recognize and map intra-sedimentary volcanic rocks and geological structures across the Cretaceous middle Benue Trough, Nigeria. Journal of African Earth Sciences. 99, 625-636.

[41] Maluski, H., Coulon, C., Popoff, M., et al., 1995. $40^{Ar}/39^{Ar}$ chronology, petrology and geodynamic setting of Mesozoic to early Cenozoic magmatism from the Benue Trough, Nigeria. Journal of Geological Society, London. 152, 311-326.

[42] Ajayi, C.O., Ajakaiye, D.E., 1986. Structures deduced from gravity data in the middle Benue Trough, Nigeria. Journal of African Earth Sciences. 5(4), 359-369.

[43] Ofoegbu, C.O., 1985. A review of the geology of the Benue Trough, Nigeria. Journal of African Earth Sciences. 3(3), 283-291.

[44] Maus, S., Dimri, V.P., 1996. Depth estimation from the scaling power spectrum of potential fields. Geophysical Journal International. 124, 113-120.

[45] Pilkington, M., Todoeschuck, J.P., 1993. Fractal magnetization of continental crust. Geophysical Research Letter. 20, 627-630.

[46] Pilkington, M., Gregotski, M.E., Todoeschuck, J.P., 1994. Using fractal crustal magnetization models in magnetic interpretation. Geophysical Prospecting. 42, 677-692.

[47] Bansal, A.R., Gabriel, G., Dimri, V.P., 2010. Power law distribution of susceptibility and density and its relation to seismic properties: An example from the German Continental Deep Drilling Program. Journal of Applied Geophysics. 72, 123-128.

[48] Pilkington, M., Todoeschuck, J.P., 1995. Scaling nature of crustal susceptibilities. Geophysical Research Letter. 22, 779-782.

[49] Maus, S., Dimri, V.P., 1994. Scaling properties of potential fields due to scaling sources. Geophysical Research Letter. 21, 891-894.

[50] Maus, S., Dimri, V.P., 1995. Potential field power spectrum inversion for scaling geology. Journal of Geophysical Research. 100, 12605-12616.

[51] Fedi, M., Quarta, T., Santis, A.D., 1997. Inherent power-law behavior of magnetic field power spectra from a Spector and Grant ensemble. Geophysics. 62, 1143-1150.

[52] Kumar, R., Bansal, A.R., Anand, S.P., et al., 2018. Mapping of magnetic basement in Central India from aeromagnetic data for scaling geology. Geophysical Prospecting. 66, 226-239.

[53] Li, C.F., Lu, Y., Wang, J., 2017. A global reference model of Curie-point depths based on EMAG2. Scientific Report. 7(1), 45129.

[54] Turcotte, D.L., Schubert, G., 1982. Geodynamics applications of continuum physics to geologic problems. Wiley: New York.

[55] Akpan, O., Nyblade, A., Okereke, C., et al., 2016. Crustal structure of Nigeria and Southern Ghana, West Africa from P-wave receiver functions. Tectonophysics. 676, 250-260.

[56] Pham, L.T., Eldosouky, A.M., Melouah, O., et al., 2021. Mapping subsurface structural lineaments using the edge filters of gravity data. Journal of King Saud University—Science. 33(8), 101594.

[57] Melouah, O., Pham, L.T., 2021. An improved ILTHG method for edge enhancement of geological structures: Application to gravity data from the Oued Righ valley. Journal of African Earth Sciences. 177, 104162.

[58] Melouah, O., Steinmetz, R.L.L., Ebong, E.D., 2021. Deep crustal architecture of the eastern limit of the West African Craton: Ougarta range and western Algerian Sahara. Journal of African Earth Sciences. 183, 104321.

[59] Tokam, K.A.P., Tabod, C.T., Nyblade, A.A., et al.,

2010. Structure of the crust beneath Cameroon, West Africa, from the joint inversion of Rayleigh wave group velocities and receiver functions. Geophysical Journal International. 183, 1061-1076.

[60] Tugume, S., Nyblade, A., Julià, J., et al., 2013. Precambrian crustal structure in Africa and Arabia: Evidence lacking for secular variation. Tectonophysics. 609, 250-266.

[61] Fairhead, J.D., Okereke, C.S., 1987. A regional gravity study of the West African rift system in Nigeria and Cameroon and its tectonic implication. Tectonophysics. 143, 141-159.

[62] Okereke, C.S., 1988. Contrasting modes of rifting: The Benue Trough and Cameroon volcanic line, West Africa. Tectonics. 7(4), 775-784.

[63] Fairhead, J.D., Okereke, C.S., Nnange, J.M., 1991. Crustal structure of the Mamfe basin, West Africa based on gravity data. Tectonophysics. 186, 351-358.

[64] Nwachukwu, S.O., 1976. Approximate geothermal gradients in the Niger Delta sedimentary basins. The American Association of Petroleum Geology. 60(7), 1073-1077.

[65] Avbovbo, A.A., 1978. Geothermal gradients in the southern Nigerian basins. Bulletin of Canadian Petroleum Geology. 26(2), 268-274.

[66] Onuaha, K.M., Ekine, A.S., 1999. Subsurface temperature variations and heat flow in the Anambra Basin, Nigeria. Journal of African Earth Sciences. 28(3), 641-652.

[67] Kwaya, M.Y., Kurowska, E., 2018. Geothermal exploration in Nigeria—Country update. Proceedings of 7th African Rift Geothermal Conference; 2018 Oct 31; Kigali, Rwanda. Nairobi: ARGeo—The African Rift Geothermal Development Facility.

**Earth and Planetary Science**
https://ojs.nassg.org/index.php/eps

**EDITORIAL**

# Uncovering the Secrets of the Gas Giant

**Alessandro Mura**

INAF—Istituto di Astrofisica e Planetologia Spaziali, Rome, 00133, Italy

ARTICLE INFO

*Article history*
Received: 19 April 2023
Accepted: 20 April 2023
Published Online: 23 April 2023

If we want to keep our Earth habitable, we must strive to know as much as possible about all its less fortunate "brother" planets. Like novice students of "planetary physiology", we must study the sick to learn how to stay healthy. It is necessary to understand how planets have evolved, whether some of them have been potentially habitable in the past, how the four smallest rocky ones have been guided in their evolution by the four gas or icy giants. Among these last ones, Jupiter is the protagonist. All theories about the birth and evolution of the Solar System revolve around its "personal history", because it is probably the first to form and therefore the one that has influenced others more than any other planet.

Although much can be understood about a planet just by remote observation, direct exploration offers us otherwise unattainable information. We can study its gravity and internal structure, its magnetic field, its environment; we have the possibility of observing regions not visible from Earth, such as the poles. At the end of the 1970s, after the fly-by of the Pioneer 10 probe, NASA began designing a mission entirely dedicated to Jupiter: Galileo. After Galileo, whose scientific results were partly compromised by some technical problems, it was Juno's turn, launched in 2011 and in orbit around Jupiter since 2016.

Named after the consort of the Roman god, the Juno probe observes the planet Jupiter completely, scrutinizing him even beneath its thick layer of clouds. Equipped with a suite of instruments, including plasma and field detectors, cameras, a magnetometer, a microwave radiometer and a gravity science experiment, Juno has been able to peer beneath the planet's thick clouds and provide a detailed view of its atmosphere, it's interior and the environment around the planet [1]. Juno has shed new light on the planet's interior, revealing that Jupiter's core is larger and more diffuse ("fuzzy") than previously thought. This finding has important implications for our understanding

*Corresponding Author:
Alessandro Mura,
INAF—Istituto di Astrofisica e Planetologia Spaziali, Rome, 00133, Italy;
*Email: alessandro.mura@inaf.it*

DOI: http://dx.doi.org/10.36956/eps.v2i1.845

of how gas giants like Jupiter form and evolve over time.

One of the first discoveries made by Juno is the existence of two huge, stable cyclone systems at both planets' poles. The two polar cyclones, which are thousands of kilometres wide, are surrounded by an octagon of cyclones in the North, and by a pentagon in the South. While scientists are still trying to understand why this unusual configuration exists, it has been recently found that the cyclones are quite stable, with a lifetime of tens to hundreds of years [2].

Outside the polar regions, the fast east-west jet streams, separating the iconic belts and zones, have been found to be quite deep. The measurements of gravitational harmonics indicate that these streams have a vertical extension of thousands of kilometres (~3000) beneath the reference level of 1 bar [3]. That depth, magnetic dissipation could occur, and this is an example of the existing link between the magnetic field and the atmospheric winds. Another one has been found in the vicinity of the Great Blue Spot, which is an anomalous intensification of magnetic flux close to the equator. Since Juno is constantly monitoring the configuration of the magnetic field of Jupiter, it is possible to analyse its temporal variability, which suggests a significant advection of the magnetic field by deep zonal winds close to this Great Blue Spot. This is, again, consistent with the penetration of zonal winds to a depth of ~3,500 km [4].

Finally, recent measurements of Jupiter's gravity field showed that its gaseous envelope is inhomogeneous, with its interior enriched in heavy elements, surrounding a fuzzy core. Since such enrichment should have continued during the gas accretion phase of Jupiter formation, this poses constraints on models and theories for the formation of giant planets (and hence the whole Solar System) [5].

Juno is now waiting for two other missions that will contribute to our understanding of Jupiter. The first one is the European Space Agency's (ESA) Jupiter Icy Moons Explorer (JUICE), launched in April 2023. This ambitious mission will study Jupiter's icy moons, including Europa, Ganymede, and Callisto, which are believed to harbour subsurface oceans that may be capable of supporting life. JUICE will use a suite of instruments to study the composition, geology, and potential habitability of these moons, as well as the interactions between the moons and the planet's magnetic field.

The other is the upcoming Europa Clipper mission, which is set to launch in the mid 2020s. This is a NASA mission that will study Jupiter's moon Europa, which is believed to be one of the most promising places in the solar system to search for signs of life. The Europa Clipper mission will conduct a detailed survey of Europa's surface and environment, using a suite of instruments to search for signs of life and study the moon's geology and composition.

In conclusion, the recent developments in Jupiter exploration have given us a fascinating glimpse into the complex world of this gas giant. From the Juno mission's detailed study of Jupiter's atmosphere and magnetic field to the upcoming JUICE and Europa Clipper missions, we are learning more and more about the processes that shape this enigmatic world. With each new mission and discovery, we are unlocking the secrets of Jupiter and expanding our understanding of the solar system and our place within it.

## Conflicts of Interest

The author declares no conflicts of interest.

## References

[1] Bolton, S.J., Adriani, A., Adumitroaie, V., et al., 2017. Jupiter's interior and deep atmosphere: The initial pole-to-pole passes with the Juno spacecraft. Science. 356(6340), 821-825.
DOI: https://doi.org/10.1126/science.aal2108

[2] Adriani, A., Mura, A., Orton, G., et al., 2018. Clusters of cyclones encircling Jupiter's poles. Nature. 555, 216-219.
DOI: https://doi.org/10.1038/nature25491

[3] Kaspi, Y., Galanti, E., Hubbard, W.B., et al., 2018. Jupiter's atmospheric jet streams extend thousands of kilometres deep. Nature. 555(7695), 223-226.
DOI: https://doi.org/10.1038/nature25793

[4] Connerney, J.E.P., Timmins, S., Oliversen, R.J., et al., 2022. A new model of Jupiter's magnetic field at the completion of Juno's Prime Mission. Journal of Geophysical Research: Planets. 127, e2021JE007055.
DOI: https://doi.org/10.1029/2021JE007055

[5] Miguel, Y., Bazot, M., Guillot, T., et al., 2022. Jupiter's inhomogeneous envelope. Astronomy & Astrophysics. 662, A18.
DOI: https://doi.org/10.1051/0004-6361/202243207

Earth and Planetary Science
https://ojs.nassg.org/index.php/eps

RESEARCH ARTICLE

# Hydrogeological-geotechnical Characterization and Analysis for Construction of a Subsurface Reservoir at a Coastal Site in the Nakdong Deltaic Plain, Busan, South Korea

**Pham Huy Giao**[1*] **Namsik Park**[2*]

1. Department of Geological Engineering, PetroVietnam University (PVU), Baria-Vung Tau, 790000, Vietnam
2. Department of Civil Engineering, Dong-A University, Busan, 49315, Korea

ARTICLE INFO

*Article history*
Received: 12 February 2023
Revised: 10 April 2023
Accepted: 20 April 2023
Published Online: 27 April 2023

*Keywords*:
Artificial recharge
Subsurface reservoir
Managed Aquifer Recharge (MAR)
Finite element (FE) consolidation analysis
Land subsidence control
Nakdong plain

ABSTRACT

Store and recover clean groundwater from a man-made subsurface reservoir is useful for the development of coastal cities. A full-scale pilot field test of managed aquifer recharge (MAR) schemes were conducted in the Nakdong River plain, Korea. The process involved constructing a hydrogeological-geotechnical model based on investigation data, including the target aquifer that was located between 30 and 67 meters deep. The subsurface response to water pumping was analyzed, and this led to the creation of charts to determine the maximum allowable injection pressure and maximum recharge rate. For two factors of safety of 1.5 and 2.0, the maximum injection head rise was estimated to be 9.7 meters and 7.25 meters, respectively, corresponding to recharge rates of 5,000 and 3,800 $m^3$/d. One-dimensional FE consolidation analyses were conducted for different groundwater drawdowns (2, 5, 10 and 15 m) and the results showed a good match with the monitored settlement and rebound for the 2-meter drawdown case. The study concluded that the injection rate could potentially be much higher than what was tested, which would increase the capacity of the subsurface reservoir. The lessons learned from this study are useful for similar coastal sites in terms of the application of MAR technology.

## 1. Introduction

Artificial recharge is a process where water is injected into the ground [1], while Aquifer Storage Recovery (ASR) is a more comprehensive concept of water management that involves the storage of water in an aquifer through wells and the recovery of water when it is needed. Managed aquifer recharge (MAR) is a term conceived by the British hydrogeologist Ian Gale for an increasingly impor-

*Corresponding Author:
Pham Huy Giao,
Department of Geological Engineering, PetroVietnam University (PVU), Baria-Vung Tau, 790000, Vietnam;
*Email: giaoph@pvu.edu.vn*
Namsik Park,
Department of Civil Engineering, Dong-A University, Busan, 49315, Korea;
*Email: nspark@dau.ac.kr*

DOI: http://dx.doi.org/10.36956/eps.v2i1.810

tant water management strategy, alongside demand management, to help maintain, enhance and secure stressed groundwater systems and improve water quality. The term Managed Aquifer Recharge (MAR) is commonly used nowadays to reflect the continuing advancement in recharge technology [2,3]. As reported by Dilon et al. [4], by the end of the last decade "*MAR has reached about 10 km$^3$/year or 2.4% of groundwater extraction in countries reporting MAR (or approximately 1.0% of global groundwater extraction)*". Typical examples of stressed groundwater systems are found in most Middle East and North Africa (MENA) countries where groundwater extraction exceeds its renewability by 6% to 100% [5], where the potential application of MAR is seriously investigated.

The success of many MAR projects depends on the ability to construct a suitable subsurface reservoir. This can be achieved by injecting fresh surface water into an underground confined aquifer, which can be commonly found at the estuary of a large river, such as in the Nakdong deltaic plain in Busan, Korea. The main operating facilities of the MAR system include injection wells and pumping wells, which can be dual or separate. During normal operation, water is injected through the injection wells and pumped from the pumping wells simultaneously. The flow of water through the aquifer is expected to enhance the water quality. In emergency situations, such as drought, flood, or accidents, an injection can be stopped to protect the subsurface reservoir, but pumping can still be maintained for a prolonged period. A subsurface reservoir that uses a confined aquifer can be a viable alternative to more conventional water supply schemes.

It is important to understand the geotechnical and hydrogeological characteristics of the subsurface to ensure the success of a subsurface reservoir. This includes knowledge of the deformation of the soil layer, particularly the lower-permeability layer overlying a confined aquifer. This understanding can help to prevent subsidence caused by groundwater pumping, which is a common problem in many Asian cities where water demand is high due to rapid population growth, urban expansion, and industrial development [6-10]. It is crucial to have a comprehensive understanding of the subsurface behavior in response to pumping and storage activities to design and operate a subsurface reservoir effectively.

A field experiment on the subsurface reservoir was set up and conducted at a coastal site in the Nakdong River plain from June 2013 to the end of 2018. A substantial amount of field data was collected. The primary objective of this study is to propose an integrated geotechnical-hydrogeological model, which can be used to conduct groundwater and consolidation analyses and simulate and predict the responses of the artificially-injected and stored reservoir to the discharge-recharge operation. Another objective of this study is to construct charts to aid in determining the maximum injection pressure and recharge rate.

## 2. Testing and Monitoring

### 2.1 Study Location

The construction site of a subsurface reservoir in the Nakdong plain is shown in Figure 1. It is located on the left floodplain of the Nakdong River, and its shape is approximately square, with a side length of 400 meters.

### 2.2 Monitoring

The plan view of the field instrumentation is depicted in Figure 2. It includes 12 red-colored injection wells labeled OIW1-9 and NIW1-3, 8 blue-colored pumping wells labeled W1-8, 10 purple triangle-shaped vibrating wire piezometers designated PW1-10 to monitor pore water pressure, 14 blue rhomb-shaped extensometers labeled SE1-14 to monitor settlements, and 5 black rectangular-shaped surface settlement plates labeled SP1-5. The study site has been divided into five monitoring areas, each equipped with specific extensometers and piezometers. The mon-

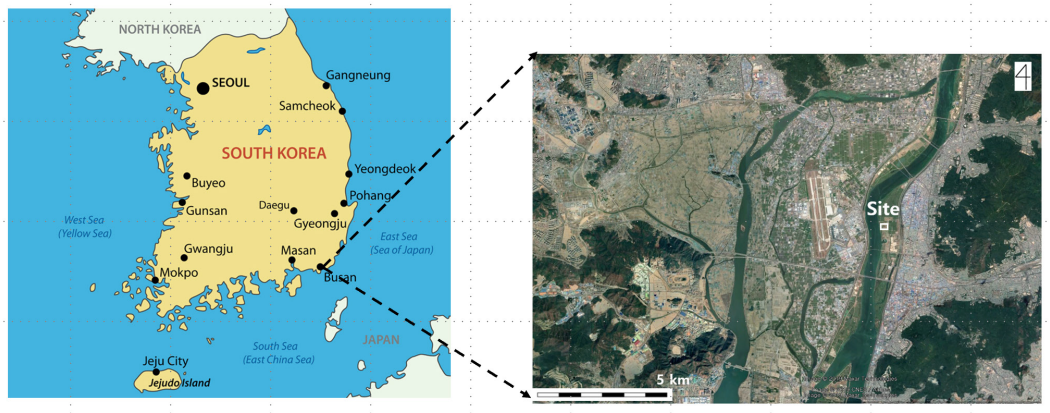


**Figure 1.** The location of the MAR testing site in the Nakdong River plain, Busan, South Korea [11].

itoring areas are designated as Area A (SE1-4, PW1-2, PW9-10), Area B (SE5-8, PW3-4), Area C (SE9-12, PW5-6), and Area D (SE13-14, PW7-8). The type and location of geotechnical sensors are detailed in Table 1.

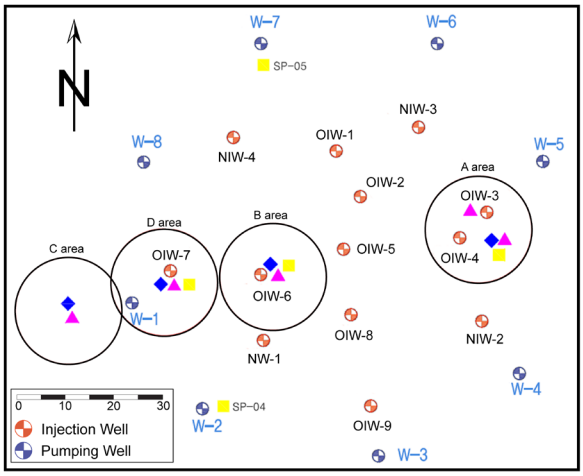


**Figure 2.** Layout of field monitoring instrumentations (modified after DAU, 2017 [11]).

The subsoil profile and the vertical instrumentation layout of each monitoring area are shown in Figure 3.

Additionally, observation wells were installed to monitor groundwater flow. Three wells were placed in the upper sand layer and thirteen wells in the target aquifer. These wells were situated within a 125-meter circular area. However, they were not included in Figure 2 to prevent symbol overcrowding, as the focus of this manuscript is geotechnical.

**Table 1.** Geotechnical sensors and locations.

| Equipment | Symbol (notation) | Location and sensors |
|---|---|---|
| Piezometer-vibrating wire type (PW) | Triangle | A area: PW-1, -2, -9, -10<br>B area: PW-3, -4<br>C area: PW-5, -6<br>D area: PW-7, -8 |
| Settlement Extensometer (SE) | Diamond | A area: SE-1, -2, -3, -4<br>B area: SE-5, -6, -7, -8<br>C area: SE-9, -10, -11, -12<br>D area: SE-13, -14 |
| Settlement Plate (SP) | Square | A area: SP-1<br>B area: SP-2<br>D area: SP-3<br>Other: SP-4, -5 |

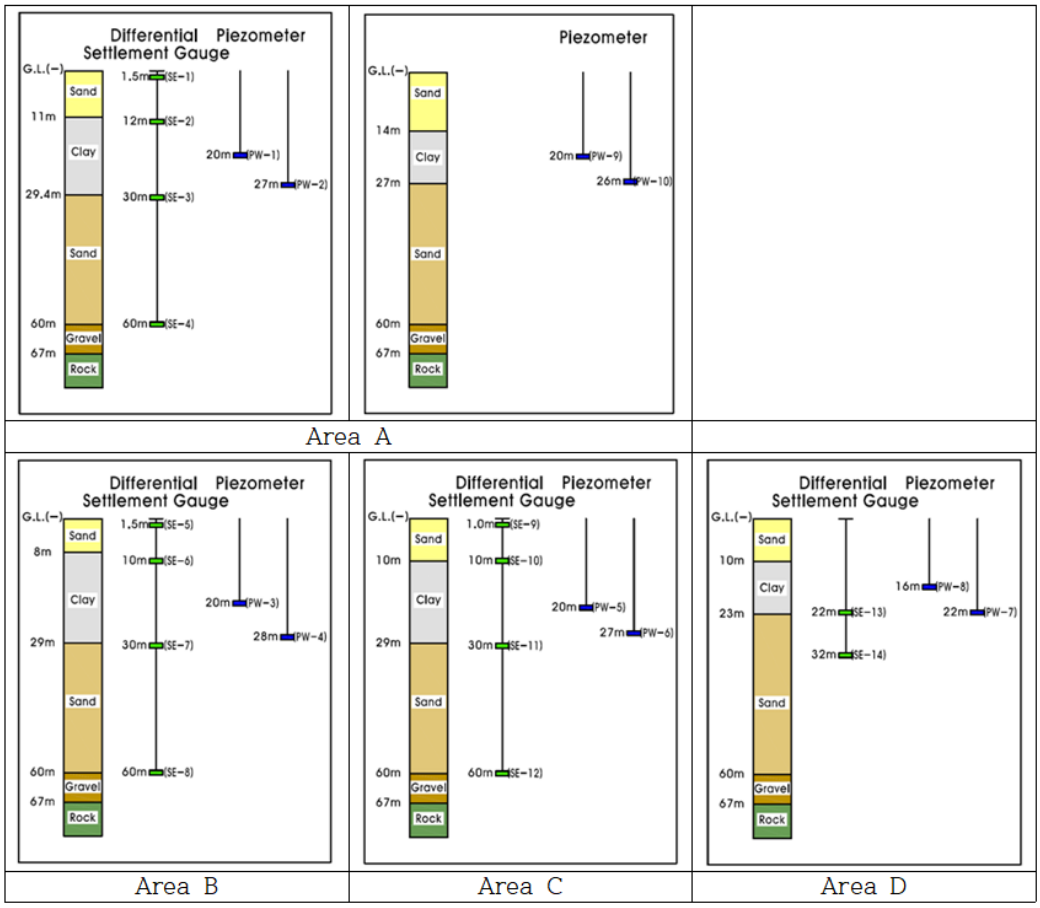


**Figure 3.** Subsoil profile and field instrumentations layouts at five monitoring areas [11].

## 3. The Hydro-geotechnical Model for the MAR Testing Site

### 3.1 Subsurface Model

Three investigative boreholes were drilled at locations OW2, OW5, and OW6, reaching a depth of 60 meters. Soil samples were collected from these boreholes for laboratory testing, as indicated in Table 2a. A standard penetration test (SPT) was also performed in the same three boreholes at 1-meter intervals, excluding the sampling positions.

The soil layers' geotechnical index properties were tested, as shown in Table 2a. The results of the normal and constant rate of strain (CRS) consolidation tests are presented in Table 2b. A hydro-geotechnical model was created for the subsurface at the MAR testing site, as depicted in Figure 4. This model shows a compressible clay layer from 10 to 30 meters deep, which is composed of a normally-consolidated (NC) clay with an over-consolidation ratio (OCR) ranging from 1.0 to 1.1. This clay layer is known as Busan marine soft clay that was well investigated by Chung et al. [12] and it functions as a confining aquitard, sandwiched between the top unconfined aquifer located from 1 to 10 meters deep and the underlying confined aquifer of gravelly sand located from 30 to 67 meters deep, where the subsurface reservoir is intended to be constructed.

The hydrogeological condition of the confined aquifer is a crucial factor in determining the results of the MAR experiment. In this experiment, parameters that represent the area are more valuable than those at specific points. Aquifer-wide hydraulic conductivity and specific storage were assessed based on three sets of injection-recovery tests. For each test, a different combination of wells was chosen, involving a total of three injection wells and eight monitoring wells.

The durations and injection rates of the tests ranged from five to fourteen days and from approximately 200 $m^3$/d to 260 $m^3$/d, respectively. The distances between the injection and observation wells were from 8.0 m to 71.4 m. In each test, water was injected through one or two wells, and hydraulic heads were measured at three or four wells. The hydraulic conductivity and specific storage were determined using a numerical groundwater flow model and a genetic algorithm. The aquifer-wide hydrau-

**Table 2a.** Basic geotechnical parameters of the clay layer overlying the target aquifer at the study site.

| Borehole | Sample depth (m) | NSPT | #200 sieve (%) | Gs | W (%) | LL (%) | PL (%) | PI | Soil type |
|---|---|---|---|---|---|---|---|---|---|
| OW2 | 15 | 11-2 | 90.05 | 2.67 | 52 | 42.85 | 29.35 | 13.50 | ML |
| | 16 | | 68.40 | 2.60 | 52 | 39.99 | 29.00 | 11.00 | ML |
| | 18 | | 88.52 | 2.68 | 45 | 55.86 | 37.85 | 18.01 | MH |
| OW5 | 15 | 0-7 | 94.64 | 2.63 | 60 | 47.97 | 26.99 | 20.98 | CL |
| | 17 | | 87.63 | 2.61 | 55 | 45.11 | 28.47 | 16.64 | ML |
| | 18 | | 97.71 | 2.63 | 53 | 49.95 | 32.74 | 18.39 | ML |
| OW6 | 20 | 11-12 | 82.56 | 2.63 | 53 | 47.31 | 32.63 | 14.68 | ML |
| | 21 | | 85.58 | 2.66 | 42 | 36.21 | 26.59 | 9.62 | ML |

**Table 2b.** Results of consolidation tests.

| Consolidation test | Borehole | Sample Depth (m) | $C_r$ | $C_c$ | $P_c$ (kPa) | $\sigma_0$ (kPa) | OCR |
|---|---|---|---|---|---|---|---|
| Standard | OW2 | 18 | 0.068 | 0.59 | 157.6 | 145.2 | 1.09 |
| | OW5 | 19 | 0.078 | 0.78 | 142.8 | 139.2 | 1.03 |
| | OW6 | 22 | 0.058 | 0.42 | 161.5 | 164.8 | 0.98 |
| CRS | OW2 | 18 | 0.052 | 0.56 | 160.0 | 145.2 | 1.10 |
| | OW5 | 19 | 0.068 | 0.76 | 158.0 | 139.2 | 1.14 |
| | OW6 | 22 | 0.060 | 0.51 | 165.0 | 181.7 | 0.91 |

lic conductivity and specific storage were determined to be 17.8 m/d and 4.25 × $10^{-4}$ $m^{-1}$, respectively. The details of the injection tests are outside the scope of this manuscript and will be reported elsewhere.

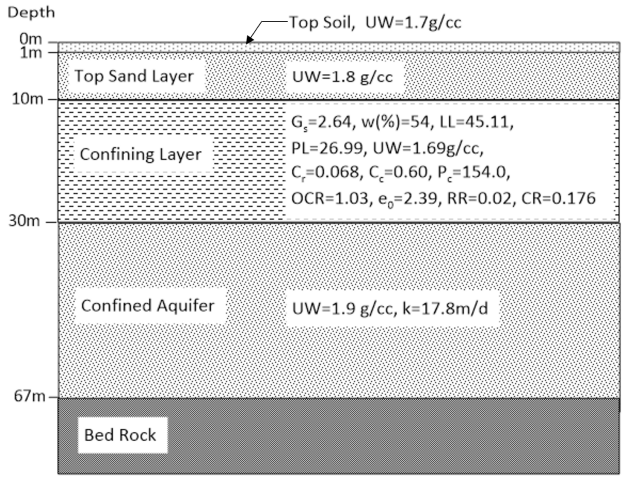


**Figure 4.** The hydro-geotechnical model of the MAR testing site.

### 3.2 Calculation of Maximum Injection Pressure ($P_{max}$) and Maximum Recharge Rate ($Q_{max}$)

The permissible injection pressure is an important design parameter for an artificial recharge well as it determines the safe injection rate and helps prevent boiling. If the injection pressure is higher than a permissible criterion vertical cracks can be developed at the injection depth level and propagated up to the ground surface, damaging the recharge site. Such a phenomenon is commonly referred to as boiling. The permissible injection pressure is basically controlled by the horizontal effective stress at the depth level immediately above the screen or gravel pack.

The procedure to estimate the permissible injection pressure involves calculating the vertical effective stress, determining the coefficient of lateral pressure at rest ($K_0$ = 0.4), calculating the horizontal effective stress ($\sigma'_H = K_0.\sigma'_V$), determining the maximum injection pressure ($P_{max}$) and corresponding head rise ($dh_{max}$), and finally determining the maximum recharge rate ($Q_{max}$) with a factor of safety considered. The charts in Figure 5 and Figure 6 provide a visual representation of these calculations and help in determining the maximum recharge rate ($Q_{max}$).

For this MAR study site, the depth to the top of the gravel pack is 45 m, where the vertical and horizontal effective stresses are 36.2 t/$m^2$ and 14.5 t/$m^2$, considering the coefficient of later pressure at rest equal to 0.4 (see Figure 5). For FS = 1.5, $dh_{max,p} = dh_{max,cal}/FS$ = 14.5 m/1.5 = 9.7 m. Based on the chart in Figure 6, for $dh_{max}$ = 9.7 m, the corresponding maximum injection rate is 5000 $m^3$/d. For FS = 2.0, $dh_{max,p} = dh_{max,cal}/FS$ = 14.5 m/2.0 = 7.25 m. Based on the chart in Figure 6, for $dh_{max}$ = 7.25 m, the corresponding maximum injection rate is 3800 $m^3$/d. It is important to note that these values are just estimates and actual values may vary based on the site-specific conditions and the design of the artificial recharge well. The detailed calculations are shown below:

$$FS = dh_{max,cal}/dh_{max,p} \quad (1)$$

Thus, if FS =1.5 => $dh_{max,p}$ = 14.5/1.5 = 9.7 m => Q = 5,000 $m^3$/d.

Thus, if FS =2.0 => $dh_{max,p}$ = 14.5/2.0 = 7.25 m => Q = 3,800 $m^3$/d.

where: FS is the factor of safety, $dh_{max,p}$ is the maximum head rise to be used in practice, $dh_{max,cal}$ is the maximum head rise calculated using the chart in Figure 5, Q is the recharge rate.

It's important to consider the actual conditions and limitations of the injection facilities when deciding on the injection rate for an artificial recharge experiment. The actual injection rate of 1500 $m^3$/d applied in this experiment was smaller than the geotechnically permissible injection rate due to the limitations of the injection facilities such as injection wells, pumps, and pipes as shown by the calculation results presented earlier. The injection wells were designed with 100 mm PVC pipes and lengths of screens varying between 10 m and 15 m starting from 15 m to 20 m below the bottom of the clay layer.

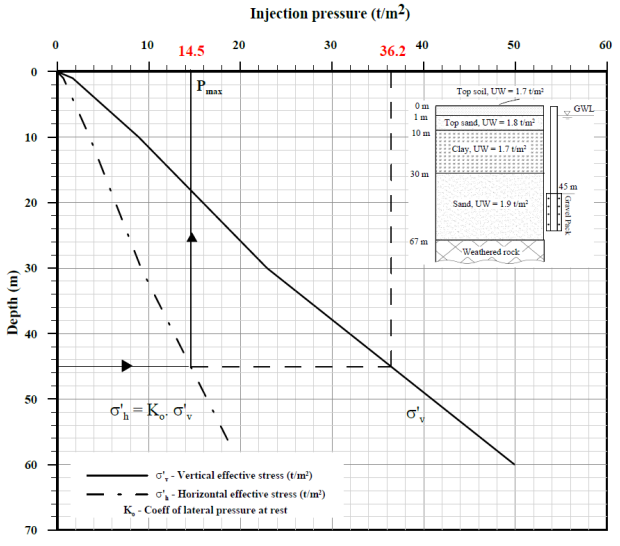


**Figure 5.** Chart to determine the maximum injection pressure ($P_{max}$) for the MAR testing site.

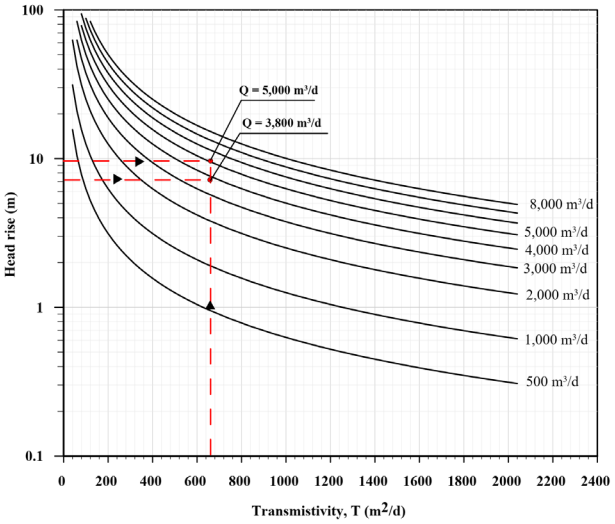


**Figure 6.** Chart to determine the maximum injection rate for the study MAR testing site.

## 4. Consolidation Analysis

### 4.1 FEM Formulation of 1D Consolidation Equation

The consolidation analysis could be done using the 1D FEM code of consolidation analysis named the TZP program to calculate the groundwater drawdown-induced settlement and/or injection-induced rebound of the subsoil [6,8,10]. The 1-D consolidation analysis starts from the following consolidation equation:

$$C_v \frac{\partial^2 u}{\partial z^2} = \frac{\partial u}{\partial t} \tag{2}$$

where $C_v$ is the coefficient of consolidation, u is the rate of dissipation of pore pressure in the clay layer, and u = $dh/\gamma_w$, with dh being the head change and $\gamma_w$ being the unit weight of water. In one-dimensional finite element (1D FEM) consolidation analysis, linear elements are employed instead of quadrilateral elements. Applying Galerkin's procedure on Equation (2) one can get the following weak form:

$$\int_{\Omega^e} C_v \frac{\partial N_k}{\partial z}\frac{\partial N_l}{\partial z} u_k d\Omega^e + C_v N_l \frac{\partial N_k}{\partial z} u_k \Big|_{R^e} - \int_{\Omega^e} N_k N_l \frac{\partial u_k}{\partial t} d\Omega^e = 0 \tag{3}$$

The second term in Equation (3) is the flux term, which is usually considered zero in the case of a 1D consolidation model. Thus, Equation (3) is reduced to:

$$\int_{\Omega^e} C_v \frac{\partial N_k}{\partial z}\frac{\partial N_l}{\partial z} u_k d\Omega^e - \int_{\Omega^e} N_k N_l \frac{\partial u_k}{\partial t} d\Omega^e = 0 \tag{4}$$

And FEM global matrix equation of 1D consolidation will be:

$$[KT]u + \left[BS\frac{\partial u}{\partial t}\right] = 0 \tag{5}$$

### 4.2 Settlement Calculation

To calculate the consolidation settlement of a compressible (clay) layer adjacent to a pumped aquifer using the TZP program, the layer is divided into smaller sub-layers, for each of which the incremental settlement can be calculated by the following relationship:

$$dS_i = h_i \left[ RR_i . \log \frac{\sigma'_p(i)}{\sigma'_v(i)} + CR_i . \log \frac{\sigma'_v(i) + \Delta\sigma_v(i) \pm \Delta u(i)}{\sigma'_P(i)} \right] \tag{6a}$$

$$S_c = \sum_{i=1}^{N} dS_i \tag{6b}$$

where: $S_c$ is the total settlement of the entire compressible layer;

$dS_i$ is the incremental settlement of the sub-layer i;

$h_i$, RR and CR are thickness, recompression ratio and compression ratio, respectively;

$\sigma'_p(i)$ is the maximum past pressure, usually determined from the oedometer test;

$\sigma'_v(i)$ is the vertical effective stress (effective overburden);

$\Delta\sigma'_v(i)$ is the change in vertical effective stress due to a surcharge loading on the surface;

$\Delta u(i)$ is the change in vertical effective stress due to pore pressure change (plus sign for deficit pore pressure due to pumping; while minus sign for excess pore pressure due to artificial recharge or natural recovery).

A number of consolidation analyses were performed to evaluate the impact of various hypothetical drawdowns of 2.0 m, 5.0 m, 10.0 m, and 15.0 m of the aquifer underlying the clay layer, which has properties as shown in Table 3. The results of the 1-year consolidation analysis, conducted over 12 months, are depicted in Figure 7. The long-term results, up to 25 years, can be seen in Figure 8. It can be observed that for drawdowns of 2.0 m or 5.0 m, the subsidence of the ground surface at the MAR reservoir site is still relatively small, with magnitudes of only a few millimeters, particularly during the first year of operation. However, as per the FEM consolidation analysis results shown in Figure 8, after 25 years of operation, cumulative subsidence may reach 25 cm and 33 cm for a drawdown of 10.0 m and 15.0 m, respectively. Comparison of the calculated settlement and the monitored ground deformation is shown in Figure 9.

**Table 3.** Geotechnical properties of clay layers used in 1D FEM consolidation analysis.

| Layer | Depth interval (m) | Thickness(m) | UW(kN/m$^3$) | $C_v$(m$^2$/y) | $C_c$ | $C_s$ | CR | RR | OCR |
|---|---|---|---|---|---|---|---|---|---|
| Clay | 10-30 | 20 m | 16.90 | 2.0 | 0.6 | 0.068 | 0.176 | 0.02 | 1.05 |

Note: $C_c$ (compression index), $C_s$ (recompression index), $C_v$ (vertical consolidation coefficient), CR (compression ratio), RR (recompression ratio), and OCR (over consolidation ratio).

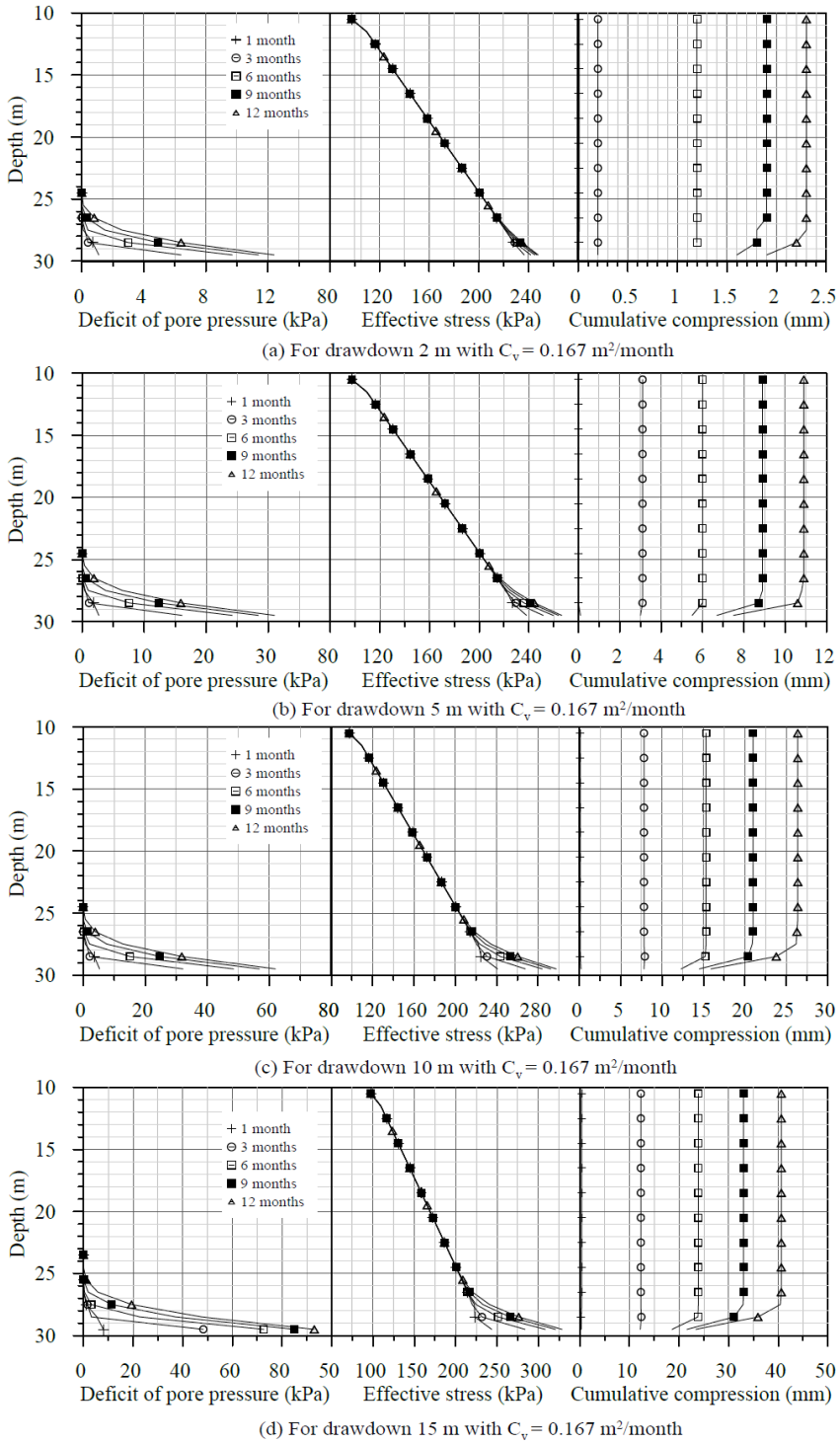


**Figure 7.** Results of 1-year consolidation analysis for the clay layer located from 10 to 30-m deep with $C_v$ = 2 m$^2$/y and different drawdowns: (a) 2.0 m; (b) 5.0 m; (c) 10.0 m; (d) 15.0 m.

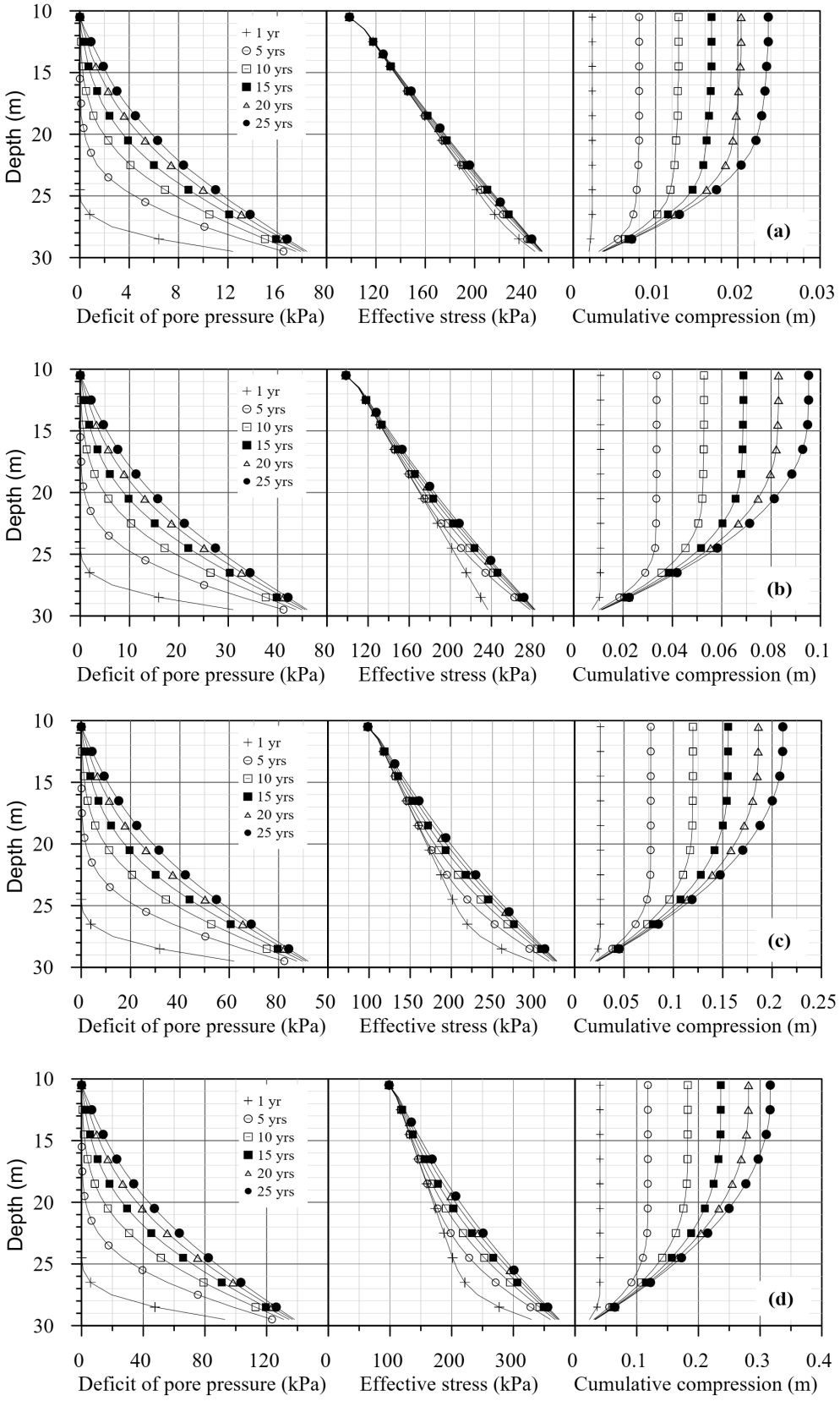


**Figure 8.** Results of 25-year consolidation analysis for the clay layer located from 10 to 30-m deep with $C_v$ = 2 $m^2$/y and different drawdowns: (a) 2.0 m; (b) 5.0 m; (c) 10.0 m; (d) 15.0 m.

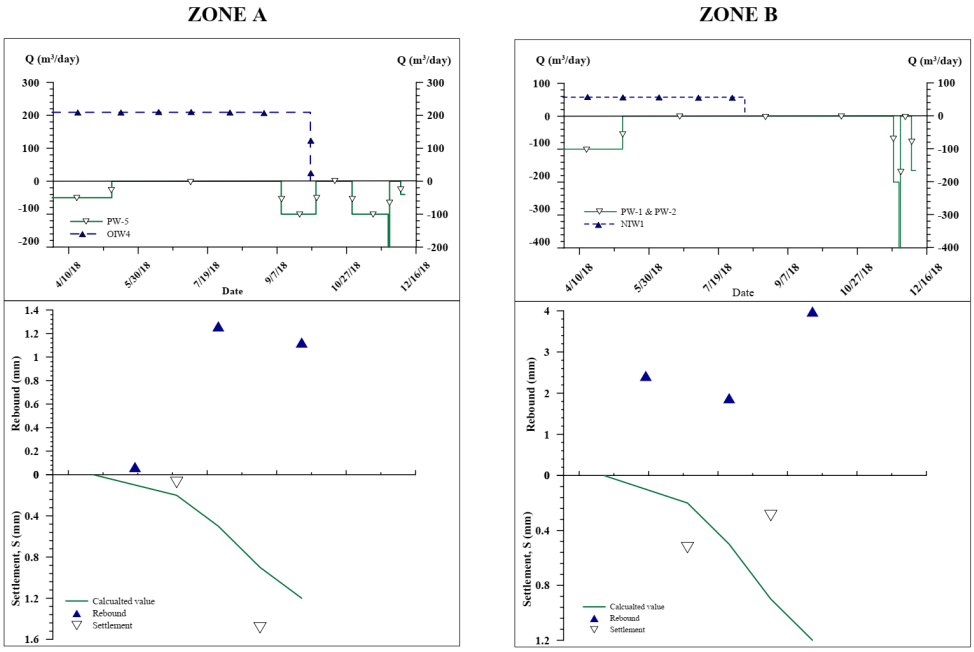


**Figure 9.** Comparison of the calculated settlement and monitored ground deformation.

As the consolidation analyses were performed with significantly higher pumping and injection rates than what was used in the pilot test (less than 500 $m^3$/d), it is expected that there will be no significant environmental impact caused by subsidence during the MAR test.

## 5. Results and Discussion

The results of the geotechnical and hydrogeological investigation conducted during field experiments at the experimental site of a subsurface reservoir in the coastal area of the Nakdong River plain led to the construction of a hydro-geotechnical model of the subsoil. The confined aquifer, where the subsurface reservoir was built, is located between 30 to 67 meters deep. In 2017 and 2018, a series of pumping and injection tests were conducted, and the pore pressure at the settlement monitoring data was obtained, demonstrating the smooth operation of the MAR test. To assess whether the constructed subsurface reservoir was fully utilized, post-experiment groundwater and consolidation analyses were carried out using the hydro-geotechnical model developed in this study. These results were used to create charts that determined the maximum allowable injection pressure and maximum recharge rate for the MAR test site in this study. The maximum injection head rise was theoretically calculated to be 14.5 meters. By considering two cases of a factor of safety (FS = 1.5 and 2.0), the maximum injection head rise was estimated to be 9.7 and 7.25 meters, corresponding to recharge rates of 5,000 $m^3$/d and 3,800 $m^3$/d, respectively.

## 6. Conclusions

A full-scale pilot field test of managed aquifer recharge (MAR) schemes, was successfully conducted in the Nakdong River plain, Korea as the first step of constructing a subsurface reservoir to store and supply clean water for a coastal area in the Nakdong plain, Busan, Korea. The following conclusions were drawn, and namely:

1) A hydrogeological-geotechnical model was successfully constructed based on the investigation data of the target aquifer which was located between 30 and 67 meters deep.

2) Based on the newly constructed subsurface model and geotechnical testing results a chart was created to determine the maximum injection pressure ($P_{max}$) and the maximum recharge rate ($Q_{max}$) for different scenarios of water injection into the subsurface reservoir in the future.

3) A 1D FEM consolidation code was revisited and employed to calculate the subsoil deformation, i.e., settlement or rebound due to pumping out or injection activities, respectively.

4) There is potential to increase the capacity of this subsurface reservoir in the future. The lessons learned from this pilot MAR test are expected to be useful for the construction of subsurface reservoirs at other coastal sites.

## Author Contributions

Both authors contribute equally to this research article. P.H.G.: FEM geotechnical analysis, model development,

manuscript writing, editing, revising. N.P.: funding, data acquisition, project management, manuscript editing, revising.

## Acknowledgement

This work was supported by the Dong-A University research fund.

## Conflict of Interest

There is no conflict of interest.

## References

[1] Pyne, R.D.G., 2005. Aquifer storage recovery, a guide to groundwater recharge through wells, 2nd edition. ASR Systems LLC: Gainesville. pp. 608.

[2] Casanova, J., Devau, N., Pettenati, M., 2016. Managed aquifer recharge: An overview of issues and options. Integrated groundwater management: Concepts, approaches and challenges. Springer, Cham.: Switzerland. pp. 413-434.

[3] International Association of Hydrogeologists—Commission on Managing Aquifer Recharge [Internet] [cited 2023 Mar 24]. Available from: https://recharge.iah.org/

[4] Dillon, P., Stuyfzand, P., Grischek, T., et al., 2019. Sixty years of global progress in managed aquifer recharge. Hydrogeology Journal. 27(1), 1-30. DOI: https://doi.org/10.1007/s10040-018-1841-z

[5] Sherif, M., Sefelnasr, A., Al Rashed, M., et al., 2023. A review of managed aquifer recharge potential in the Middle East and North Africa Region with examples from the Kingdom of Saudi Arabia and the United Arab Emirates. Water. 15(4), 742. DOI: https://doi.org/10.3390/w15040742

[6] Giao, P.H., 1996. Artificial recharge of Bangkok aquifer system for mitigatin of land subsidence [PhD thesis]. Bangkok: Asian Institute of Technology (AIT).

[7] Giao, P.H., Phien-Wej, N., Honjo, Y., 1998. FEM quasi-3D modelling of responses to artificial recharge in the Bangkok multiaquifer system. Environmental Modelling & Software. 14(2-3), 141-151.

[8] Giao, P.H., Paveechana, T., Saowiang, K. (editors), 2013. Consolidation settlement analysis with reference to groundwater recovery in the Bangkok multiaquifer system. The 1st Southeast Asian Geotechnical Conference cum Inaugural AGSSEA Conference, Advances in Geotechnical Infrastructure. Research Publishing: Singapore. p. 567-573.

[9] Phien-Wej, N., Giao, P.H., Nutalaya, P., 1998. Field experiment of artificial recharge through a well with reference to land subsidence control. Engineering Geology. 50(1-2), 187-201.

[10] Giao, P.H., Hue, V.T., Han, N.D., et al., 2020. Land subsidence prediction for a new urban mass rapid transit line in Hanoi. Underground Space. 5(2), 93-104. DOI: https://doi.org/10.1016/j.undsp.2018.11.002

[11] DAU, 2017. Internal Report of Geotechnical Investigation, Dong A University, Busan, Korea.

[12] Chung, S.G., Giao, P.H., Kim, G.J., et al., 2002. Geotechnical properties of Pusan clays. Canadian Geotechnical Journal. 39(5), 1050-1060.

Earth and Planetary Science
https://ojs.nassg.org/index.php/eps

RESEARCH ARTICLE

# Taxonomical Consideration, Phylogeny and Paleobiogeography of Some Argentinian Ypresian Benthic Foraminiferal Species

**Haidar Salim Anan**

Al Azhar University-Gaza, P.O Box 1277, Gaza, Palestine

ARTICLE INFO

*Article history*
Received: 19 February 2023
Revised: 7 April 2023
Accepted: 18 April 2023
Published Online: 28 April 2023

*Keywords*:
Paleontology
Eocene
Lineage
Paleogeography
Paleoenvironment
Argentina
Tethys

ABSTRACT

Rich and well preserved Argentinian taxa made it possible to correlate them with those previously identified species in the coeval sequence in different Tethyan North America, Europe and Middle East localities. This study deals with new information on paleontology and lineages of fourteen Argentinian Ypresian benthic foraminiferal species from the Punta Torcida Formation, lower-middle Eocene (Ypresian-lower Lutetian), Tierra del Fuego Island and Fuegian continental shelf, which belongs to twelve genera: *Laevidentalina*, *Lagenoglandulina*, *Tollmannia*, *Tristix*, *Leticuzonaria*, *Palmula*, *Leroyia*, *Marginulina*, *Ramulina*, *Orthokarstenia*, *Rectuvigerina* and *Pleurostomella*. Ten of the illustrated species are believed to be new: *Laevidentalina jannoui*, *Lagenoglandulina argentinica*, *Tollmannia argentinica*, *Leticuzonaria argentinica*, *Palmula americana*, *Leroyia argentinica*, *Marginulina argentinica*, *Ramulina subornata*, *Ramulina morsii* and *Rectuvigerina argentinica* sp. nov. The paleoenvironment of the Argentinian taxa would have been a shelf sea of normal salinity, where muds were deposited under low energy and low oxygen conditions, as is suggested by the dominance of infaunal morphotypes and excellent preservation of the tests, whereas intercalated sandstones reflect moderate energy and oxic conditions, bearing microfossil assemblages displaced from shallower settings.

## 1. Introduction

In this study, the fourteen recorded Eocene benthic foraminiferal species have been originally from Argentina by Jannou et al. [1,2]. It was followed by some other authors from the Southern and Northern Tethyan localities [3-17].

The present study deals with the taxonomic consideration of fourteen Argentinian Ypresian species of the two suborders Lagenid and Rotaliid of small benthic

*Corresponding Author:
Haidar Salim Anan,
Al Azhar University-Gaza, P.O Box 1277, Gaza, Palestine;
*Email: profanan@gmail.com; alazhar@alazhar-gaza.edu*

DOI: http://dx.doi.org/10.36956/eps.v2i1.815

foraminifera from the Punta Torcida Formation, lower-middle Eocene (Ypresian-lower Lutetian), Tierra del Fuego Island and Fuegian continental shelf (Figure 1). The present study aims at throwing light on: 1) to present together many data scattered in the literature for the members of nine Lagenid foraminiferal genera: *Laevidentalina, Lagenoglandulina, Tollmannia, Tristix, Leticuzonaria, Palmula, Leroyia, Marginulina, Ramulina,* and three Rotaliid foraminiferal genera: *Orthokarstenia, Rectuvigerina, Pleurostomella* under a unifying theme, 2) to detect its paleontology, stratigraphy and paleogeographic distribution of the different species of that genera, 3) to discuss the taxonomic status of the Argentinian species with the other related species, in the other localities in the Tethys, 4) to present ten species, which are believed to be new: *Laevidentalina jannoui*, *Lagenoglandulina argentinica*, *Tollmannia argentinica, Leticuzonaria argentinica, Palmula americana, Leroyia argentinica, Marginulina argentinica, Ramulina subornata, Ramulina morsii* and *Rectuvigerina argentinica*. The recorded species from Argentina and other localities in the Tethys are distributed in a wide paleogeographic area in the world throughout the open Tethys in the Ypresian time.

## 2. Material of Study

The identified Argentinian benthic foraminifera are recorded from the Punta Torcida Formation, lower-middle Eocene (Ypresian-lower Lutetian), Tierra del Fuego Island and Fuegian continental shelf, which yielded 161 species of benthic foraminifera. Twenty-four of these species have a tight relation with many diagnostic Tethyan species recorded from USA, Europe and south Mediterranean Sea localities. Following the Code of Zoological Nomenclature, a taxonomic revision of ten of the Argentinian species are re-described its morphological features, which considered here as a new species: *Laevidentalina jannoui, Lagenoglandulina argentinica, Tollmannia argentinica, Leticuzonaria argentinica, Palmula americana, Leroyia argentinica, Marginulina argentinica, Ramulina subornata, Ramulina morsii* and *Rectuvigerina argentinica.*

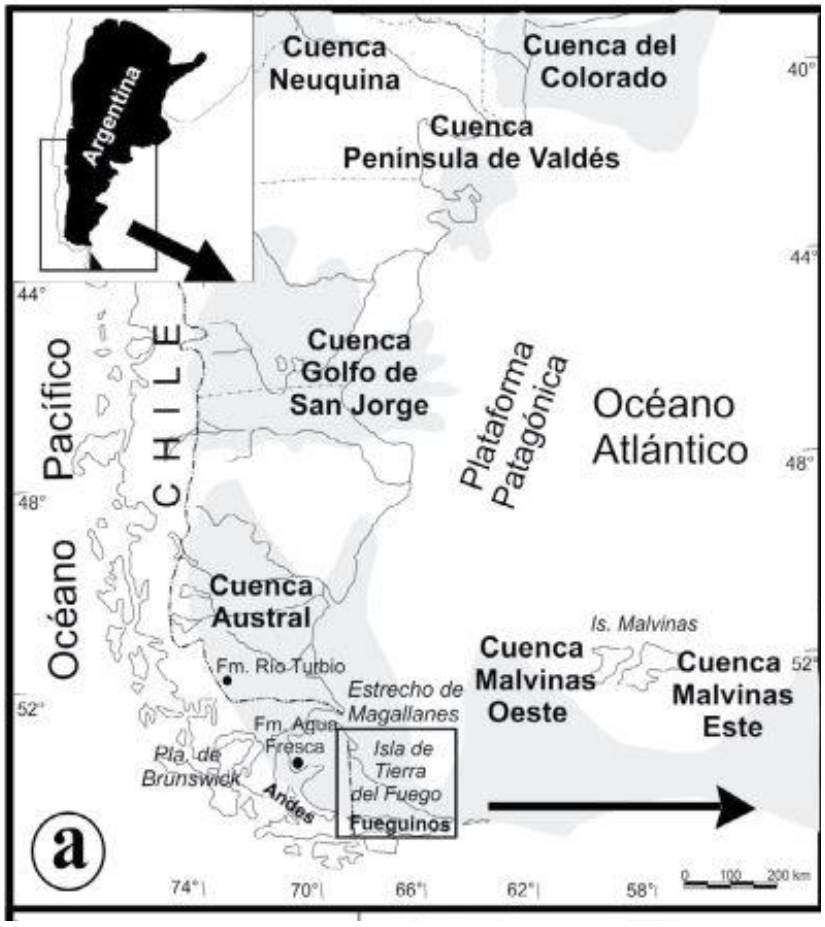

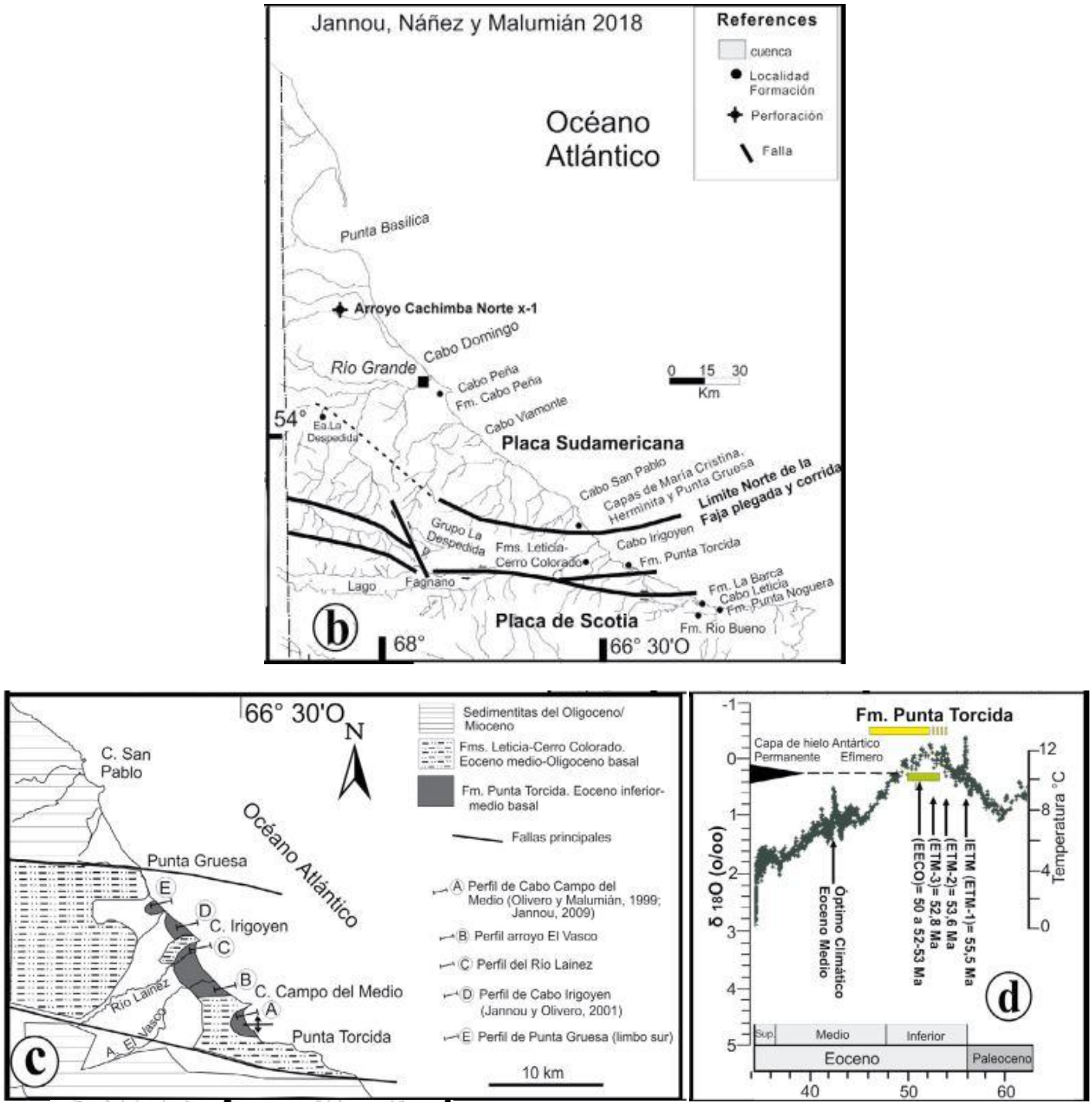


**Figure 1.** a) Location map of the study area (in box) of south Argentina in the Southern America, South Atlantic Ocean, b) details of the study area, c) geological map of de la Isla Grande de Tierra del Fuego, d) the temperature curve δ 18O depends on the benthic foraminifera in the Punta Torcida Formation [2].

## 3. Taxonomy

The taxonomy of Loeblich & Tappan [3] is followed here for the recorded twenty-four benthic foraminiferal species belonging to twelve genera, which were recorded from the Ypresian of Argentina and other Tethyan countries, and illustrated in Plate 1.

Order Foraminiferida Eichwald, 1830

Suborder Lagenina Delage & Hérouard, 1896

Genus *Laevidentalina* Loeblich & Tappan, 1986

Type species *Laevidentalina aphelis* Loeblich & Tappan, 1955

***Laevidentalina jannoui* Anan, sp. nov.** (Plate 1, Figure 1) (= *Dentalina* sp.—Jannou [1], p. 177, Figure 6F; *Laevidentalina* sp. B—Jannou et al. [2]., p. 36, Plate 2, Figure 6) ● {illustrated specimen}.

Holotype: Illustrated specimen in Plate 1, Figure 1.

Dimension: Length 1.1 mm.

Etymology: In the honor of the micropaleontologist Jannou in Argentine Mining Geological Service.

Type locality and sample: Formación Punta Torcida, CCM: Mbros. PTa & PTb, SEGEMAR 2850, CM-2L. (SEGEMAR = Servicio Geológico Minero Argentino)

Stratigraphic level: Ypresian (Early Eocene).

Diagnosis: This species is characterized by an elongate and arcuate test with gradually growing, smooth surface, parallel sides, nearly globular chambers, globular pro-loculus and apiculate, flush sutures in the lower part but depressed in the upper part, aperture terminal.

Remarks: The Argentinian Ypresian *Laevidentalina jannoui* n. sp. is most probably evolved from the Pale-

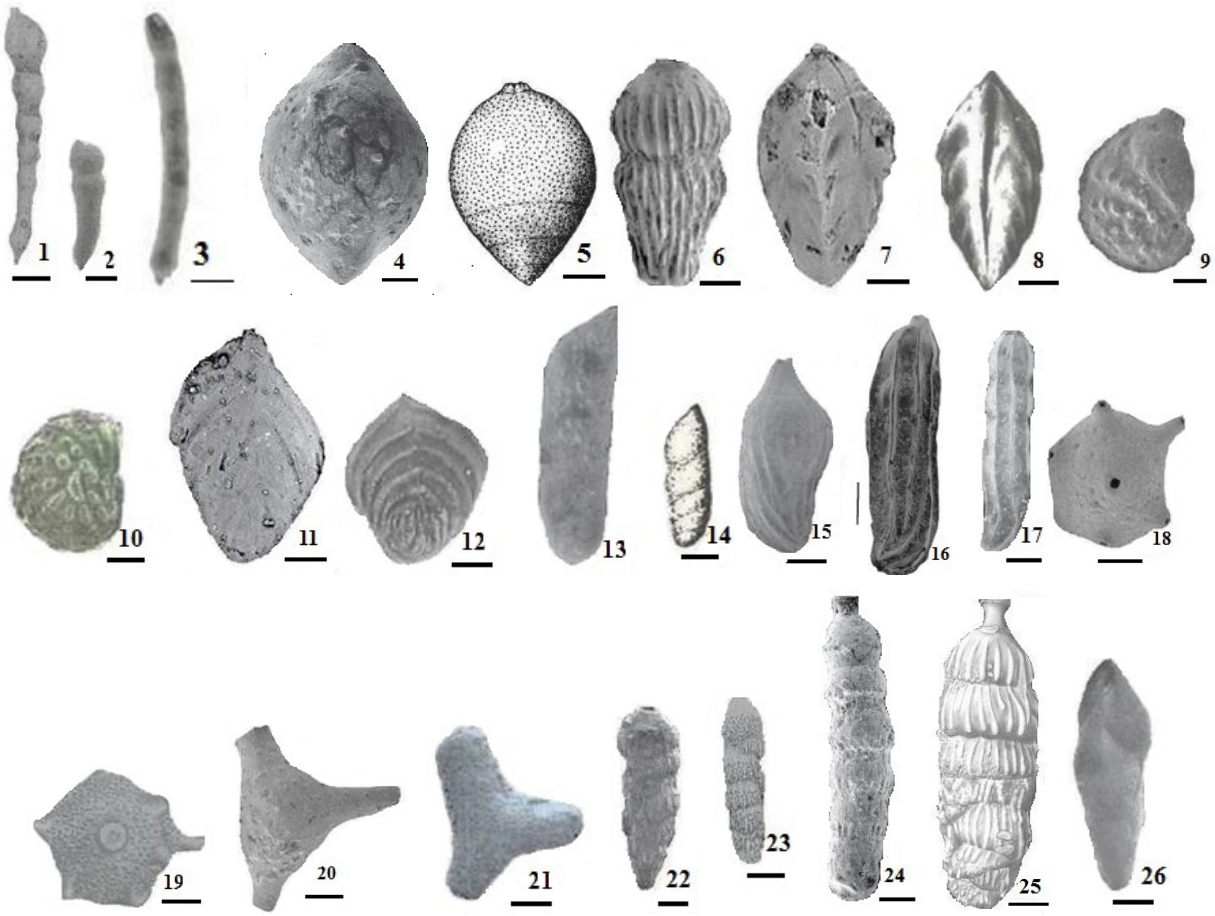


**Plate 1.** Figure 1. *Laevidentalina jannoui* Anan, sp. nov., 2. *Laevidentalina hudae* Anan [4], 3. *Laevidentalina salimi* Anan [5], 4. *Lagenoglandulina argentinica* Anan, sp. nov., 5. *Lagenoglandulina annulata* (Stache [6]), 6. *Tollmannia argentinica* Anan, sp. nov, 7, 8. *Tristix aubertae* Anan [7], (7. from Argentina, 8. from Egypt), 9. *Leticuzonaria argentinica* Anan, sp. nov., 10. *Leticuzonaria misrensis* Anan [8], 11. *Palmula americana* Anan, sp. nov., 12. *Palmula sagittaria* Lea [9], 13. *Leroyia argentinica* Anan, sp. nov., 14. *Leroyia aegyptiaca* Anan [10], 15. *Marginulina argentinica* Anan, sp. nov., 16, 17. *Marginulina costata* [11], (16. from Egypt, 17. from Argentina), 18. *Ramulina subornata* Anan, sp. nov., 19. *Ramulina ornata* Cushman [12], 20. *Ramulina morsii* Anan, sp. nov., 21. *Ramulina ismaili* Anan [13], 22. *Orthokarstenia higazyi* [14], 23. *Orthokarstenia eleganta* [15], 24. *Rectuvigerina argentinica* Anan, sp. nov., 25. *Rectuvigerina multicostata* Cushman & Jarvis [16], 26. *Pleurostomella acuta* Hantken [17]. (scale bar = 100 μm)

ocene *L. hudae* Anan [4] (Plate 1, Figure 2), (from Jabal Mundassa, United Arab Emirates, UAE) and considered here as the ancestor of the Middle-Late Eocene *L. salimi* Anan [5] (Plate 1, Figure 3) (from Jabal Hafit, UAE) (Figure 2) in the *Laevidentalina hudae* → *L. jannoui* → *L. salimi* lineage.

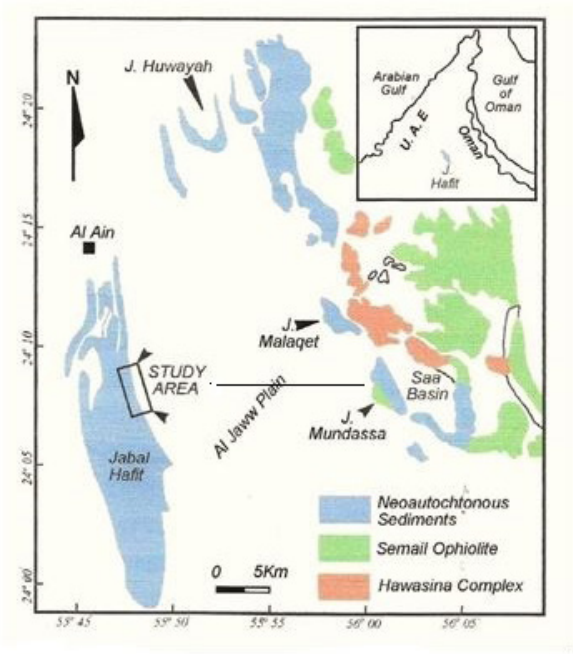


**Figure 2.** Location map of Jabal Mundassa and Jabal Hafit, Al Ain area, UAE (the type sections of *Laevidentalina hudae* and *L. salimi*).

Genus *Lagenoglandulina* A. Silvestri, 1923

Type species: *Glandulina subovata* = *Lagenoglandulina annulata* (Stache, 1864)

***Lagenoglandulina argentinica* Anan**, sp. nov. (Plate 1, Figure 4) (= *Lagenoglandulina* A. Silvestri [18], p. 12; *Lagenoglandulina* sp.—Jannou et al. [2], p. 36, Plate 3, Figure 3).

Holotype: Illustrated specimen in Plate 1, Figure 4.

Dimension: Length 0.55 mm, width 0.40 mm.

Etymology: After the State of Argentina.

Type locality and sample: Formación Punta Torcida, CM-13a, SEGEMAR 2873.

Stratigraphic level: Ypresian

Diagnosis: Test ovate and circular in section with few rectilinear chambers, which increase rapidly in breadth as added and strongly overlap the earlier chambers, sutures obscure in the early part, surface finally scattered knobs, aperture terminal and radiate at the end of a short cylindrical neck.

Remarks: *Lagenoglandulina argentinica* differs from *L. annulata* (Plate 1, Figure 5) in its finally scattered knobs on the surface than the smooth surface of the holotype. The members of this genus were recorded from Caribbean, Italy, New Zealand, and now from Argentina.

Genus *Tollmannia* Sellier de Civrieux and Dessauvagie, 1965

Type species: *Lingulina costata* subsp. *tricarinata* Tollmann, 1954 = *Lingulina costata* d'Orbigny, 1846.

***Tollmannia argentinica* Anan**, sp. nov. (Plate 1, Figure 6) (=Lingulina sp.—Jannou[1], p. 101, Figure 6L; *Amplectoductina multicostata* (Galloway & Morrey)—Jannou et al. [2], p. 20, Plate 2, Figure 12).

Holotype: Illustrated specimen in Plate 1, Figure 6.

Dimensions: Length 4.8 mm, width 2.5 mm.

Etymology: After the State of Argentina.

Type locality and sample: Formación Punta Torcida, CI-20, SEGEMAR 2856.

Stratigraphic level: Ypresian

Diagnosis: Test large up to 4.5 mm in length, circular to ovate in section, chambers increase rapidly in breadth as added and strongly overlap previous chambers, final chamber comprising one-third the length of the test, sutures horizontal, moderately depressed, surface with longitudinal ribs that may completely cross the chambers, aperture terminal, circular, bordered by an elevated lip.

Remarks: The genus has longitudinal costae, and nearly circular in section. The *Tollmannia argentinica* sp. nov. is characterized by an elongated test, globular-semi globular uniserial chambers, longitudinal ribs on the surface, and a rounded aperture with the small elevated neck. The Early Eocene *T. argentinica* most probably may develop into the youngest Miocene species *T. costata* (d'Orbigny).

Genus *Tristix* Macfadyen, 1941

Type species *Rhabdogonium liasinum* Berthelin, 1879

***Tristix aubertae* Anan**, 2002 (Plate 1, Figures 7, 8) (=*Tristix auberti* Anan [7], p. 634, Figure 2. 6; *Tristix aubertae* Anan - Anan [19], p. 304, Plate 1, Figure 2; *Tristix* sp.—Jannou [1], p. 179, Figure 7I; *Tristix* sp.—Jannou et al. [2], p. 44, Plate 3, Figure 4).

Type locality and sample in Argentina: Formación Punta Torcida, PTma-2, SEGEMAR 2874.

Remarks: The Argentinian Ypresian figured specimen of Jannou et al. [2], is conspecific to the Egyptian Paleocene *T. aubertae* (triangular test face, flattened, concave triangular chamber). It means that this species has wide geographic distribution from the Southern Tethys (Egypt) to Southern Atlantic (Argentina), which proves the open sea water between these wide areas (Figure 3).

Genus *Leticuzonaria* Anan, 2021

Type species *Leticuzonaria hodae* Anan, 2021

***Leticuzonaria argentinica* Anan**, sp. nov. (Plate 1, Figure 9) (= *Marginulina asperuliformis* [20]—Jannou [1], p. 179, Figure 7P (*non* Figures 7N, 7O); *Marginulina asper-*

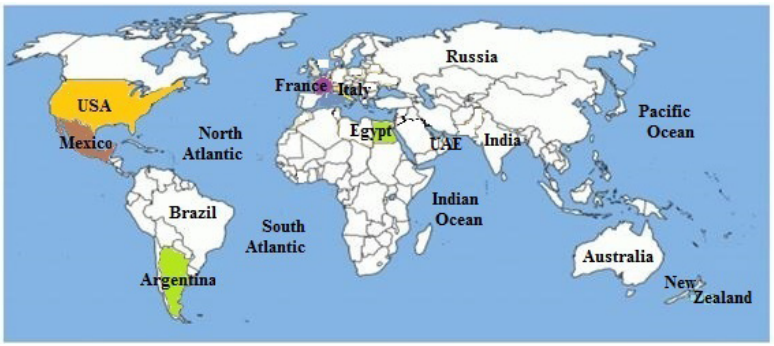


**Figure 3.** A map of the world showing the geographic distribution of some benthic foraminiferal species in many different countries: North America (USA, Mexico), South America (Argentina), West Europe (France, Italy, Hungaria), North Africa (Egypt), Southwest Asia (UAE), South Pacific Ocean (New Zealand).

*uliformis* (Nuttall)—Jannou et al. [2], p. 38, Plate 2, Figure 16.

Holotype: Illustrated specimen in Plate 1, Figure 9.

Dimension: Length 0.55 mm.

Etymology: After the Argentina State.

Type locality and sample: Formación Punta Torcida, AV-5, SEGEMAR 2860.

Stratigraphic level: Ypresian.

Diagnosis: The Ypresian figured specimen of Jannou et al. [2] (p. 38, Plate 2, Figure 16) belongs here to the genus *Leticuzonaria* Anan [8], Plate 1, Figure 10), not to *Marginulina* with the slightly coiled initial stage, followed by uniserial inflated chambers.

Remarks: The new species *Leticuzonaria argentinica* differs from *L. hodae* Anan [8] (from Egypt) by lacking a spinose surface and elongated last chamber, and protruding development of the aperture.

Genus *Palmula* Lea, 1833

Type species *Palmula sagittaria* Lea, 1833

***Palmula americana* Anan**, sp. nov. (Plate 1, Figure 11) (= *Palmula* sp. cf. *P. magallanica* Todd & Kniker [21]Jannou [1]), p. 179, Figure 7B; *Palmula* sp. cf. *P. magallanica* Todd & Kniker—Jannou et al. [2]), p. 38, Plate 2, Figure 23) .

Holotype: Illustrated specimen in Plate 1, Figure 11.

Dimension: Length 1.5 mm, width 0.75 mm.

Etymology: After the geographic location from South America.

Type locality and sample in Argentina: Formación Punta Torcida, PTma-2, SEGEMAR 2867. Stratigraphic level: Ypresian.

Diagnosis: This species has large, elongate and flattened test, enrolled planispiral early stage, later uncoiled and rectilinear, broad and chevron shaped chambers, which increasing gradually in breadth, periphery rounded, sutures slightly depressed, surface smooth, aperture terminal and radiate.

Remarks: This species is characterized by a compressed palmate test with small coiled stage, and distinct slightly raised sutures. It differs from the holotype of the genus *Palmula sagittaria* (Plate 1, Figure 12) (after Loeblich & Tappan [3]) in its elongated larger test, smaller early planispirally stage, and slightly depressed sutures than raised.

Genus *Leroyia* Anan, 2020

Type species *Leroyia aegyptiaca* Anan, 2020

***Leroyia argentinica* Anan**, sp. nov. (Plate 1, Figure 13) (= *Lenticulina* sp.—Jannou [1], p. 179, Figure 6K—*Marginulina* ex gr. *M. hochstetteri* Stache [6]—Jannou et al. [2], p. 38, Plate 2, Figure 17).

Holotype: Illustrated specimen in Plate 1, Figure 13.

Dimensions: Length 0.55 mm, width 0.15 mm.

Etymology: After the state of Argentina.

Type locality and sample: Formación Punta Torcida, CM-4a, SEGEMAR 2855, CM-145.

Stratigraphic level: Ypresian.

Diagnosis: This Ypresian species has elongate test, minute indistinct early coiled stage, later 7-10 uniserial inflated chambers, which increasing in length as added, sutures slightly depressed and moderately oblique, peripheral margins rounded, surface smooth, aperture radiate extended at dorsal angle.

Remarks: It seems that the Ypresian new species *L. argentinica* was evolved from Thanetian-Ypresian *L. aegyptiaca* (from Egypt) in the *L. aegyptiaca* → *L. argentinica* lineage.

Genus *Marginulina* d'Orbigny, 1826

Type species *Marginulina raphanus* d'Orbigny, 1826

***Marginulina argentinica* Anan,** sp. nov. (Plate 1, Figure 15) (= *Lenticulina* sp.—Jannou [1], p. 179, Figure 6U; *Marginulina* sp.—Jannou et al. [2], p. 38, Plate 2, Figure 21).

Holotype: Illustrated specimen in Plate 1, Figure 15.

Dimension: Length 0.66 mm, width 0.33 mm.

Type locality and sample: Formación Punta Torcida, CM-180, SEGEMAR 2865.

Stratigraphic level: Ypresian.

Diagnosis: The *Marginulina argentinica* is characterized by a short test, slightly coiled initial stage, uniserial later stage with inflated chambers, surface with about 20 longitudinal costae, extended over the sutures, straight and slightly depressed sutures in the uniserial part, but indistinct in the initial part, aperture terminal on a long neck.

Remarks: This species differs from the *Marginulina costata* (Batsch [11], Plate 1, Figures 16, 17) by smaller test, more inflated uniserial stage, and more numbers of longitudinal costae. Most probably Early Eocene *L. argentinica* was developed into Middle-Late Eocene *L. costata* in the *M. argentinica* → *M. costata* lineage.

***Marginulina costata* (Batch, 1791)** (Plate 1, Figures 16, 17) (=*Nautilus (Orthoceras) costatus* Batsch [11], p. 2, Plate 1, Figure 1; *Marginulina costata* (Batsch)—Anan [22], 1994, p. 223, Figure 8. 17, 18; *Dentalina elgansoensis* Todd & Kniker [21]—Jannou et al. [2], p. 33, Plate 2, Figures 3,4).

Remarks: This species was recorded in the Middle-Late Eocene of Egypt [22], but only in the Middle Eocene of UAE [5], and now is recorded in the Early Eocene of Argentina (Formación Punta Torcida, CM-1a).

Genus *Ramulina* Jones, 1875

Type species *Ramulina laevis* Jones, 1875

***Ramulina subornata* Anan**, sp. nov. (Plate 1, Figure 18) (= *Ramulina* sp. cf. *globulifera* Brady [23]),—Jannou [1], p. 104, Figure 7F).

Holotype: Illustrated specimen in Plate 1, Figure 18.

Dimension: Length 2. 8 mm.

Etymology: Unornate, smooth.

Type locality and sample: Formación Punta Torcida, AV mbro. PTa, AV-1, SEGEMAR 2871.

Stratigraphic level: Ypresian.

Diagnosis: This Ypresian species has a globular chamber with sixth rounded spinose projections with numerous radiate tubular processes, surface is smooth, not ornate.

Remarks: This species (from Argentina) differs from the American *R. ornata* Cushman [12] (Plate 1, Figure 19) by its smooth surface, not spinose projections on the surface, and 6 homogeneous distribution of the arms.

***Ramulina morsii* Anan**, sp. nov. (Plate 1, Figure 20) (=*Ramulina* sp.—Jannou [1], p. 104, Figure 7G; *Ramulina* sp.—Jannou et al. [2], p. 24, Plate 3, Figure 2).

Holotype: Illustrated specimen in Plate 1, Figure 20.

Dimension: Length 5.0-5.5 mm.

Etymology: In the honor of Prof. A. Morsi, Department of Geology, Ain Shams Univ., Egypt.

Type locality and sample: Formación Punta Torcida, AV mbro. PTa, AV-1, SEGEMAR 2872.

Stratigraphic level: Ypresian.

Diagnosis: This Ypresian species has radiating three triangular tubular thick extinctions of the chamber, and mainly with small projections surface.

Remarks: *Ramulina morsii* n. sp. (from Argentina) differs from *R. ismaili* Anan [13] (p. 2, Figure 2. 6) (from Egypt) by less thick elongate tapering tubular projection, and ornamented surface. The Maastrichtian–Paleocene *R. ismaili* (Plate 1, Figure 21) most probably was developed to the Early Eocene *R. morsii* in its ornamented globular body and thicker elongated tapering three tubular arms. It seems that *R. ismaili* was developed to *R. morsii* in the *R. ismaili* → *R. morsii* lineage.

Suborder Rotaliina Delage & Hérouard, 1896

Genus *Orthokarstenia* Dietrich, 1935

Type species *Orthocerina ewaldi* Karsten, 1858

***Orthokarstenia higazyi*** [14] (Plate 1, Figure 22) (= *Siphogenerina higazyi* Nakkady [14], p. 705, text-Figure 4; *Orthokarstenia higazyi* (Nakkady)—Anan & Sharabi [24], p. 212, Plate 2, Figures 8, 9; *Loxostomina* sp. aff. *L. eleganta* [15]—Jannou et al. [2]), p. 24, Plate 3, Figure 16 (*non* Figures 13-15).

Remarks: Anan [8] noted that the cosmopolitan Thanetian-Ypresian *O. eleganta* [15] has mainly smooth surface (without ribs, but with indistinct and irregularly longitudinal striation in the very earliest portion of the test), while the Paleocene species *O. higazyi* [14] has longitudinal costae covers all of the chambers. The existed of longitudinal costae separates the Paleocene *O. higazyi* from the smooth test surfaces of both the Maastrichtian *O. esnehensis* [25], and the Paleocene-Early Eocene *O. eleganta* (Plate 1, Figure 23). It is, so far recorded from Egypt, Jordan, UAE and Argentina.

Genus *Rectuvigerina* Mathews, 1945

Type species *Siphogenerina multicostata* Cushman & Jarvis, 1929

***Rectuvigerina argentinica* Anan**, sp. nov. (Plate 1, Figure 24) (= *Stilostomella* sp. Jannou et al. [2], p. 42, Plate 3, Figure 19).

Holotype: Illustrated specimen in Plate 1, Figure 24.

Dimension: Length 0.62 mm, width 0.13 mm.

Etymology: After the State of Argentina.

Type locality and sample: Formación Punta Torcida, CM-151, SEGEMAR 2889.

Stratigraphic level: Ypresian.

Diagnosis: *Rectuvigerina jannoui* Anan, sp. nov. has elongate and slightly arcuate hyaline test, small involute triserial early stage followed by elongata uniserial stage, gradually grow globular to discoidal chambers, short ribs at the base of the chambers, proloculus globular, but not apiculate, sutures slightly depressed in early stage, but depressed in later stage, aperture terminal on neck with a phialine lip.

Remarks: The *Rectuvigerina jannoui* differs from the holotype *R. multicostata* Cushman & Jarvis [16] (Plate 1, Figure 25) by non-ribbed ornamented test without crossing the sutures, doesn't have an intervening biserial stage, and more number (6 instead of 3) of elongated uniserial stage.

Genus *Pleurostomella* Reuss, 1860

Type Species *Dentalina subnodosa* Reuss, 1860

***Pleurostomella acuta* Hantken, 1875** (Plate 1, Figure 26) (= *Pleurostomella acuta* Hantken [17], 1875, p. 37, Plate 13, Figure 18 - Anan [26], p. 174, Plate 1, Figure 1—Jannou et al. [2], p. 31, Plate 5, Figures 33, 34).

Type locality and sample: Formación Punta Torcida, CM-134, SEGEMAR 2975.

Remarks: This cosmopolitan species has an elongate test, and is circular in cross-section, with biserial early-stage chambers increasing gradually in size, and final pair of chambers with extremely inflated, sutures slightly depressed and strongly curved, wall calcareous hyaline smooth, aperture terminal with the large oval opening of the final chamber, and characterized by its diagnostic apertural tooth. It was recorded from the Maastrichtian-Paleocene of the Atlantic Ocean [27,28], Thanetian-Ypresian of France [29], Italy [30] and USA [31], Ypresian from Argentina [2], but Lutetian-Bartonian from Hungaria [32].

## 4. Paleogeography

The identified species have wide geographic distribution: North Atlantic (USA, Mexico, Caribbean), South Atlantic (Argentina), Europe (France, Germany, Hungaria, Italy), Northeast Africa (Egypt), Southwest Asia (Jordan), and Southwest Pacific (New Zealand) (see Figure 3).

Moreover, the paleogeographic maps recorded by many authors [33-36] show the Tethyan realm had been connected with the Atlantic Ocean from west to the Indo-Pacific Ocean to the east, via the Mediterranean Sea, crossing the Middle East region during the Paleogene time. Another author [37-39] expressed that the extended realms of the

**Table 1.** Paleogeographic distribution of the Early Eocene twenty-four Lagenid and Rotaliid benthic foraminiferal species in the Punta Torcida Formation (Early Eocene), Tierra del Fuego Island and Fuegian continental shelf and other Tethyan localities.

| Sp. No. | species | countries | 1 | 2 | 3 | 4 | 5 | 6 | 7 | 8 | 9 | 10 | 11 | 12 |
|---|---|---|---|---|---|---|---|---|---|---|---|---|---|---|
| 1 | *Laevidentalina* | *jannoui* | x | - | - | - | - | - | - | - | - | - | - | - |
| 2 | | *hudae* | - | - | - | - | - | - | - | - | - | - | x | - |
| 3 | | *salimi* | - | - | - | - | - | - | - | - | - | - | x | - |
| 4 | *Lagenoglandulina* | *argentinica* | x | - | - | - | - | - | - | - | - | - | - | - |
| 5 | | *annulata* | - | x | - | - | - | x | x | - | - | - | - | x |
| 6 | *Tollmannia* | *argentinica* | x | - | - | - | - | - | - | - | - | - | - | - |
| 7 | *Tristix* | *aubertae* | x | - | - | - | - | - | - | - | x | - | - | - |
| 8 | *Leticuzonaria* | *argentinica* | x | - | - | - | - | - | - | - | - | - | - | - |
| 9 | | *misrensis* | - | - | - | - | - | - | - | - | x | - | - | - |
| 10 | *Palmula* | *americana* | x | - | - | - | - | - | - | - | - | - | - | - |
| 11 | | *sagittaria* | - | - | x | - | - | - | - | - | - | | - | - |
| 12 | *Leroyia* | *argentinica* | x | - | - | - | - | - | - | - | - | - | - | - |
| 13 | | *aegyptiaca* | - | - | | - | - | - | - | - | x | - | - | - |
| 14 | *Marginulina* | *argentinica* | x | - | - | - | - | - | - | - | - | - | - | - |
| 15 | | *costata* | x | - | - | - | x | - | - | - | x | - | - | - |
| 16 | *Ramulina* | *subornata* | x | - | - | - | - | - | - | - | - | - | - | - |
| 17 | | *ornata* | - | - | x | - | - | - | - | - | - | - | - | - |
| 18 | | *morsii* | x | - | - | - | - | - | - | - | - | - | - | - |
| 19 | | *ismaili* | - | - | - | - | - | - | - | - | x | - | - | - |
| 20 | *Orthokarstenia* | *higazyi* | - | - | - | - | - | - | - | - | x | x | - | - |
| 21 | | *eleganta* | x | - | x | - | - | - | - | - | - | - | - | - |
| 22 | *Rectuvigerina* | *argentinica* | x | - | - | - | - | - | - | - | - | - | - | - |
| 23 | | *multicostata* | - | - | x | - | - | - | - | - | - | - | - | - |
| 24 | *Pleurostomella* | *acuta* | x | - | - | - | - | - | - | x | - | - | - | - |

1. Argentina, 2. Caribbean, 3. USA, 4. Atlantic Ocean, 5. France, 6. Germany, 7. Italy, 8. Hungaria, 9. Egypt, 10. Jordan, 11. UAE, 12. New Zealand. Sp. No. = Species number, x=recorded,—not recorded.

Tethys have extended from the Indo-Pacific to the Atlantic Oceans and the Mediterranean Sea during the Late Cretaceous to Paleogene times, and the fauna exhibit pronounced similarities (Figure 4).

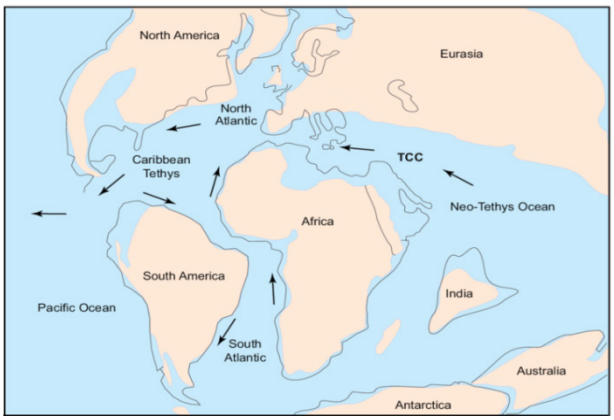


**Figure 4.** Paleogeography of the Neo-Tethys Ocean during the Maastrichtian-Ypresian time showing the flow direction of the Tethyan Circumglobal Current (TCC) from east to west, and the location of North and South America, Eurasia, Africa, India and Australia [40].

## 5. Paleoecology and Paleoenvironment

Jannou [1] noted that the small, weakly calcified tests and marked infaunality of the benthic calcareous foraminiferal assemblages, added to the occurrence of acarininid planktic foraminifera, suggest relatively warm waters, correlatable with the post maximum thermal Eocene-3 (~52 Ma). Jannou et al. [2] noted that the paleoenvironment of South Argentina would have been a shelf sea of normal salinity, where muds were deposited under low energy and low oxygen conditions, as is suggested by the dominance of infaunal morphotypes and excellent preservation of the tests, whereas intercalated sandstones reflect moderate energy and oxic conditions, bearing microfossil assemblages displaced from shallower settings. The foraminifera taxa in the study section of Argentina have similarities with those of the Eocene of the Austral basin, Australia, New Zealand and the Antarctic, reflecting the southern nature of the microfauna. Anan [41] noted that the probable environment of northern Egypt is outer neritic-upper bathyal, while deeper in central Egypt, are deposited in the middle-outer neritic. The *Lenticuzonaria misrensis*, *Tristix aubertae*, *Leroyia aegyptiaca*, *Orthokarstenia higazyi* were recorded from central and southern Egypt, which located in the Nile Valley Facies (NVF), of Issawi et al. [42], which has middle-outer neritic environmental facies by some authors (e.g. Nakkady [43], LeRoy [44]) and considered here to be related to the Midway-Type Fauna (MTF) of Berggren & Aubert [45]. Hayward et al. [46] noted the paleobathymetric distribution of Pleurostomella acuta in present-day depth ranges of sites in the lower bathyal to middle abyssal.

## 6. Conclusions

The present study deals with the recording of twenty-four diagnostic identified Early Eocene species of Lagenid and Rotaliid calcareous foraminiferal genera which needs a taxonomic revision to accommodate the modern nomenclature among more than 160 species of Argentina. Ten out of these species are believed here as new: *Laevidentalina jannoui, Lagenoglandulina argentinica, Tollmannia argentinica, Leticuzonaria argentinica, Palmula americana, Leroyia argentinica, Marginulina argentinica, Ramulina subornata, Ramulina morsii* and *Rectuvigerina argentinica* sp. nov. Some of the identified species are confined to Argentina, but some others were recorded from many localities in North America (USA, Mexico), Europe (France, Italy) North Africa (Egypt), Southwest Asia (Jordan) and South Pacific (New Zealand). The extended realms of the Tethys have extended from the Indo-Pacific to the Atlantic Oceans via the Mediterranean Sea during the Ypresian time, and the fauna exhibit pronounced similarities.

## Acknowledgement

The author would like to express his sincere appreciation to the editor of EPS for continuous efforts, and unknown reviewer for improving the original manuscript and contributing valuable comments. I am also indebted to my daughter Dr. Huda Anan for help in the development of the figures and plate.

## Conflict of Interest

There is no conflict of interest.

## References

[1] Jannou, G.E., 2009. Microfósiles Marinos del Eoceno inferior, Isla Grande de Tierra Del Fuego, Argentina: bioestratigrafía, paleoambiente y paleobiogeografía (Spanish) [Marine microfossils of the lower Eocene, Isla Grande de Tierra Del Fuego, Argentina: biostratigraphy, paleoenvironment and paleobiogeography] [PhD thesis]. Biblioteca Digital, Universidad de Buenos Aires (UBA), Facultad de Ciencias Exactas Naturales (FCEN). p. 1-228.

[2] Jannou, G.E., Náñez, C.A., Malumián, N., 2022. Foraminíferos bentónicos de la Formación Punta Torcida, Eoceno inferior-medio (YpresianoLutetiano inferior), Isla Grande de Tierra del Fuego y plataforma

continental fueguina (Spanish) [Benthic foraminifera from the Punta Torcida Formation, Lower-Middle Eocene (Lower Ypresian-Lutetian), Isla Grande de Tierra del Fuego and Tierra del Fuego continental shelf]. Serie Contribuciones Técnicas. Geología Regional. 9, 53.

[3] Loeblich, A.R., Tappan, H., 1988. Foraminiferal genera and their classification. Springer: Berlin.

[4] Anan, H.S., 2015. Paleocene Lagenid benthic foraminifera of Jabal Mundassa, Al Ain Area, United Arab Emirates. Egyptian Journal of Paleontology. 15, 61-83.

[5] Anan, H.S., 2009. Paleontology and stratigraphical distribution of suborder Lagenina (benthic foraminifera) from the Middle-Late Eocene Mazyad Member of the Dammam Formation in Jabal Hafit, Al Ain area, United Arab Emirates, northern Oman Mountains. Revue de Paléobiologie. 28(1), 1-18.

[6] Stache, G., 1864. Die Foraminiferen der tertiären Mergel des Whaingaroa-Hafens (Prov. Auckland), Novara-Expedition, 1857-1859 (German) [The foraminifera of the tertiary marls of Whaingaroa Harbor (Prov. Auckland), Novara Expedition, 1857-1859]. Geologische Theil. 1(2), 159-304.

[7]Anan, H.S., 2002. Stratigraphy and paleobiogeography of some Frondicullariinae and Palmulinae benthic foraminiferal genera in the Paleocene of Egypt (Misr). Neues Jahrbuch fur Geologie und Palaontologie Monatshefte. 10, 629-640.

[8] Anan, H.S., 2021. *Lenticuzonaria*: A new Tethyan Lagenid benthic foraminiferal genus. Earth Sciences Pakistan (ESP). 5(1), 33-36.

[9] Lea, I., 1833. Contributions to geology. Carey, Lea and Blanchard: Philadelphia. pp. 227.

[10] Anan, H.S., 2020. *Leroyia:* a new Tethyan Lagenid benthic foraminiferal genus. Earth Sciences Pakistan (ESP). 4(2), 53-57.

[11] Batsch, A.I.G.C., 1791. Sechs Kupfertafeln mit Conchylien des Seesandes, gezeichnet und gestochen von A. J. G. K. Batsch, Jena (German) [Six copper plates with sea sand conchylia, drawn and engraved by A. J. G. K. Batsch, Jena]. Iena: Academische Buchhandlung. Available from: https://www.digitale-sammlungen.de/en/details/bsb10231112

[12] Cushman, J.A., 1938. Additional new species of American Cretaceous foraminifera. Contribution from the Cushman Laboratory Foraminiferal Research Sharon. 14, 31-50.

[13] Anan, H.S., 2022. On the variability of benthic foraminiferal species of the genus *Ramulina* in the Tethys. Journal of Foraminiferal Research. 52(3), 1-7.

[14] Nakkady, S.E., 1955. The stratigraphic implication of the accelerated tempo of evolution in the Mesozoic-Cenozoic transition of Egypt. Journal of Paleontology. 29(4), 702-706.

[15] Plummer, H.J., 1927. Foraminifera of the Midway Formation in Texas. Bulletin University of Texas. 2644, 3-206.

[16] Cushman, J.A., Jarvis, P.W., 1929. New foraminifera from Trinidad. Contributions from the Cushman Laboratory for Foraminiferal Research. 5, 6-17.

[17] Hantken, M., 1875. Die Fauna der *Clavulina szaboi* Schichten, I. Theil: Foraminiferen. Mitt. Jb. k. Ungaren (German) [The fauna of the *Clavulina szaboi* strata, Part I: Foraminifera. Mitt. Jb. k. Hungarian]. Geological Anstalt. 4, 1-93.

[18] Silvestri, A., 1923. Microfauna pliocenica rizopodi reticolari di Capocolle presso Forli (Italian) [Pliocene microfauna reticular Rhizopods of Capocolle near Forli]. Atti della Pontificia Accademia della Scienze Nuovi Lincei, Roma (1922-1923). 76, 70-77.

[19] Anan, H.S. (editor), 2007. Paleontological and biostratigraphical remarks on some diagnostic Tethyan benthic foraminifera. 2nd International Conference on the Geology of the Tethys; Cairo University, Cairo. p. 303-308.

[20] Nuttall, W.L.F., 1930. Eocene foraminifera from Mexico. Journal of Paleontology. 4, 271-293.

[21] Todd, R., Kniker, H.T., 1952. An Eocene foraminiferal fauna from the Agua Fresca Shale of Magallanes Province, southernmost Chile. Cushman Foundation for Foraminiferal Research: Ithaca. pp. 1-28.

[22] Anan, H.S., 1994. Benthic foraminifera around Middle/Upper Eocene boundary in Egypt. Middle East Research Center, Ain Shams University, Earth Science Series. 8, 210-233.

[23] Brady, H.B., 1879. Notes on some of the Reticularian Rhizopoda of the "Challenger" Expedition: Part 2. Additions to the knowledge of porcelaneous and hyaline types. Quaternary Journal of Microscopical Science, New Series. 19, 261-299.

[24] Anan, H.S., Sharabi, S.A., 1988. Benthonic foraminifera from Upper Cretaceous-Lower Tertiary rocks of northwest Kharga Oasis, Egypt. Middle East Research Center, Ain Shams University, Earth Science Series. 2, 191-218.

[25] Nakkady, S.E., 1950. A new foraminiferal fauna from the Esna Shale and Upper Cretaceous chalk of Egypt. Journal of Paleontology. 24(6), 675-692.

[26] Anan, H.S., 2019. On the variability of benthic foraminiferal species of the genus Pleurostomella in the Tethys. Journal of Microbiology & Experimentations.

7(3), 173-181.

[27] Mohan, K., Gupta, A.K., Bhaumik, A.K., 2011. Distribution of deep-sea benthic foraminifera in the Neogene of Blake Ridge, NW Atlantic Ocean. Journal of Micropalaeontology. 30(1), 33-74.

[28] Alegret, L., Thomas, E., 2013. Benthic foraminifera across the Cretaceous/Paleogene boundary in the Southern Ocean (ODP Site 690): Diversity, food and carbonate saturation. Marine Micropaleontology. 105, 40-51.

[29] Sztrákos, K., 2000. Eocene foraminifers in the Adour Basin (Aquitaine, France): biostratigraphy and taxonomy. Revue de Micropaléontologie. 43(1-2), 71-172.

[30] Proto Decima, F., de Biase, R., 1975. Foraminiferi bentonici del Paleocene, dell' Eocene inferiore e medio. Foraminiferi bentonici del Paleocene ed Eocene della sezione di Possagno (Italian) [Benthic foraminifera from the Paleocene, lower and middle Eocene. Paleocene and Eocene benthic foraminifera of the Possagno section]. Schweizerische Paläontologische Abhandlungen. 97, 87-98.

[31] Hulsbos, R.E., 1986. Eocene benthic foraminifers from the upper continental rise off New Jersey, Deep Sea Drilling Project Site 605. Initial Reports of the Deep Sea Drilling Project, Washington (U.S. Govt. Printing Office). 93, 525-538.

[32]Ozsvárt, P., 2007. Middle and Late Eocene benthic foraminiferal fauna from the Hungarian Paleogene Basin: Systematics and paleoecology. Hantken Press: Budapest. pp. 129.

[33] Anan, H.S., 1995. Late Eocene Biostratigraphy of Jabals Malaqet and Mundassa of Al Ain region, United Arab Emirates. Revue de Micropaleontologie. 38(1), 3-14.

[34] Haq, B.U., Aubry, M.P., 1978. Early Cenozoic calcareous nannoplankton biostratigraphy and palaeobiogeography of North Africa and the Middle East and Trans-Tethyan correlations. The Geology of Libya. Academic Press: London. pp. 271-304.

[35] Mintz, L.W., 1981. Historical geology, the science of a dynamic earth, 3rd edition, Merrill Publication Company: Princeton. pp. 611.

[36] Rosenbaum, G., Lister, G.S., Duboz, C., 2002. Relative motions of Africa, Iberia and Europe during Alpine orogeny. Tectonophysics. 359(1-2), 117-129.

[37] Aubert, J., Berggren, W.A., 1976. Paleocene benthonic foraminiferal biostratigraphy and paleoecology of Tunisia. Bulletin du Centre de Recherches Pau- SNPA. 10(2), 379-469.

[38] Adams, C.G., Gentry, A.W., Whybrow, P.J., 1983. Dating the terminal Tethys event. Utrecht Micropaleontological Bulletin. 30, 273-298.

[39] Anan, H.S., 2017. Paleontology, paleogeography and paleoenvironment of the Paleocene benthic foraminiferal species of Plummer in the Tethys: A review. Journal of Tethys. 5(3), 272-296.

[40] Abed, A.M., 2013. The eastern Mediterranean phosphorite giants: An interplay between tectonics and upwelling. GeoArabia. 18(2), 67-94.

[41] Anan, H.S., 2011. Paleontology, paleoenvironments, palaeogeography and stratigraphic value of the Maastrichtian-Paleogene and recent foraminiferal species of Anan in the Middle East. Egyptian Journal of Paleontology. 11, 49-78.

[42] Issawi, B., 1999. The phanerozoic geology of Egypt: A geodynamic approach. Egyptian Geological Survey: Cairo. pp. 1-462.

[43] Nakkady, S.E., 1950. A new foraminiferal fauna from the Esna Shale and Upper Cretaceous chalk of Egypt. Journal of Paleontology. 24(6), 675-692.

[44] LeRoy, L.W., 1953. Biostratigraphy of Maqfi section, Egypt. Geological Society of American Memoir. 54, 1-73.

[45] Berggren, W.A., Aubert, J., 1975. Paleocene benthonic foraminiferal biostratigraphy, paleobiogeography and paleoecology of Atlantic-Tethyan regions: Midway-type fauna. Palaeogeography, Palaeoclimatology, Palaeoecology. 18(2), 73-192.

[46] Hayward, B.W., Kawagata, S., Sabaa, A., et al., 2012. The last global extinction (Mid-Pleistocene) of deep-sea benthic foraminifera (Chrysalogoniidae, Ellipsoidinidae, Glandulonodosariidae, Plectofrondiculariidae, Pleurostomellidae, Stilostomellidae), their Late Cretaceous–Cenozoic history and taxonomy. Cushman Foundation for Foraminiferal Research. 43, 1-408.

Earth and Planetary Science
https://ojs.nassg.org/index.php/eps

RESEARCH ARTICLE

# On the Millennial-scale Variability in Climate of the Northern Hemisphere

**Maxim G. Ogurtsov**[1,2]

1. Ioffe Physico-Technical Institute, St. Petersburg, 194021, Russia
2. Central Astronomical Observatory at Pulkovo, 196140, Russia

ARTICLE INFO

*Article history*
Received: 19 March 2023
Revised: 10 April 2023
Accepted: 23 April 2023
Published Online: 26 April 2023

*Keywords*:
Climatic change
Paleoclimatology
Dendrochronology

ABSTRACT

The question of the existence of millennial-scale climate variability and its possible impacts is important for interpreting long-term climate changes and predicting its future. In the present work a statistical analysis of the seven most recent annual reconstructions of the Northern Hemisphere temperature, covering time intervals with a length from 1260 to 2016 years, was carried out. The analysis included data of different types - both tree-ring paleo reconstructions and multi-proxies. The study was carried out using both methods of Fourier and wavelet analysis. It is shown that the yearly resolved modern temperature reconstructions indicate that in the temperature of the Northern Hemisphere of the Earth in the last 1-2 millennia there is a strong variation with a period close to 900 years. The 1400-year variation appears only in a few temperature reconstructions. Thus, the presence of a weaker 1400-year variation in the temperature of the Northern Hemisphere is not excluded but this is uncertain. The obtained difference in the spectral compositions of different data sets can be associated with: (a) the difference in the geographical location of the individual temperature indicators used, (b) the difference in the methods of standardization and generalization of the used individual proxies, (c) the difference in the seasonality of the temperature reconstructions. Although the evidence obtained for the existence of the millennial-scale variability in the climate of the Northern Hemisphere is sufficiently convincing, a concluding answer to the question of its character requires the analysis of more reconstructions that: (a) are at least several millennia-long, (b) have high time resolution, (c) use a network of individual indicators covering the largest part of the Northern Hemisphere.

## 1. Introduction

Many studies have claimed the presence of a ca 1470-year climate cycle in various types of Pleistocene geologic and ice deposit records from the North Atlantic region [1-3]. The period of this variation was reported as 1470 ± 500 years [1]. It was determined only approximately because the time resolution of the majority of the analyzed records was low, usually 50-180 years [1,4]. A similar cycle was identified in two annually resolved temperature proxies for the Northern Hemisphere [5], but the length of these

*Corresponding Author:
Maxim G. Ogurtsov,
Ioffe Physico-Technical Institute, St. Petersburg, 194021, Russia; Central Astronomical Observatory at Pulkovo, 196140, Russia;
*Email: ogurtsov.maxim@mail.ru*

DOI: http://dx.doi.org/10.36956/eps.v2i1.828

series—about two millennia—is insufficient to accurately determine the oscillation period. The question of the existence of a 1470-year cycle and its possible impacts is important for interpreting centennial and millennium time scales of climate variability, in particular, North Atlantic ice drift and surface hydrography, as well as for understanding atmospheric-ocean coupling and predicting future climate changes. For example, the question of whether the Little Ice Age was an isolated climatic event or was it the most recent cold phase in the series of millennial-scale fluctuations is closely related to the question of the existence of the 1470-year periodicity [1]. Attempts have been made to explain the nature of this cycle:

(a) By the influence of Dansgaard-Oeschger events [1]. Bond et al. [1] concluded that the 1470 year cycle is the result of a chain of climatic episodes in each of which, cool, ice-bearing waters from north of Iceland were advected south to the latitude of Britain. They considered the surface North Atlantic as a hydrographic system that shifts persistently in Dansgaard/Oeschger-like oscillation.

(b) By the influence of solar cycles [2,3]. For example, Brown et al. developed a non-linear two-state model based on the superposition of the solar 210-year and 87-year cycles affected by white noise. The model demonstrates transitions between climatic states when a certain threshold is exceeded with a spacing of 1470 years.

(c) By an astronomical mechanism that consists of fluctuations in the Earth-Sun-Moon distance [6]. In this approach the 1470-year cycle is the result of an interaction between the lunar-linked 209-year cycle and the 133-year cycle of change in Earth-Sun and Earth-Moon distances.

(d) By stochastic resonance within the climate system of North Atlantic [7]. These authors hypothesized that weak periodic forcing combined with some noise from ice sheet-related events could cause the observed 1470-year variation.

However, the actual physical mechanism of this climate change is still unknown. Moreover, some authors have disputed the existence of ca 1470-year quasi-periodicity [4,8,9]. For example, Obrochta et al. [4] concluded that the original 1500 cycles may actually be a mixture of the 1000 and 2000 cycles. Since the question of millennial climate variations is important for understanding the mechanisms of the climate system, in this work the study was continued using new data. Seven temperature reconstructions in the northern hemisphere were analyzed, including a series of Loehle [10] and Moberg et al. [11] used by Loehle and Singer [5].

## 2. Data

One of the advantages of dendroclimatology is that it allows you to reconstruct climatic parameters with a resolution of 1 year. On the other hand, standardization of tree ring sizes, which takes into account the natural decrease in their size and makes it possible to remove purely biological trends from tree ring indices, can suppress any long-term variability in the tree-ring series and make it difficult to study long-term climate changes. However, the recent improvement of dendrochronological methodologies makes it possible to preserve long-term changes in tree rings caused by climate. Thus, modern temperature dendroreconstructions retain fluctuations with a period of up to 1000 years or more. This makes them more or less suitable for studying millennium-scale variability, as has been done, for example, by Loehle and Singer [5]. In the present work paleoclimatic reconstructions of Moberg et al. [11]; Loehle [10]; Christiansen and Ljungqvist [12]; Schneider et al. [13]; Wilson et al. [14]; Guillet et al. [15]; Büntgen et al. [16] were used. For the N-TREND2015 reconstruction of Wilson et al. [14] an average between the data for North America and Eurasia was used. All data sets are described in Table 1 and are shown in Figure 1.

**Table 1**. Millennial-length reconstructions of the Northern Hemisphere temperature used in analysis.

| Source | Time span | Seasonality | Geographic area | Data type |
|---|---|---|---|---|
| Moberg et al. (2005) [11] | 1-1979 | annual | Northern Hemisphere | Tree-ring, $\delta^{18}O$, pollen, Mg/Ca, diatoms, stalagmite, borehole |
| Loehle (2007) [10] | 16-1980 | annual | Northern Hemisphere | $\delta^{18}O$, pollen, diatoms, Mg/Ca, stalagmite, documentary |
| Christiansen and Ljungqvist (2012) [12] | 0-1973 | annual | Extratropical part of the Hemisphere ($\Phi$>$30^0$ N) | Tree-ring, $\delta^{18}O$, $\delta^{13}C$, sea and lake sediments, $\delta$Ar/N, pollen, sta-lagmite, documentary |
| Schneider et al. (2015) [13] | 600-2002 | June-August | Extratropical part of the Hemisphere ($\Phi$>$30^0$ N) | Tree-ring |
| Wilson et al. (2016) [14] | 750-2010 | May-August | Northern Hemisphere | Tree-ring |
| Guillet et al. (2017) [15] | 500-2000 | June-August | Northern Hemisphere | Tree-ring, $\delta^{18}O$ |
| Buntgen et al. (2021) [16] | 1-2016 | June-August | Northern Hemisphere | Tree-ring |

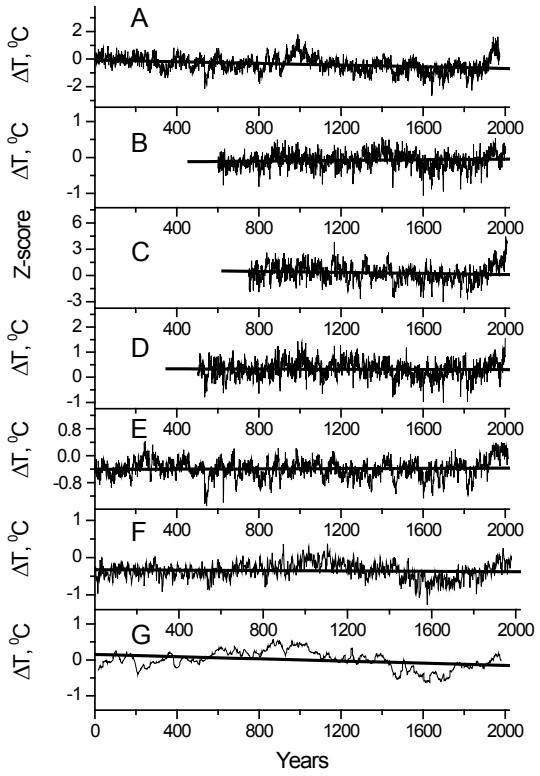


**Figure 1**. Reconstructions of the Northern Hemisphere temperature over the last 1.5-2.0 millennia: A—the multiproxy of Christiansen and Ljungqvist [12]; B—the tree-ring proxy of Schneider et al. [13]; C—the tree-ring proxy of Wilson et al. [14] (Z-score relative to the 1750-1950 period); D—the multiproxy of Guillet et al. [15]; E—the tree-ring proxy of Büntgen et al. [16]; F—the multiproxy of Moberg et al. [11]; G—the non tree-ring proxy of Loehle [10]. The figure also shows linear trends.

## 3. Methods and Results

Spectral properties of the seven reconstructions were studied by means of wavelet and Fourier analysis. The main disadvantage of Fourier methods, which have been used for a long time in the analysis of time series, is the assumption that the process is stationary. In the case of a non-stationary dataset (the class of datasets to which the main part of the climate series belongs), the Fourier transform allows only the average power at a given frequency to be estimated, and it is impossible to trace the change in the spectral composition over time. This disadvantage is absent when using the wavelet transform. The wavelet transform has a fundamental difference from the Fourier transform – here the analyzed signal is decomposed not into infinite sinusoidal harmonics, but into a series of wavelets – m orthogonal waves of the solyton type. These waves are called wavelets and they are well localized in both frequency and time [17], while Fourier harmonics are only localized in frequency. Due to this property, the wavelet transform is suitable for the analysis of non-stationary time series, including non-periodic inhomogeneities, deterministic chaos, and local periodic structures. Wavelet analysis has long been successfully used in the study of climate series [18]. Linear trends were preliminarily subtracted from all the series. The Fourier spectra of the analyzed data sets have strong peaks in the range of 750-1960 years, but the resolution in their low-frequency part is low. Wavelet analysis (basis of Morlet) can provide better resolution. Global wavelet spectra are shown in Figure 2. All the spectra are normalized to a 0.95 confidence level calculated for red noises with the corresponding AR(1) coefficient.

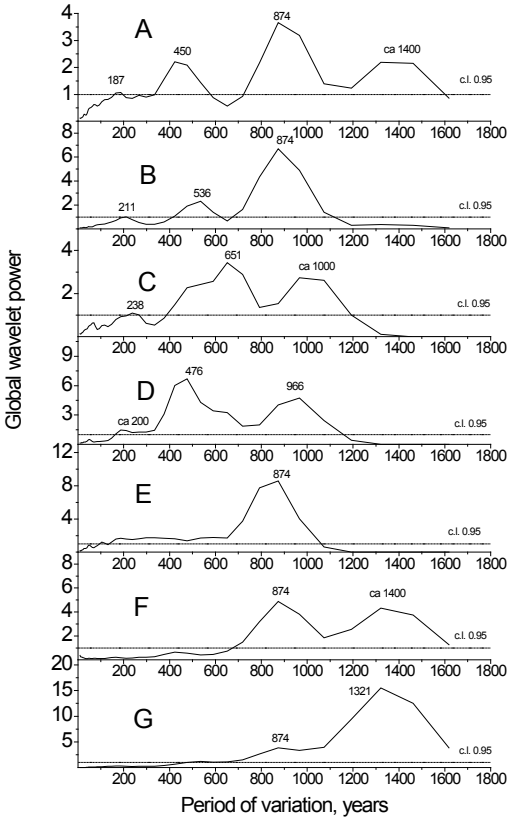


**Figure 2**. Global wavelet spectra of: A—the multiproxy of Christiansen and Ljungqvist [12]; B—the tree-ring proxy of Schneider et al. [13]; C—the tree-ring proxy of Wilson et al. [14]; D—the multiproxy of Guillet et al. [15]; E—the tree-ring proxy of Büntgen et al. [16]; F—the multiproxy of Moberg et al. [11]; G—the non tree-ring proxy of Loehle [10].

Figure 2 shows that ca 900-year (period 874-966 years) cycle is clearly expressed in all seven series, while ca 1400-year variation is manifested in three records. Here, however, a problem arises—is it possible to distinguish a 900-year variation from a 1400-year variation on such

a short time interval? To answer this question, two series of 2000 years were generated, each consisting of the sum of a sine wave with a period of 900 or 1400 years and red noise (AR(1)=0.6). The power of the red noise was such that the signal-to-noise ratio ($\sigma^2(signal)/\sigma^2\ (noise)$) was 0.1. Then the global wavelet spectra of these noisy time series were calculated. They are shown in Figure 3.

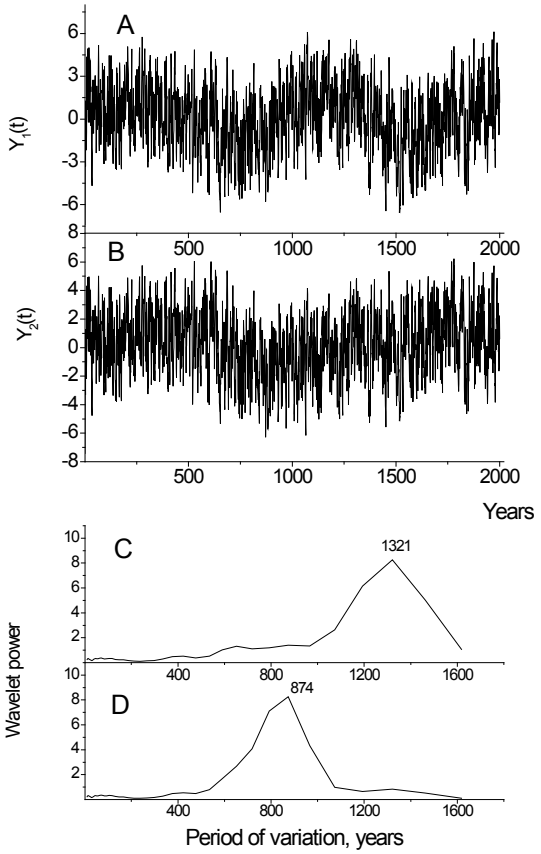


**Figure 3**. A—$Y_1(t)$ – a sine wave with a period of 900 years plus red noise; B—$Y_2(t)$—a sine wave with a period of 1400 years plus red noise; C—global wavelet spectrum of $Y_1(t)$; D—global wavelet spectrum of $Y_2(t)$.

Figure 3 shows that despite the shortness of the time series, it is possible to distinguish the 900-year oscillation from the 1400-year oscillation.

## 4. Discussion and Conclusions

It is shown the yearly resolved modern temperature reconstructions indicate that there is a strong cyclicity in the temperature of the Northern Hemisphere of the Earth with a period close to 900 years. This testifies that the 1000-year periodicity reported in the climate of the North Atlantic [4] has a global character. The 1400-year variation is less pronounced and appears only in a few temperature reconstructions. The difference in the spectral compositions of different data sets can be associated with:

(a) The difference in geographical location of the individual temperature indicators used. In fact, it is known that interdecadal and century-scale temperature variability has a strong spatial distribution with a marked change in amplitude and phase depending on geographic location [19]. In this regard, it can be noted that the subpolar sector of North Atlantic, in which the 1470-year variation has been established most reliably [1,2], is poorly covered by individual proxies in the reconstructions [13,14].

(b) The difference in the methods of standardization and generalization of the used individual proxies. In this regard, it can be noted that the 1470-year cycle is most pronounced in the series of Loehle (2007) [10], which did not use any tree-ring data and, as a result, the long-term variations of which were completely free from any influence of standardization procedures.

(c) The difference in seasonality of the temperature reconstruction. This difference may also play a role, since different seasons may show different temperature fluctuations. For example, in Southern Scandinavia bi-decadal variation is present in a warm season, while decadal variation is observed in winter [20].

For a concluding answer to the question of the millennial-scale variability in the climate of the Northern Hemisphere, it is necessary to obtain new paleoreconstructions that: (a) are at least several millennia long, (b) have high time resolution, (c) use a network of individual indicators covering as much of the Northern Hemisphere as possible. The use of non tree-ring reconstructions, whose low-frequency variations are not distorted by standardization procedures, appears to be preferable.

## Conflict of Interest

There is no conflict of interest.

## References

[1] Bond, G.C., Showers, W., Cheseby, M., et al., 1997. A pervasive millennial-scale cycle in North Atlantic Holocene and glacial climates. Science. 278(5341), 1257-1266.

[2] Bond, G.C., Kromer, B., Beer, J., et al., 2001. Persistent solar influence on North Atlantic climate during the Holocene. Science. 294(5549), 2130-2136.

[3] Braun, H., Cyristl, M., Ramhstorf, S., et al., 2005. Possible solar origin of the 1,470-year glacial climate cycle demonstrated in a coupled model. Nature. 438(7065), 208-211.

[4] Obrochta, S.P., Miyahara, H., Yokoyama, Y., et al., 2012. A re-examination of evidence for the North

Atlantic "1500-year cycle" at Site 609. Quaternary Science Reviews. 55, 23-33.

[5] Loehle, C., Singer, F., 2010. Holocene temperature records show millennial-scale periodicity. Canadian Journal of Earth Sciences. 47(10), 1327-1336.

[6] Kelsey, A., 2022. Abrupt climate change and millennial-scale cycles: An astronomical mechanism. Climate of the Past Discussions. (preprint), 1-19. DOI: https://doi.org/10.5194/cp-2022-49

[7] Alley, R.B., Anandakrishnan, S., Jung, P., 2001. Stochastic resonance in the North Atlantic. Paleoceanography. 16, 190-198.

[8] Ditlevsen, P.D., Andersen, K.K., Svensson, A., 2007. The DO-climate events are probably noise induced: Statistical investigation of the claimed 1470 years cycle. Climate of the Past. 3(1), 129-134.

[9] Clemens, S.C., 2005. Millennial-band climate spectrum resolved and linked to centennial-scale solar cycles. Quaternary Science Reviews. 24(5-6), 521-531.

[10] Loehle, C., 2007. A 2000-year global temperature reconstruction on non-tree ring proxies. Energy and Environment. 18(7), 1049-1058.

[11] Moberg, A., Sonechkin, D.M., Holmgren, K., et al., 2005. Highly variable Northern Hemisphere temperatures reconstructed from low- and high-resolution proxy data. Nature. 433(7026), 613-617.

[12] Christiansen, B., Ljungqvist, F.C., 2012. The extra-tropical Northern Hemisphere temperature in the last two millennia: Reconstructions of low-frequency variability. Climate of the Past. 8(2), 765-786.

[13] Schneider, L., Smerdon, J.E., Büntgen, U., et al., 2015. Revising midlatitude summer temperatures back to A.D. 600 based on a wood density network. Geophysical Research Letters. 42(11), 4556-4562.

[14] Wilson, R., Anchukaitis, K., Briffa, K., et al., 2016. Last millennium northern hemisphere summer temperatures from tree rings: Part I: The long term context. Quaternary Science Reviews. 134, 1-18.

[15] Guillet, S., Corona, C., Stoffel, M., et al., 2017. Climate response to the Samalas volcanic eruption in 1257 revealed by proxy records. Nature Geoscience. 10(2), 123-128.

[16] Büntgen, U., Allen, K., Anchukaitis, K.J., et al., 2021. The influence of decision-making in tree ring-based climate reconstructions. Nature Communications. 12(1), 3411.

[17] Torrence, C., Compo, G.P., 1998. A practical guide to wavelet analysis. Bulletin of the American Meteorological Society. 79(1), 61-78.

[18] Lau, K.M., Weng, H., 1995. Climate signal detection using wavelet transform: How to make a time series sing. Bulletin of the American Meteorological Society. 76(12), 2391-2402.

[19] Mann, M., Park, J., Bradley, R., 1995. Global interdecadal and century-scale climate oscillations during the past five centuries. Nature. 378(6554), 266-270.

[20] Ogurtsov, M., 2021. Decadal and di-decadal periodicities in temperature of Southern Scandinavia: Manifestations of natural variability or climatic response to solar cycles? Atmosphere. 12(6), 676.

NASS
NAN YANG ACADEMY OF SCIENCES

**Earth and Planetary Science**
https://ojs.nassg.org/index.php/eps

RESEARCH ARTICLE

# The Problem of $CO_2$ Reabsorption in Emission Spectra

**Svatopluk Civiš[1*] Adam Pastorek[2] Sergei N. Yurchenko[3]**

1. J. Heyrovsky Institute of Physical Chemistry, Czech Academy of Sciences, Dolejškova, Prague, 18223, Czech Republic
2. Department of Chemistry and Biochemistry, Old Dominion University, Norfolk, Virginia, 23529, United States of America
3. Faculty of Mathematical and Physical Sciences, University College London, Gower Street, London, WC1E6BT, United Kingdom

ARTICLE INFO

*Article history*
Received: 4 April 2023
Revised: 26 April 2023
Accepted: 27 April 2023
Published Online: 17 May 2023

*Keywords*:
Reabsorption
Carbon dioxide
FTIR spectroscopy
Vacuum vs air measurement

ABSTRACT

The authors present a detailed explanation for selective reabsorption by the $CO_2$ $\nu_3$-band when passing its optical emission through an atmospheric-pressure air column (60 cm long, 410 ppm $CO_2$) connecting a microwave-discharge cell and the entrance window of a high-resolution Fourier Transform spectrometer. The $CO_2$ band shapes are explained with a two-temperature model of emission and foreground absorption. Selective $CO_2$ atmospheric reabsorption is a common effect in optical emission measurements. It primarily affects the fundamental infrared bands, which comprise the main part of the missing laboratory emission and must be taken into account in (exo)planetary atmospheric models.

## 1. Introduction

Reabsorption (or even self-absorption, when mentioning the reabsorption of radiation by the emitter) is practically omnipresent in emission light sources, where reabsorption of a portion of the emitted light causes a light flux deficit. This deficit disrupts the linear dependence of signal and on analyte concentration that is stated for any spectroscopic or spectrochemical measurement. For example, self-absorption by the emitter plays a major role in laser-induced breakdown spectroscopy (LIBS). In LIBS, self-absorption is a huge drawback because the nonlinear signal dependence can lead to false information on the quantity of an analysed sample. Many studies have been written on the problem of reabsorption in LIBS, e.g. Rezaei et al. [1] being among the most recent. Generally,

*Corresponding Author:
Svatopluk Civiš,
J. Heyrovsky Institute of Physical Chemistry, Czech Academy of Sciences, Dolejškova, Prague, 18223, Czech Republic;
*Email: svatopluk.civis@jh-inst.cas.cz*

DOI: http://dx.doi.org/10.36956/eps.v2i1.836

self-absorption depends on the density of the analyte, the size of the emitter and the population of the lower energy level of a specific transition.

Raman emission spectroscopy is another optical emission method and also struggles with signal nonlinearity caused by reabsorption in quantitative measurements. According to Wu et al. [2], it is possible to control and restrict reabsorption by proper experimental methods, like the use of external and internal standards. Reabsorption was also studied in near-infrared (NIR) Fourier-transform (FT) Raman measurements of tetrahydrofuran by Petty [3], and by Agarwal et al. [4] in cellulosic materials.

Recently we studied the intensity ratio of the $D_1$ and $D_2$ sodium-doublet emission lines, which varies in spectra of astronomical sources and laboratory plasma [5]. This work probes the behaviour of this ratio under controlled laboratory conditions and shows the relative intensities of the Na doublet are determined by self-absorption dependent on the nitrogen buffer-gas pressure and discharge power. The emission-intensity ratio and individual line shapes were explained by a two-temperature model of sodium emission and foreground absorption.

Reabsorption is also extensively studied in X-ray absorption spectroscopy. Trevorah et al. [6] presented a software approach accounting for potential self-absorption of secondary inelastically scattered fluorescence photons. Furthermore, publications from Nassar et al. [7] and Hargreaves et al. [8] have to be mentioned because of reabsorption present in experimental spectra.

$CO_2$ lasers are an emitting source that also suffers from self-absorption. The output power deficit of $CO_2$ lasers due to self-absorption was demonstrated in 1981 by Hishii et al. [9]. This effect was also noticed for low pressure of $CO_2$ active gas by Kaye et al. [10] in 1983.

Here, we find that the reabsorption of $CO_2$ emission spectra must always be taken into account during optical measurements. Especially if carbon dioxide is present in the laboratory system outside the emission region, because of its exceptional absorbing abilities.

## 2. Experimental Setup

The emission beam was created in a microwave discharge realized in a quartz tube of 12 mm external diameter and 150 mm total length. The front window of the tube was made from $CaF_2$ and the tube was constantly evacuated by a rotary vacuum pump to ensure a flowing regime of gases. The discharge tube was inserted into a microwave cavity connected to a magnetron microwave source (2.45 GHz). The experimental scheme is depicted in Figure 1.

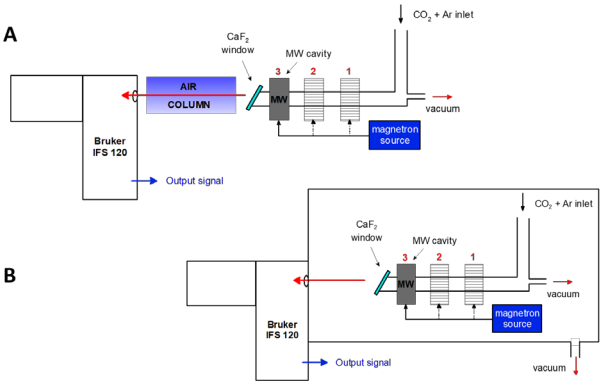


**Figure 1.** A—Scheme of the microwave discharge in the air; B—Scheme of the microwave discharge in vacuum.

The discharge was made in $CO_2$ mixed with an argon buffer gas. The partial gas pressures were 0.1 Torr of $CO_2$ and 1 Torr of Ar. The output power of the magnetron was 30 W. The spectra were recorded with a Bruker 120 HR FTIR spectrometer. The spectrometer was equipped with a $CaF_2$ beam splitter and $CaF_2$ entry window. The aperture was set to 4 mm and a liquid-nitrogen-cooled InSb detector was used. The recorded spectral range was 1800 to 3500 $cm^{-1}$, limited by an interference optical filter. The unapodized spectral resolution was 0.02 $cm^{-1}$ and 20 scans were accumulated to obtain a reasonable signal-to-noise ratio. The experimental arrangement used in this work is similar to our paper on sodium self-absorption [5].

As depicted in Figure 1, the experimental arrangement was performed in two setups. Panel A of Figure 1 shows the arrangement of discharge performed in air, where the emission optical beam passes through 60 cm of atmospheric air before entering the entry aperture of the spectrometer, undergoing reabsorption along its path. The second setup (panel B of Figure 1) shows the implementation of a vacuum chamber that housed the whole microwave cavity tube system. In this system, no external air column was present and therefore no reabsorption occurred. Also, it must be noted that significant effort was made to ensure there was no cold gas in between the microwave cavity and the $CaF_2$ window of the emission system tube. This fact is depicted in Figure 1 as shaded rectangles presenting MW cavity position. By varying the position of the cavity (numbers 1 to 3), an optimal position of the cavity was achieved.

## 3. Results and Discussion

Firstly, a pure absorption arrangement measurement of $CO_2$ was performed. This measurement was conducted in order to obtain a comparative spectrum of a fundamental band of $CO_2$. This measurement was performed with pure $CO_2$ (Linde gas > 99.9%) of a pressure of 0.5 Torr, placed

in a cell of 30 cm length at a temperature of 298 K. Other parameters were the same as described in experimental setup section. An absorbance spectrum depicted in Figure 2 was obtained.

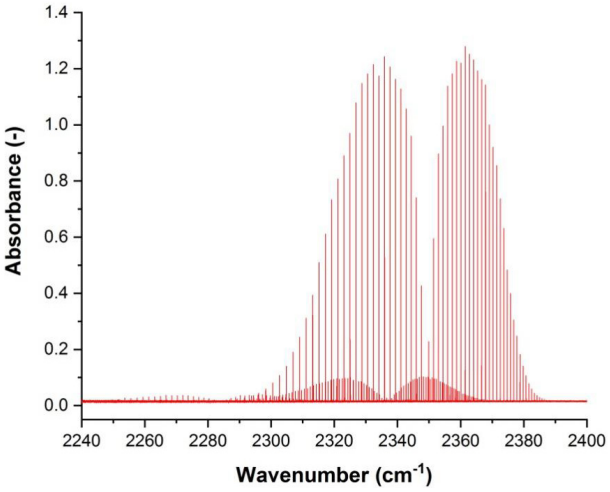


**Figure 2.** $CO_2$ spectrum measured in absorption arrangement.

The spectrum of fundamental $CO_2$ band ($\nu_3$) resembles itself in a well-defined two-branch shape. This is a shape of $\nu_3$ band common for absorption measurements since $CO_2$ only absorbs a part of referential light and the population of energy levels is hence typical. Since a standard $CO_2$ gas was used, both the most common isotopes of $^{12}CO_2$ and $^{13}CO_2$ are present in the spectrum.

In an ideal case, the emission spectrum is a combination of fundamental $\nu_3$ band together with additional several rovibrational excited states of $CO_2$ (Figure 3).

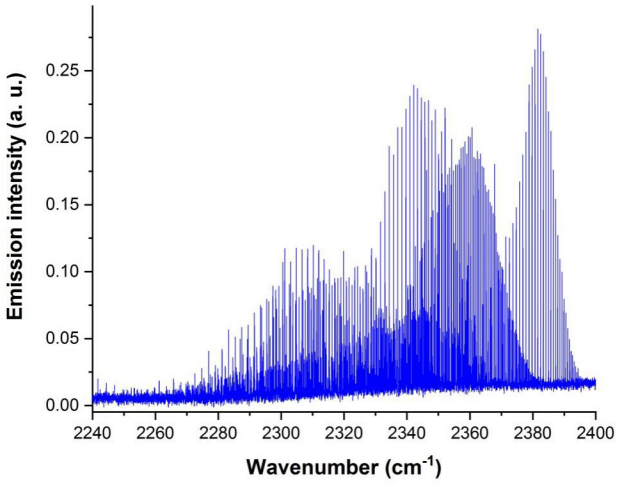


**Figure 3.** $CO_2$ fundamental band in emission arrangement (in vacuum).

Spectrum depicted in Figure 3 was obtained by emission measurement of $CO_2$ mixed with Ar of total pressure of 1.1 Torr (0.1 Torr of $CO_2$ and 1 Torr of Ar). The whole apparatus was located in an evacuated vacuum chamber directly connected to the spectrometer. Emission light beam thus did not encounter any air during its path. Nevertheless, when the emission experiment is carried out in the standard laboratory environment and the emission light beam passes a column of atmospheric air before it enters the evacuated measuring device, the air containing $CO_2$ reabsorbs the emitted light and the resulting spectrum then looks different. The comparison of such spectrum with the previous one measured in vacuum (Figure 3) can be seen in Figure 4.

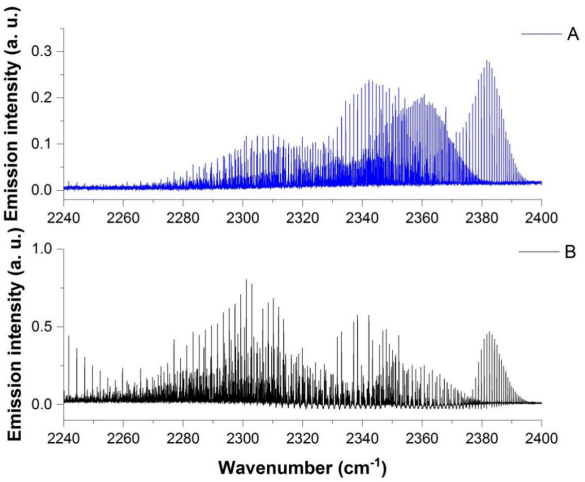


**Figure 4.** A comparison of vacuum-measured $CO_2$ emission spectrum (no reabsorption effect) (panel A) together with the reabsorbed $CO_2$ emission (60 cm long air column, atmospheric pressure, 410 ppm $CO_2$) (panel B).

The spectrum depicted in panel B of Figure 4 was obtained in emission arrangement when creating a glow discharge of $CO_2$ mixed with argon as buffer gas of total pressure of 1.1 Torr (0.1 Torr of $CO_2$ and 1 Torr of Ar). The emission light beam passed 60 cm of air at atmospheric pressure and a standard laboratory temperature of 298 K before entering the spectrometer. Weak absorption features of $CO_2$ ($\nu_3$ fundamental band) can be recognized below the horizontal background level as well as the line broadening caused by atmospheric $CO_2$ absorption. Due to atmospheric absorption a large part of the $\nu_3$ emission spectrum is eliminated.

A theoretical spectrum has been modelled in collaboration with University College London that matches our experimental emission spectrum measured in air. A comparison of such a model and experimental emission spectrum is depicted in Figure 5.

Microwave discharge emission spectrum is shown in Figure 5 together with a theoretically modelled $CO_2$ emission. For the calculated spectrum we used a two-tempera-

ture (555 K and 700 K) non-LTE model from Pastorek et al. [11] where the $2\nu_3 - \nu_3$ band was multiplied by a factor of 23 to match the experimental intensity. The theoretical model was constructed from the UCL-4000 line list [12] with the resolution = 0.01 $cm^{-1}$, Lorentzian line profile, a HWHM = 0.017 $cm^{-1}$ and the rotational temperature set to $T_R$ = 555 K, corresponding to the experimental conditions. The effect of self-absorption is not included in the model. The shape of the experimental $\nu_3$ emission band does not correspond well to the theoretical model due to elimination of the $\nu_3$ atmospheric absorption in a spectral range of 2300-2380 $cm^{-1}$ in the model. Only a few lines between 2370 and 2390 $cm^{-1}$ are strong enough to match this part of the theoretical $\nu_3$ band.

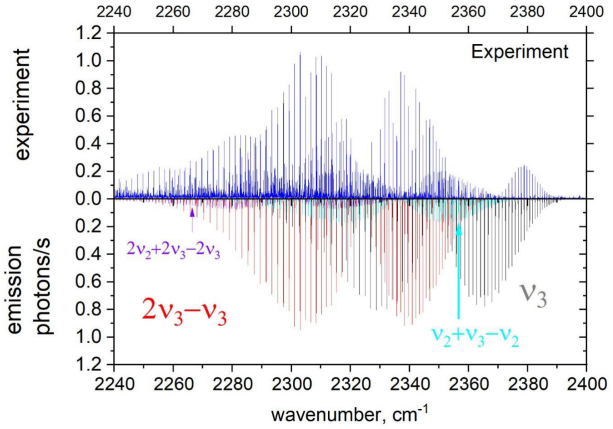


**Figure 5.** Experimental emission of the reabsorbed $CO_2$ emission (60 cm long air column) (top) and theoretical (bottom) non-LTE emission spectrum of $CO_2$.

The experimental spectrum in Figure 5 can be matched to the hot $\nu_2 + \nu_3 - \nu_2$ (01111-01101) and $2\nu_3 - \nu_3$ (00021-00011) bands of $CO_2$, as well as to the $2\nu_2 + \nu_3 - 2\nu_2$ (10012-02201) (lower display, plotted in green, blue and pink) spectrum. In the non-LTE model [13], the vibrational temperature of the hot bands $2\nu_3 - \nu_3$ and $2\nu_2 + \nu_3 - 2\nu_2$ was set to 700 K, while other bands were modelled using $T$ = 555 K. The $2\nu_3 - \nu_3$ band is an especially important feature of non-LTE $CO_2$ within the Martian atmosphere [13] where the overpopulation of the upper state is caused by solar radiation pumping at 2.7 μm. The fundamental band of $CO_2$ around 2300 $cm^{-1}$ was also detected in non-LTE emission via fluorescence of solar radiation in Venus's atmosphere by VIRTIS spectrometer [14].

The hot bands ($2\nu_2 + \nu_3 - 2\nu_2$, $2\nu_3 - \nu_3$, or $\nu_2 + \nu_3 - \nu_2$) depicted in Figure 5 are unaffected by reabsorption in the atmospheric section of the measured optical path. Only the part of the most intense atmospheric infrared fundamental band ($\nu_3$), (room temperature, relatively low $J$ rotational excitation) has a high influence on the reabsorption effect (see Figures 4 and 5).

The distribution of spectral intensity in absorption on rotational quantum number (room temperature, 0.5 Torr pressure and 30 cm optical path) and of $CO_2$ $\nu_3$-band $R$-branch emission (See Figure 4, panel B) can be seen in Figure 6. Comparison of spectra showing $CO_2$ absorption spectrum (red) and emission (blue). Most lines appearing in the absorption spectrum are missing from the laboratory emission. The absorption spectrum intensities in Figure 6 have been obtained by measurement of 0.5 Torr of pure $CO_2$ at room temperature (298 K) in a 30 cm long absorption cell (Figure 2). The unapodized spectral resolution was 0.05 $cm^{-1}$ and other parameters were the same as for the emission experiments. Figure 6 clearly demonstrates differences in the $\nu_3$ band rotation intensities of $J$ when measured in absorption and emission. Rotational lines of the $CO_2$ $\nu_3$-band with $J$ = 0 to 34 are completely in the emission spectrum missing. The higher $J$ vibrational transitions are starting to appear in the spectrum at frequencies higher than approximately 2375 $cm^{-1}$ (see Figures 5 and 6).

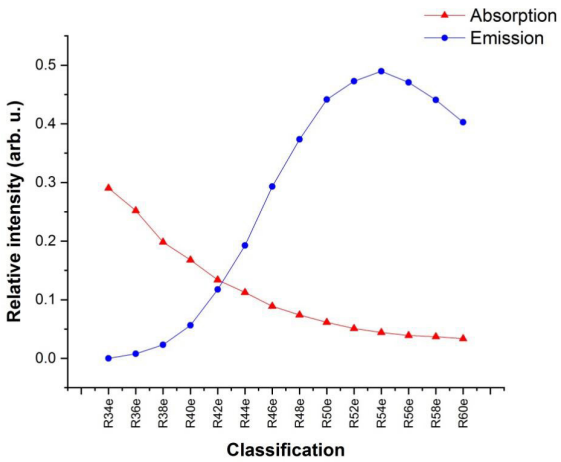


**Figure 6.** Intensity distribution of $CO_2$ $\nu_3$ lines in absorption and emission.

Around the line R42e, the emission intensity becomes almost as intense as selective reabsorption of $CO_2$ (equilibrium). For higher $J$-values, emission prevails in the spectrum (the atmospheric room temperature absorption of high-$J$ transitions is weak, on the contrary the rotational excitation in the microwave discharge is high) which allows for the intense blue tail of the $\nu_3$ band observed between 2380 and 2400 $cm^{-1}$, as depicted in Figures 5 and 6.

In order to get an exact model of our $CO_2$ discharge emission through the atmospheric air column ($I_{tot}$), one must include an absorption part of our simulation. The infrared $\nu_3$ absorption band (Figure 2) was subtracted from

the simulated non-LTE emission spectrum shown in Figure 5. For the absorption spectrum we used T = 296 K and the Lorentzian line profile of HWHM = 0.017 $cm^{-1}$. The emission spectrum was modelled using a two-temperature non-LTE model. The total spectrum of $CO_2$ was constructed as:

$$I_{tot} = I_{vacuum\ emission} - A \times I_{absorp},$$

where A was adjusted for the closest reproduction of the experimental spectrum and $I_{absorp}$ is as in our paper [11] with the fundamental 00011 and hot bands 01111-01101 affected. The underlying line list is UCL-4000. A comparison of the experimental reabsorbed $CO_2$ emission spectrum (60 cm long air column) (top) and theoretical (bottom) corrected ($I_{tot}$) spectrum of $CO_2$ is depicted in Figure 7.

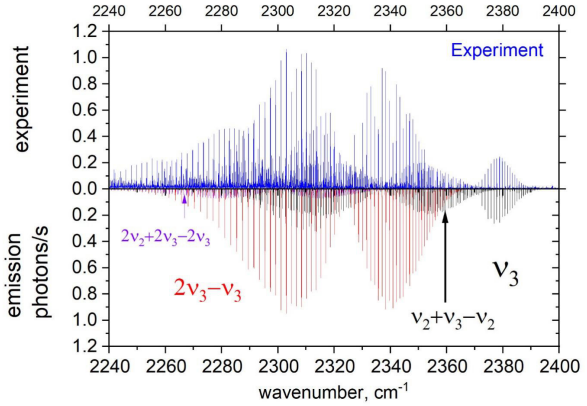


**Figure 7.** Experimental emission of the reabsorbed $CO_2$ emission (60 cm long air column) (top) and theoretical $I_{tot}$ (bottom) reabsorption model of the non-LTE emission spectrum of $CO_2$.

## 4. Conclusions

This short letter points out the reabsorption effect in $CO_2$ when its emission passes through a volume of atmosphere containing trace $CO_2$ (410 ppm). The effect of reabsorption is most prominent for the fundamental transitions of the $\nu_3$ band, especially for lower *J*-values.

The experimental results demonstrate the dominating absorption properties of the fundamental infrared carbon dioxide rovibrational bands. This must be taken into account in all cases of planetary atmospheric models that are based on measured emission data, including in models of exoplanetary atmospheres containing high $CO_2$ concentrations.

## Author Contributions

SC invented the research, conducted the experiments, edited the manuscript, and provided funding. AP conducted the experiments, wrote the original manuscript, and edited the manuscript. SNY performed theoretical calculations and modelling and provided funding.

## Funding

This work is part of a research series funded by ERDF/ESF "Centre of Advanced Applied Sciences" project no. CZ.02.1.01/0.0/0.0/16_019/0000778 and by grant no. 21-11366S of the Czech Science Foundation. Development of Ariel space telescope is supported by ESA Prodex project under PEA 4000129979. The work by SY was supported by the European Research Council (ERC) under the European Union's Horizon 2020 research and innovation programme through Advance Grant number 883830 and the STFC Project ST/R000476/1.

## Acknowledgment

This work was funded by grant no CZ.02.1.01/0.0/0.0/16_019/0000778 alias "ERDF/ESF Centre of Advanced Applied Sciences".

## Data Availability Statement

The data presented in this study are available on request from the corresponding author.

## Conflicts of Interest

Authors declare no conflicts of interest.

## References

[1] Rezaei, F., Cristoforetti, G., Tognoni, E., et al., 2020. A review of the current analytical approaches for evaluating, compensating and exploiting self-absorption in Laser Induced Breakdown Spectroscopy. Spectrochimica Acta Part B: Atomic Spectroscopy. 169, 105878.

[2] Wu, Z., Zhang, C., Stair, P.C., 2006. Influence of absorption on quantitative analysis in Raman spectroscopy. Catalysis Today. 113(1-2), 40-47.

[3] Petty, C.J., 1991. Self-absorption in near-infrared Fourier transform Raman spectrometry. Vibrational Spectroscopy. 2(4), 263-268.

[4] Agarwal, U.P., Kawai, N., 2005. "Self-Absorption" phenomenon in near-infrared fourier transform raman spectroscopy of cellulosic and lignocellulosic materials. Applied Spectroscopy. 59(3), 385-388.

[5] Civiš, S., Heays, A.N., Knížek, A., et al., 2021. High resolution emission FT spectra of sodium in a microwave discharge: Intensity variation of the D1/D2 lines in exoplanetary atmospheres. Journal of Quantitative Spectroscopy and Radiative Transfer. 270,

107689.

[6] Trevorah, R.M., Chantler, C.T., Schalken, M.J., 2019. Solving self-absorption in fluorescence. IUCrJ. 6(4), 586-602.

[7] Nassar, R., Bernath, P., 2003. Hot methane spectra for astrophysical applications. Journal of Quantitative Spectroscopy and Radiative Transfer. 82(1-4), 279-292.

[8] Hargreaves, R.J., Li, G., Bernath, P.F., 2011. Hot $NH_3$ spectra for astrophysical applications. The Astrophysical Journal. 735(2), 111.

[9] Hishii, M., Nagai, H., Nagai, A., et al., 1981. Influence of self-absorption on output power characteristics of a high-pressure cw $CO_2$ laser. Journal of Applied Physics. 52(8), 4953-4958.

[10] Kaye, A.S., Naylor, D.L., 1983. Runaway self-absorption in multikilowatt $CO_2$ lasers. Applied Physics Letters. 42(8), 641-642.

[11] Pastorek, A., Clark, V.H., Yurchenko, S.N., et al., 2022. New physical insights: Formamide discharge decomposition and the role of fragments in the formation of large biomolecules. Spectrochimica Acta Part A: Molecular and Biomolecular Spectroscopy. 278, 121322.

[12] Yurchenko, S.N., Mellor, T.M., Freedman, R.S., et al., 2020. ExoMol line lists–XXXIX. Ro-vibrational molecular line list for $CO_2$. Monthly Notices of the Royal Astronomical Society. 496(4), 5282-5291.

[13] Kutepov, A.A., Rezac, L., Feofilov, A.G., 2017. Evidence of a significant rotational non-LTE effect in the $CO_2$ 4.3 μm PFS-MEX limb spectra. Atmospheric Measurement Techniques. 10(1), 265-271.

[14] Gilli, G., López-Valverde, M.A., Drossart, P., et al., 2009. Limb observations of $CO_2$ and CO non-LTE emissions in the Venus atmosphere by VIRTIS/Venus Express. Journal of Geophysical Research: Planets. 114(E5), 1-19.

Earth and Planetary Science
https://ojs.nassg.org/index.php/eps

REVIEW

# Main Mechanisms of Celestial Bodies Negative Polarization Formation: A Review

**Dmitry Petrov**

Crimean Astrophysical Observatory (CrAO RAS), Nauchnyj, 298409, Crimea

ARTICLE INFO

*Article history*
Received: 27 March 2023
Revised: 24 April 2023
Accepted: 28 April 2023
Published Online: 17 May 2023

*Keywords*:
Light scattering
Degree of linear polarization
Polarization mechanisms

ABSTRACT

The scattered light by the vast majority of celestial bodies without atmospheres has a characteristic feature: A negative branch of linear polarization degree at little phase angles. Researchers have proposed many theoretical mechanisms to explain this feature. This review describes the main mechanisms that form a negative branch of linear polarization degree. The results of ground-based observations of the negative branch of the degree of linear polarization of various objects of the solar system are described. Scattering by single particles, shadow effect, coherent backscattering enhancement, and effects of the near field are considered. The review will be useful for all researchers studying the scattering of light by celestial bodies.

## 1. Introduction

Consider light with wavelengths lying in the optical range. Light incident on a scattering object is generally unpolarized. However, the scattered light is partially polarized, that is, there are planes in which the predominant part of the oscillations of the electrical vector of the electromagnetic wave is concentrated. Typically, the scattered light intensity is decomposed into two components. The first of them, denoted by $I_{\parallel}$, means the scattered radiation intensity polarized in the plane of scattering (the plane containing the observer, the scattering object and the light source). The second, denoted by $I_{\perp}$, means the intensity of scattered light whose polarization is in a plane, which is perpendicular to the plane of scattering. The linear polarization degree, expressing the relationship between these two quantities, is determined by the formula:

$$P = \frac{-I_{\parallel} + I_{\perp}}{I_{\parallel} + I_{\perp}}, \quad (1)$$

If $I_{\perp} > I_{\parallel}$, the linear polarization degree is positive. Otherwise, it is negative. The linear polarization degree depends on the phase angle α (the angle between the direction of the scattering object and the light source, and the scattering object—the observer).

The dependence of linear polarization degree on phase

*Corresponding Author:
Dmitry Petrov,
Crimean Astrophysical Observatory (CrAO RAS), Nauchnyj, 298409, Crimea;
*Email: dvp@craocrimea.ru*

DOI: http://dx.doi.org/10.36956/eps.v2i1.831

angle has been widely studied. At phase angles of 0-30°, laboratory measurements of vast majority of surfaces consisting of small particles, as well as polarimetric observations of most objects of the solar system visible from our planet, show a region of negative polarization, which often coincides with the brightness opposition effect. Characteristically, the size of the negative polarization region, as well as its magnitude, depends on the physical properties of the scattering objects [1].

Phase dependence of linear polarization degree negative branch can be described by the values shown in Figure 1: $P_{min}$ is the minimal value of the degree of polarization; $\alpha_{min}$ is the phase angle at which the minimum polarization is observed; $\alpha_{inv}$ is the angle of inversion at which the polarization equals to zero; $h = \left.\frac{dP}{d\alpha}\right|_{\alpha=\alpha_{inv}}$ is the polarization slope; $P_{max}$ is maximum polarization degree; $\alpha_{max}$ is the angle of maximum polarization. All these quantities depend very strongly on the parameters of the scattering object and, therefore, are applicable in the interpretation of observational data.

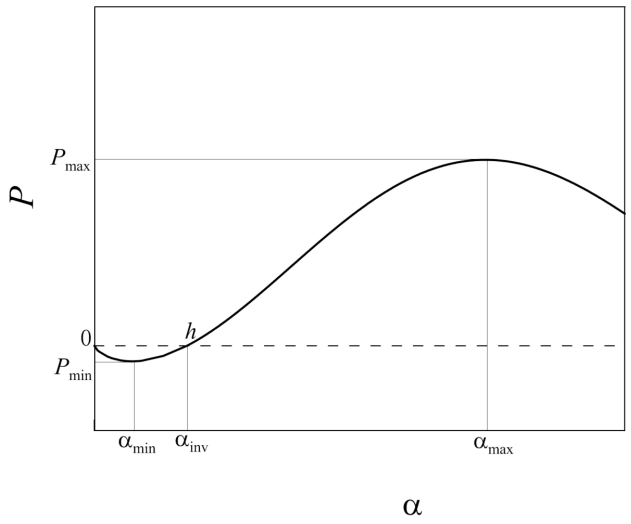


**Figure 1.** Characteristic form and main parameters of the phase dependence of the degree of linear polarization.

For non-atmospheric bodies, negative polarization branch curves usually look like a parabola ($\alpha_{inv} \approx 2\alpha_{min}$), which, for example, are observed on the Moon [2,3]. The negative polarization is also regularly observed in the moons of Jupiter and Saturn, although their curves show a marked dissymmetry in the negative polarization branch. Measurements of the linear polarization degree of various samples in the laboratory show huge variety of negative polarization [4].

The variety of phase curves is explained by a sufficiently large number of physical mechanisms that cause negative polarization. Lyot, who discovered the negative polarization of the Moon, described three main groups of physical principles underlying these physical mechanisms [2]:

- many reflections between scattering objects;
- output light refractions on transparent or translucent objects;
- light diffraction.

The first specific model describing the mechanism of the occurrence of negative polarization and corresponding to the first Lyot hypothesis is probably owing to Ohman [5]. The Ohman model uses double reflection from the troughs on a rough scattering surface, which can create negative polarization and oppositional effects. However, the experimental nature of the model was emphasized by the author, despite its progressiveness at that time.

Studies within the framework of the second Lyot group were launched by McCoyd [6]. McCoyd's research focused on a two-dimensional model that studied the behavior of light with a single external reflection and two refractions, accompanied by total internal reflection, from a uniform surface layer bounded by two interfaces.

Hopfield [7] was the first to attempt a model based on Lyot's third hypothesis using Sommerfeld's theory of diffraction. Although the model was only approximated, it gained popularity (see for example Veverka [8] and references within). The applicability of Hopfield's approach to non-atmospheric surfaces is currently unknown.

Specific mechanisms (some of which are still debatable) for the occurrence of negative polarization can be roughly divided into the following groups: Scattering by single particles, shadow effect, coherent backscattering enhancement, and the near field effects. Below we will try to describe at least some of the models underlying each of these mechanisms.

There are a number of works in which a review of certain mechanisms underlying the scattering of light has been carried out. Of particular note is the review [9], which describes achievements in the theory of light scattering by morphologically complex objects, as well as their application to the interpretation of observational data obtained in the course of photometric and polarimetric observations of celestial bodies. However, only in this review, the main mechanisms are brought together.

Note that we will focus on describing such mechanisms that can be described theoretically. Recently, a huge number of computer simulation methods have appeared that make it possible to calculate the characteristics of scattered light numerically. For example, numerical codes for modern Monte Carlo radiative transfer codes can be applied to each described negative polarization mechanism. However, there are so many variations of numerical

methods that their detailed description is far beyond the scope of this review. A recent review provides a complete description of modern Monte Carlo radiative transfer codes [10] and references within.

## 2. Negative Polarization in Ground-based Observations of Celestial Bodies

Ground and space observations of the bodies of the Solar System (the Moon, regolith surfaces of planets, comets, asteroids, satellites of giant planets, etc.) can provide a huge variety of information about the polarization of light scattered by them in a wide range of phase angles and wavelengths [11]. The phase dependences of brightness and polarization obtained from photopolarimetric observations of celestial bodies have a number of features that can be used to obtain information on the scattering properties of individual particles, their composition, structure, and also on the parameters of the medium. Almost all observed celestial bodies have a negative polarization branch, but the depth, position, and shape of this branch differ markedly for different objects.

Lyot [12] was the first to discover that the disk-integrated polarization of the Moon, as well as its local regions, becomes negative at phase angles of about 23°. In addition, polarimetric observations of the Moon were carried out by many researchers [13,14]. In these works, it was shown that the main properties of the negative branch of polarization for the Moon are as follows:

1) The negative polarization branch for the entire Moon is almost symmetrical with the parameters $P_{min}$ = –1.2%, $\alpha_{min}$ = 11°, $\alpha_{inv}$ = 23.6°;

2) Lunar objects of different morphology have different $P_{min}$ values in the range from –0.6% to –1.4%. Low values of negative polarization are characteristic of light continents, while dark seas have large $P_{min}$;

3) The dependence of $P_{min}$ on the surface albedo for various lunar formations has a horseshoe shape: At low albedos, $P_{min}$ increases with albedo, but then begins to decrease;

4) The absolute value of $P_{min}$ for bright craters does not depend on the wavelength, but slightly increases with increasing wavelength for dark material;

5) The inversion angle slightly increases with increasing wavelength.

Multiple polarimetric observations of the Galilean satellites of Jupiter in UBVR filters at phase angles in the range from 11.8° to almost 0° made it possible to obtain almost all polarimetric information available in the course of ground-based observations of these objects [15-19].

In these works, both phase and longitudinal and spectral dependences of the degree of linear polarization were studied. Some systematic differences have been found in the depth of the negative polarization branch for Io, Europa, Ganymede, and Callisto. Large longitudinal variations in the degree of polarization were found for Callisto and Io, while they were noticeably smaller in the case of Ganymede and Europa. The polarization minima for the trailing hemispheres of Io, Europa, and Ganymede turned out to be systematically higher than for the corresponding leading hemispheres. However, the leading hemisphere of Callisto has noticeably higher polarization values and large $\alpha_{min}$ in all spectral ranges compared to those of the trailing hemisphere. Separation of phase and longitudinal polarization effects was performed for Ganymede [16] and Callisto [20].

In addition, an opposite effect of polarization was found in the form of a sharp increase in negative polarization at extremely small phase angles $\alpha \approx 0.5\text{-}0.7°$ in combination with the usual behavior of the negative branch of the degree of linear polarization for Io, Ganymede and Europa [17,18,21]. This phase angle is comparable to the width of the brightness peak observed for Europa, indicating that both opposition phenomena are likely caused by the backscattering coherent backscattering mechanism [17].

A small number of observations were devoted to measurements of the degree of polarization of three satellites of Saturn: Dione, Iapetus and Rhea [22,23]. The results turned out to be sufficient for estimating the depth of the negative polarization branch, but it was not possible to determine the inversion angle. Rhea and Diona have close $P_{min}$ values close to –0.4%. For Iapetus, the negative branch turned out to be much deeper for the dark leading hemisphere ($P_{min}$ = –1.3%) than for the light trailing hemisphere ($P_{min}$ = –0.2%).

The phase dependence of the degree of linear polarization of comets was measured (for different comets) in the range 0.3-122°. The phase dependence turned out to be smooth, similar to the phase curves of non-atmospheric bodies of the Solar System. All comets exhibit a shallow branch of negative polarization in the backscattering region, first discovered by Kiselev and Chernova [24], which inverts into positive polarization at $\alpha \approx 21°$ with a polarization slope at the inversion point $h \approx 0.2\text{-}0.4\%/°$, after which the positive branch of polarization with a broad maximum at angles $\alpha_{max}$ of about 90°-100° appears as comets. While the minimum value of the degree of linear polarization is usually –2% [25-27], a significant scatter of data for different comets is observed at $\alpha > 40°$. Dlugach et al. [28] and Halder & Ganesh [29] showed that computer simulation of light scattering processes by particles of a heterogeneous structure is able to reproduce the phase curves of the degree of linear polarization of most comets.

Lyot [30] was the first to measure the degree of polarization of light scattered by asteroids. He found that the asteroids 1 Ceres and 4 Vesta show the same negative polarization at low phase angles as the Moon, Mars and Mercury. An extensive program of polarimetric observations has been carried out by Zelner et al. [31], Zellner and Gradie [32] and many other researchers, resulting in the collection of a large amount of polarimetric observational data that can be found in the polarimetric asteroid database①. For asteroids, the negative polarization branches are very diverse. The angle of inversion for different asteroids varies from 16 to 25 degrees. The value of the minimum $|P_{min}|$ for C-type asteroids reaches 2.1%, for E-type asteroids this value is about 0.5%. In the work [33] it was shown that the negative polarization branch of some asteroids, such as asteroid 419 Aurelia, can be reproduced by computer simulation of light scattering by analog of planetary regoliths.

Summing up this section, we can say that the observational data on the degree of linear polarization of objects in the solar system demonstrate a huge variety of phase polarization curves, which indicates a great variety of physical mechanisms for the formation of the negative branch of the degree of linear polarization.

## 3. Models of Negative Polarization Formation

Single particles can produce the negative polarization branch of scattered light. This feature has been repeatedly established both in the course of calculations performed according to the Mie theory [34], in the course of polarimetric observations of cometary atmospheres [35], in measurements of the linear polarization degree of singly scattered light in the laboratory [36,37], and also in the course of computer simulation of light scattered from single particles of irregular shape [38]. It should be noted that a single particle is understood as an object of an arbitrarily complex structure, sufficiently remote from other similar objects. Inside a single particle, acts of multiple scattering of light between its elements can occur, but there is no multiple scattering between different particles, or their contribution is negligible. Let us describe main mechanisms capable of inducing negative polarization in single particles.

### 3.1 Ohman Model

The Ohman model considers double reflections from two mutually perpendicular planes forming a trough, the cross section of which is a right triangle [5]. The emerging negative polarization looks like this: a triangular trough has the well-known property of reflecting light in the strictly opposite direction. When the axis is perpendicular to the scattering plane, it exhibits a trough property, but this property disappears when the axis is parallel to the scattering plane. The chute axis may have an intermediate orientation, resulting in non-zero phase angles. In the case when the axis of the trough is perpendicular to the plane of scattering, the doubly reflected rays have a positive polarization and cannot be observed at nonzero phase angles. On the other hand, when the axis of the trough is parallel to the plane of scattering, the negative polarization of doubly reflected beams predominates, but these beams are also observed at nonzero phase angles. As a general rule, negative polarization should be maintained for all but zero phase angles when averaged over all trough orientations. But, on the other hand, the light reflected once from the trough is positively polarized. Because the negative polarization of light is more noticeable at small phase angles, and the positive polarization of light is more noticeable at large phase angles, the polarization curve shown in Figure 1 can be obtained.

### 3.2 Steigmann Model

The Steigmann model [39,40] uses single and double reflection, approximating the scattering media by cylindrical pits with a flat bottom, where diameter and density are inversely related. The axes of the pits can be tilted from 0° to 90° towards the incident rays. The light undergoes two Fresnel reflections inside the pits, either from the floor and wall, or vice versa. The floor and walls of these pits act as reflectors, as in the Ohman model described earlier. Consequently, such reflections in the pits favor the appearance of negative polarization.

The Steigman model uses parameters such as the surface substance refractive index, the pit radii range, the reflection coefficient, and the depolarization coefficient to model the surface albedo and has shown good agreement with the experimental data of celestial bodies and laboratory studies [41,42]. Unlike the Wolf model (see Section 3.4), Steigman's model does not predict the second branch of negative polarization resulting from shading at significant phase angles. The Steigman model contains non-parabolic theoretical polarization curves, which indicates the variability of the experimental curves, described above.

### 3.3 The Contribution of Multipoles

If the scattering particle is much smaller than wavelength, then it can be considered an electrostatic dipole that scatters light in accordance with Rayleigh's law. The linear polarization degree of scattered light by a Rayleigh particle

① Lupishko, D., Ed. (2022). Asteroid Polarimetric Database V2.0. urn:nasa:pds:asteroid_polarimetric_database::2.0. NASA Planetary Data System. Available from: https://sbn.psi.edu/pds/resource/apd.html

is described by the following well-known formula:

$$P = \frac{1-[\cos\alpha]^2}{1+[\cos\alpha]^2}, \quad (2)$$

where α is phase angle.

This polarization is always positive. However, when the light-scattering object is of considerable size, the participation of multipoles should be taken into account. It is commonly believed that for spherical particles it is multipoles that lead to negative polarization. For particles of arbitrary shape, estimating the multipoles contribution is a rather difficult task. Nevertheless, important results can be achieved for small degrees of multipolarity. It was demonstrated by Shkuratov et al. [43] that the following formula is valid, which describes sum radiation of magnetic dipoles, quadrupoles and ordinary dipoles:

$$P = \frac{[1+(M-D)\cos\alpha]^2 - [M+\cos\alpha - D\cos 2\alpha]^2}{[1+(M-D)\cos\alpha]^2 + [M+\cos\alpha - D\cos 2\alpha]^2}, \quad (3)$$

where M and D are the contribution of the magnetic dipole and quadrupole moments to the total emission compared to the dipole emission. At M = D = 0, Equation (3) turns into Equation (2). Equation (3) can predict the negative polarization branch for certain combinations of D and M, which depend on the size, optical constants, and structure of the light-scattering particles. Figure 2 shows the $\alpha_{inv}$ dependence on the parameters D and M. It can be seen from the figure that combinations of these parameters are quite capable of well describing the actually observed inversion angles from 15 to 30 degrees.

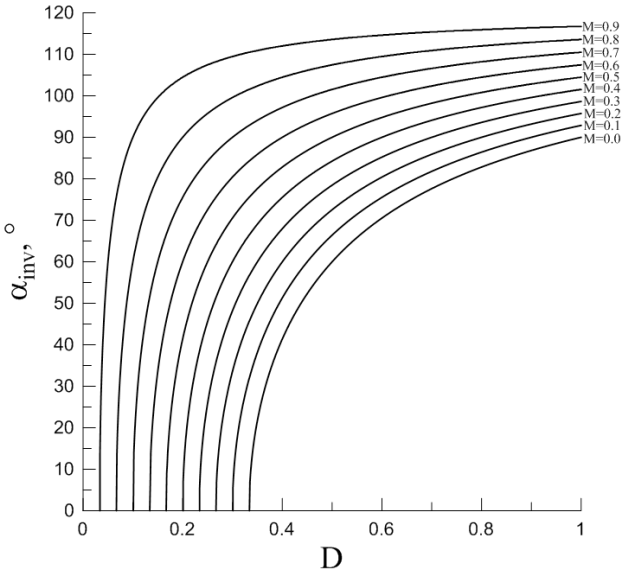


**Figure 2.** The inversion angle ($\alpha_{inv}$) dependence on the parameters D and M of Equation (3).

### 3.4 Wolff Shading Model

Wolff [44] took up the studying of Lyot's first conjecture. He suggested a model that takes into account single and double light scattering [45,46], which, apparently, is in agreement with observations. Wolff studied a scattering medium consisting of particles, but at the same time having a rough surface. He suggested that the shading of a certain proportion of particles due to the roughness of the interface contributes to negative polarization (Figure 3). In particular, Wolff suggested that for positively and negatively polarized pairs of rays (1', 2') and (3', 4'), respectively, the differences in the probability of propagation of rays (ray 2' will leave the medium with a lower probability than the rest of the rays) lead to negative polarization. Due to the peculiarities of light scattering by Rayleigh particles, light scattered along conjugate paths involving particles 3 and 4 is negatively polarized, and scattered along paths involving particles 1 and 2 gives a positive polarization. Because of waves lying in the scattering plane (1-2) are less likely to leave the surface (in particular, wave 2' in Figure 3) than waves in a plane perpendicular to the scattering plane (3-4), negative polarization will dominate.

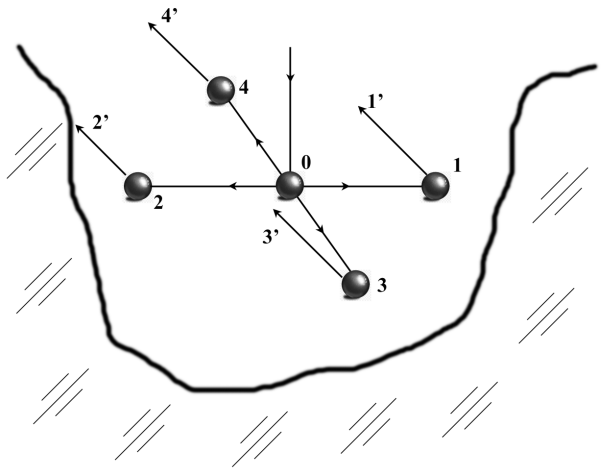


**Figure 3.** Wolff shading model. Wave 2' will leave the medium with a lower probability than the rest of the waves.

The following parameters are used in the Wolf model: The complex refractive index of scattering objects m = n + ik, the ratio of the width to the depth of emptinesses between particles, the average particle size used to calculate the scattering of unpolarized light and the intensity ratio of singly and doubly scattered light, which is influenced by

the structural properties of the scattering medium. Wolff's model has been validated through laboratory tests [47] and applied to explain data from the planets [48,49].

Shkuratov [50] simplified the Wolff shading model under the assumption of a small-angle approximation. For the linear polarization degree, the following equation was obtained:

$$P = C_1\left[\frac{(n-1)^2}{An^2(n+1)^2} + C_2\frac{\left(n^2-1\right)^2}{\left(n^2+1\right)^2}\right]\alpha^2 - C_3\frac{\left(n^2-1\right)^2}{\left(n^2+1\right)^2}\alpha, \quad (4)$$

where A is the geometric albedo of the surface, n is a real part of refractive index, $C_1$, $C_2$ and $C_3$ are parameters describing the asymmetry of beams 1-4 due to shading (Figure 3). Equation (4) is applicable only for sufficiently small phase angles $\alpha < 30°$.

### 3.5 McCoyd Model

Consider a medium formed by a complex, large-scale structure. In scattered light, two components can be distinguished—on the surface layer there is one reflection, and in the depth of the layer there are multiple refractions and reflections. McCoyd [6] investigated the polarization of light reflected and refracted both outside and inside a layer having a rough surface and a smooth lower boundary separating this layer from another layer, less optically dense. Using the assumption of Fresnel reflection coefficients, the Monte Carlo method was used for calculations.

McCoyd suggested that the negative polarization might be the result of total internal reflection at the bottom interface between the layers and refraction at the top interface. However, this model is not suitable for interpreting observations of extra-atmospheric celestial bodies and laboratory measurements, as was shown by Shkuratov et al. [51].

### 3.6 Hopfield Model

Hopfield [7] assumed that shadowing in a scattering medium composed of dust particles could explain the negative polarization through the Sommerfeld diffraction mechanism. The edges of dust grains are considered to be fine half-planes of an ideal conductor, and in the shadow zone below them, a diffracted electromagnetic field with negative polarization is reflected to the observer by scattering surface elements lying under them.

Hopfield's calculations suggest that the Moon's minimum polarization (–1.2%) may be due to tiny 5 μm particles located close together, although it is not clear if the equations used are appropriate for lunar particles. On the one hand, an electromagnetic field diffracted by a half-plane at a distance of several wavelengths has not only a transverse, but also a longitudinal component of the electromagnetic field. For this reason, it is not entirely clear whether it can be described by the usual linear polarization degree.

On the contrary, it was shown that the diffracted field in the wave zone at diffraction angles greater than 5° has a negative polarization in visible [52-55] and radio wave part of the spectrum [58]. However, the diffracted component intensity is relatively low, so the contribution of this mechanism to the resulting negative polarization is small.

## 4. Coherent Backscattering Enhancement

Interference mechanisms for the formation of negative polarization seem to be the most hopeful, since they are based on the universal multiple scattering mechanism, which takes place in any sufficiently dense medium of scattering particles.

The effect of coherent backscattering (also sometimes referred to in the literature as the "effect of weak localization") of light in discrete random medium was first described by Watson [56]. It is still under active theoretical and laboratory research [57-61]. To find out how the brightness opposition effect is caused by interference, we examine a discrete medium consisting of scattering particles randomly scattered and exposed to a plane wave. We will focus on two backward (conjugate) scattering paths that include the same particle configuration. When the waves scatter, their interference can be constructive or destructive depending on the phase difference between their paths. If the observer is not directly in the backscattering direction, the interference effect is zero due to the random position of the particles. This creates an incoherent intensity. However, when the observer is exactly in the backscattering direction ($\alpha = 0°$), coherence is preserved and the interference is always constructive, resulting in the opposite peak in the intensity of the scattered radiation.

Shkuratov [62,63] was the first to propose a coherent backscattering polarization mechanism. A little later, independently of him, the same mechanism was described by Muinonen [64].

To understand the polarization opposition effect, imagine small particles 1-4 in a plane perpendicular to the direction of the light (see Figure 4). If the incident light is unpolarized, it can be represented as a mixture of two linearly polarized beams. Rayleigh particles (much smaller than the wavelength) scatter light in a plane perpendicular to the incident radiation, with polarized light perpendicular to the scattering plane. Particles 3 and 4 scatter negatively polarized light along conjugated paths, while particles 1 and 2 scatter positively polarized light. Coherent backscattering amplifies the negative polarization contribution at small phase angles, resulting in a

negative polarization branch comparable to the brightness opposition effect. The polarization opposition effect is less pronounced than the brightness opposition effect due to the fact that certain particle configurations contribute to it.

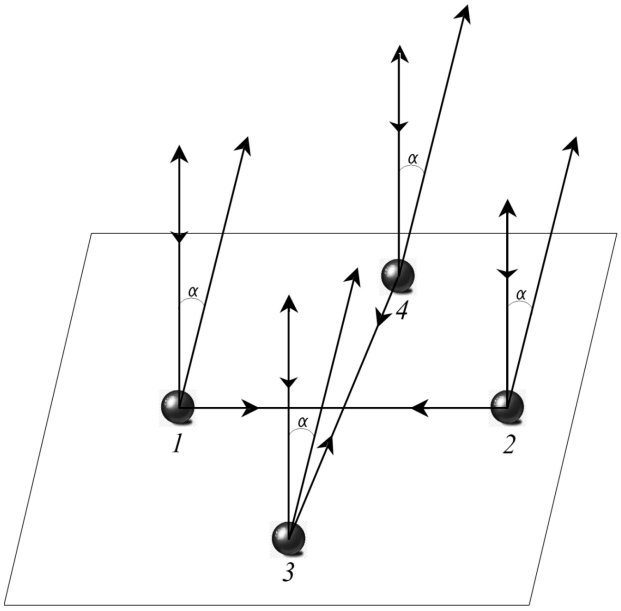


**Figure 4.** Model of coherent backscattering enhancement. Waves (3-4) and (4-3) always interfere constructively, while waves (1-2) and (2-1) at non-zero phase angles interference can be constructive or destructive depending on the phase difference between their paths.

It should also be mentioned that this mechanism predicts the presence of negative polarization at big phase angles near 180°, since all above considerations, which are valid for the phase angle α, are also valid for the phase angle 180 – α. Despite technical difficulties in measuring the large phase angles polarization, some laboratory polarimetric measurements have shown that negative polarization there is at phase angles α > 170° [65,66]. However, it should be noted that negative polarization at big phase angles is observed in a much narrower range of angles than at small phase angles. This fact suggests that one mechanism of coherent backscattering enhancement cannot explain all the features of scattering, and, most likely, several mechanisms operate simultaneously.

## 4.1 Model of Double Scattering by a Set of Point Scatterers

Any scattering particle can be described as a number of point scatterers interacting with each other. Therefore, it is logical to try to describe such an interaction theoretically.

The simplest model was developed by Muinonen [64], who considered double scattering between two particles representing electric dipoles. When averaging the second-order scattering matrix over uniformly distributed particles, it was found that a strong negative polarization accompanies the oppositional brightness peak at small phase angles. The value of negative polarization is extremely sensitive to the average distance between particles. However, since dipole particles have a small scattering cross section, the negative polarization and opposition peak disappear when the combined first and second order scattering is considered. However, replacing the dipole scatterer with a dielectric half-space somewhat increases the contribution of second-order scattering [67].

Muinonen investigated the reflection of waves from two curved surfaces [68] and found negative polarization when considering the phase of an electromagnetic field, which cast doubt on Wolf's shading model (Section 3.4).

Shkuratov [69] developed a more general model of light scattering by a set of point scatterers. He considered a medium consisting of little (quasi-Rayleigh) scattering objects restrained by flat interface. The characteristics of the particle were the single-scattering albedo ω, the polarimetrical phase function P(α), and r/λ is the ratio of the average particle size to wavelength. The bulk density of scattering objects is equal to ξ. The model took into account only single and double scattering of light in a medium, which was calculated using the theory of radiative transfer [70-72]. However, despite these assumptions, the expressions for the linear polarization degree turned out to be too complicated [73]. As a result, additional assumptions were made: the phase dependence of single scattering was assumed to be isotropic, and the phase dependence of a quasi-Rayleigh particle was described by the formula $f(\alpha)=G\frac{1-(\cos\alpha)^2}{1+(\cos\alpha)^2}$, where G is the polarimetric scale factor (0 < G < 1). These assumptions made it possible to obtain rather simple relations [73]:

$$P(\alpha)=G\frac{\left(1+2\sqrt{1-\omega}\right)^2}{9}\left(\frac{\sin^2\alpha}{1+\cos^2\alpha}+\frac{2\omega\xi\left[1-\sqrt{1+\left(\frac{8}{5}\rho\sin\frac{\alpha}{2}\right)^2}\right]}{\left(\frac{8}{5}\rho\sin\frac{\alpha}{2}\right)^2\sqrt{1+\left(\frac{8}{5}\rho\sin\frac{\alpha}{2}\right)^2}\ln(1-\xi)}\right) \quad (5)$$

where $\rho=\frac{8\pi r\cdot\ln(1-\xi)}{3\lambda}$, r is the average particle size, λ is wavelength, ξ is bulk density of scattering objects, ω is single-scattering albedo. When deriving Equation (5), it was also assumed that shading has the same effect on double and single scattering. The second and first order polarization originates due to scattering objects that form the surface relief. For certain sets of parameters, Equation (5) describes quite well the symmetric branch of negative polarization, which is characteristic of many celestial objects, such as the Moon [2], comets [74], or asteroids [75].

### 4.2 Vector Theory of Coherent Backscatter Enhancement

The first attempt to carry out a theoretical calculation of the opposition effect of polarization, based on the coherent backscattering vector theory, was carried out by Mishchenko [76]. It was based on formulas obtained by Ozrin [77] for a semi-infinite medium consisting of Rayleigh scattering objects with zero absorption. Despite the thoroughness of the theory, the final result gave only asymptotic expressions applicable to extremely small and large phase angles. Thus, the full effect of the angular polarization opposition, including the exact position and magnitude of the polarization minimum, remained unknown. However, later an exact solution was obtained [78], subsequently adapted to the Stokes vectors formalism [79].

Authors considered a semi-infinite homogeneous random medium consisting of Rayleigh scattering objects with zero absorption, using the standard set of Stokes parameters to determine the polarization state of the scattered and incident light in meridional planes (the planes containing the scattering object, the light source, and the perpendicular to the boundary environment) [80]. It was assumed that the matrix of scattering is as follows:

$$\text{-ORDER POINT-S}\,\mathbf{F}(\alpha)=\begin{bmatrix} F_{11}(\alpha) & F_{12}(\alpha) & 0 & 0 \\ F_{21}(\alpha) & F_{22}(\alpha) & 0 & 0 \\ 0 & 0 & F_{33}(\alpha) & 0 \\ 0 & 0 & 0 & F_{44}(\alpha) \end{bmatrix}, \quad (6)$$

where $F_{ij}(\alpha)$ are elements of scattering matrix, depending on phase angle α.

$\mathbf{F}(\alpha)$ can be represented as the sum of following terms:

$$\mathbf{F}(\alpha)=\mathbf{F}^{1}(\alpha)+\mathbf{F}^{L}(\alpha)+\mathbf{F}^{C}(\alpha), \quad (7)$$

where $\mathbf{F}^{1}(\alpha)$ takes into account the contribution of single scattering, $\mathbf{F}^{L}(\alpha)$ represents 2nd order or higher ladder scatterplots and $\mathbf{F}^{C}(\alpha)$ represents 2nd order or higher cyclic scatterplots. To simplify the analysis at small phase angles, the angular parameter $q = k/\alpha$ is introduced, where $l$ is the mean free path of photons in the scattering medium and k is the wavenumber. As a result, the following relations are obtained for these matrices:

$$\mathbf{F}^{1}(\alpha)\approx\mathbf{F}^{1}(0)=\frac{3}{16}\begin{bmatrix} 1 & 0 & 0 & 0 \\ 0 & 1 & 0 & 0 \\ 0 & 0 & -1 & 0 \\ 0 & 0 & 0 & -1 \end{bmatrix}, \quad (8)$$

$$\mathbf{F}^{L}(\alpha)\approx\mathbf{F}^{L}(0)=\frac{1}{4}\begin{bmatrix} \gamma_{11}(0)+\gamma_{12}(0) & 0 & 0 & 0 \\ 0 & \gamma_{11}(0)-\gamma_{12}(0) & 0 & 0 \\ 0 & 0 & \gamma_{12}(0)-\gamma_{11}(0) & 0 \\ 0 & 0 & 0 & \gamma_{44}(0) \end{bmatrix}-\mathbf{F}^{1}(0), \quad (9)$$

$$\mathbf{F}^{C}(\alpha)\approx\mathbf{F}^{C}(q)=\begin{bmatrix} F_{11}^{C}(q) & F_{12}^{C}(q) & 0 & 0 \\ F_{12}^{C}(q) & F_{22}^{C}(q) & 0 & 0 \\ 0 & 0 & F_{33}^{C}(q) & 0 \\ 0 & 0 & 0 & F_{44}^{C}(q) \end{bmatrix}-\mathbf{F}^{1}(0), \quad (10)$$

where

$$F_{11}^{C}(q)=\frac{1}{8}\left[\gamma_{11}(q)+\gamma_{22}(q)-\gamma_{33}(q)+\gamma_{44}(q)\right], \quad (11)$$

$$F_{22}^{C}(q)=\frac{1}{8}\left[\gamma_{11}(q)+\gamma_{22}(q)+\gamma_{33}(q)-\gamma_{44}(q)\right], \quad (12)$$

$$F_{33}^{C}(q)=\frac{1}{8}\left[\gamma_{33}(q)+\gamma_{44}(q)\right]-\frac{1}{4}\gamma_{12}(q), \quad (13)$$

$$F_{44}^{C}(q)=\frac{1}{8}\left[\gamma_{33}(q)+\gamma_{44}(q)\right]+\frac{1}{4}\gamma_{12}(q), \quad (14)$$

$$F_{12}^{C}(q)=\frac{1}{8}\left[\gamma_{11}(q)-\gamma_{22}(q)\right], \quad (15)$$

where $\gamma_{ij}(q)$—angular functions.

Explicit expressions for $\gamma_{ij}(q)$ are unknown, but they can be calculated numerically, in accordance with the special procedure [78]. Using the above relations, one can obtain the all Stokes matrix at any values of q. If, in addition, we know $l$, the Stokes matrix can be represented as a function of α rather than q. And knowing the Stokes matrix, it is easy to calculate the linear polarization degree:

$$P(\alpha)=-\frac{Q(\alpha)}{I(\alpha)}=-\frac{F_{12}^{C}(q)}{F_{11}^{1}(0)+F_{11}^{L}(0)+F_{11}^{C}(q)}. \quad (16)$$

It was shown by Mishchenko et al. [79] that, in accordance with this theory, the coherent enhancement of backscattering induces a rather narrow and highly asymmetric negative polarization branch, similar to the negative polarization branches observed for a number of celestial bodies, such as the rings of Saturn [76] and Galilean satellites Jupiter [19].

## 5. Effects of Near Field

When a particle or system of particles close in size to the wavelength is nearby, the wave becomes highly non-uniform due to the delay of the electromagnetic wave inside the particle compared to the incident wave. In such a wave, the surfaces of constant phase and amplitude do not coincide, and the amplitude, polarization, and direction of propagation depend on the position relative to the scatterer. According to the Lorentz-Mie theory, calculations for spherical particles show that the surface of the constant phase of the wave takes the form of a funnel near the particle if its size is close to the wavelength [81]. Thus, neighboring particles are affected by the variegated field

and therefore scattered light exhibits special features. It was shown by Petrova et al. [82] that the rotation of the field vector in the proximity of the particle reduces the scattering intensity in the backscattering and forward scattering regions and causes negative polarization. These features of light scattering are called "near field effects" [83].

The near field effect is effective in densely packed environments at various angles. However, for large scatterers in homogeneous and isotropic media, it becomes negligible, since the inhomogeneity scale is similar to the wavelength. Similarly, if the scatterers are smaller than the wavelength, the near field effect can also be neglected due to the small wave inhomogeneity.

The effectiveness of the near field effect is highest in media with scatterers close to the wavelength, or in polydisperse media, where larger particles cause wave inhomogeneities for smaller particles. Further investigation shows that the effect of the near field effect is highly dependent on particle size, refractive index, interparticle spacing, and phase angle [84].

However, the realism of this mechanism is called into question by some researchers [85]. In particular, they pointed out that the name of this effect was chosen poorly, because in the classical literature [86] the "near field" is a field whose amplitude decreases faster than 1/*r*, where r is the distance to the wave source. In the description of this mechanism, the near field is understood as any field in the immediate proximity of the scattering particle. In addition, the field near the particle is the result of the interference of the scattered and incident radiation, as a result of which this field has both a longitudinal and a transverse component. And in the course of describing the effect of near field, only the transverse component of the electromagnetic field is considered, while the longitudinal component is ignored. Thus, the description of this mechanism is at least incomplete.

Also measurements of the linear polarization degree in the laboratory of a medium consisting of hematite particles 1-2 μm in size were carried out [85]. Previous laboratory measurements of individual particles of hematite [36] showed the existence of a negative branch of polarization. While in a medium consisting of such particles, negative polarization was not found at all, which contradicts the assertions that near-field effects enhance negative polarization.

Also a light scattering computer simulation for particles cluster was carried out using the method of discrete-dipole approximations [85]. It was shown by Petrova et al. [82] that taking into account double scattering leads to the appearance of negative polarization even in the case when the singly scattered light is positively polarized. Computer simulation was carried out for particles of the same parameters (sizes and refractive indices), but taking into account all scattering orders. And as a result, negative polarization could not be detected.

However, it was shown by Petrova et al. [87] that the experimental data and model calculations described by Shkuratov and Zubko [85] do not disprove the significance of the influence of the near field on scattering mechanisms. The backscattering coherent enhancement works on sparse media, while the near field effect appears in very densely packed media. For this reason, it cannot be concluded that the near field effects are insignificant in the surface layer of a dark scattering medium. Although the effect of coherent backscattering is well known, the theory of the near field effect is not yet complete and its contribution to backscattering is still difficult to quantify. Despite these problems, Petrova et al. [87] stated that the near field effect is indeed a workable mechanism and cannot be triggered due to the discovery of dense media in studies.

## 6. Conclusions

The paper presents a literature review of the main mechanisms, the cumulative action of which explains the occurrence of the negative branch of the linear polarization degree of scattered light. The paper discusses the results of ground-based observations of the negative branch of the degree of linear polarization for various objects of the solar system. Scattering by single particles, shadow effect, coherent backscattering enhancement, and effects of near field are considered. The advantages and disadvantages of each of the described mechanisms are considered in detail. The review will be useful to all researchers studying the scattering of light by celestial bodies.

## Funding

Work is supported by the Ministry of Science and Higher Education of the RF (grant 075-15-2020-780).

## Acknowledgment

Author acknowledges the support from the Ministry of Science and Higher Education of the RF (grant 075-15-2020-780).

## Data Availability Statement

The data that support the findings of this study are available from the author, upon reasonable request.

## Conflict of Interest

There is no conflict of interest.

## References


[1] Shkuratov, Y., Ovcharenko, A., Zubko, E., et al., 2002. The opposition effect and negative polarization of structural analogs for planetary regoliths. Icarus. 159(2), 396-416.

[2] Lyot, B., 1929. Recherches sur la polarisation de la lumiere des planetes et de queldues substances terrestres (French) [Research on the polarization of the light of planets and certain terrestrial substances]Ann Obs Meudon. 8, 1-161.

[3] Bowell, E., Dollfus, A., Geake, J.E., 1972. Polarimetric properties of the lunar surface and its interpretation. Part 5: Apollo 14 and Luna 16 lunar samples. Proceedings of the Lunar Science Conference. 3, 3103.

[4] Ovcharenko, A.A., Shkuratov, Y.G., 2000. Weak-localization effect for light backscattered by surfaces with a complex structure. Optics and Spectroscopy. 88, 253-259.

[5] Ohman Y., 1955. A tentative explanation of the polarization in diffuse reflection. Stockholm Observatory Annual. 18, 1-10.

[6] McCoyd, G.C., 1967. Polarization properties of a simple dielectric rough-surface model. Journal of the Optical Society of America. 57(11), 1345-1350.

[7] Hopfield, J.J., 1966. Mechanism of lunar polarization. Science. 151(3716), 1380-1381.

[8] Veverka J., 1977. Polarimetry of satellite surfaces. Planetary satellites. University of Arizona Press: Tucson. pp. 210-231.

[9] Petrova, E.V., Tishkovets, V.P., 2011. Light scattering by morphologically complex objects and opposition effects (a review). Solar System Research. 45(4), 304.

[10] Noebauer, U.M., Sim, S.A., 2019. Monte Carlo radiative transfer. Living Reviews in Computational Astrophysics. 5, 1-103.

[11] Mishchenko, M.I., Rosenbush, V.K., Kiselev, N.N., et al., 2010. Polarimetric remote sensing of solar system objects. arXiv preprint arXiv:1010.1171.

[12] Lyot, B., 1964. Research on the polarization of light from planets and from some terrestrial substances. National Aeronautics and Space Administration: Washington.

[13] Coyne, G.V., Pellicori, S.F., 1970. Wavelength dependence of polarization. xx. the integrated disk of the moon. Astronomical Journal. 75, 54.

[14] Dollfus, A., Bowell, E., 1971. Polarimetric properties of the lunar surface and its interpretation. Part I. Telescopic observations. Astronomy and Astrophysics. 10, 29.

[15] Veverka, J., 1971. Polarization measurements of the Galilean satellites of Jupiter. Icarus. 14(3), 355-359.

[16] Dollfus, A., 1975. Optical polarimetry of the Galilean satellites of Jupiter. Icarus. 25(3), 416-431.

[17] Rosenbush, V.K., Avramchuk, V.V., Rosenbush, A.E., et al., 1997. Polarization properties of the Galilean satellites of Jupiter: Observations and preliminary analysis. The Astrophysical Journal. 487(1), 402.

[18] Rosenbush, V.K., Kiselev, N.N., Jockers, K., et al., 2000. Optical polarimetry of the Galilean satellites, Iapetus, and 64 Angelina near opposition. Kinematika i Fizika Nebesnykh Tel Supplement. 3, 227-230.

[19] Kiselev, N., Rosenbush, V., Muinonen, K., et al., 2022. New polarimetric data for the galilean satellites: Europa observations and modeling. The Planetary Science Journal. 3(6), 134.

[20] Rosenbush, V.K., 2002. The phase-angle and longitude dependence of polarization for Callisto. Icarus. 159(1), 145-155.

[21] Rosenbush, V.K., Kiselev, N.N., 2005. Polarization opposition effect for the Galilean satellites of Jupiter. Icarus. 179(2), 490-496.

[22] Zellner, B., 1972. Minor planets and related objects. VIII. Deimos. The Astronomical Journal. 77, 183.

[23] Bowell, E., Zellner, B., 1974. Polarizations of asteroids and satellites. University Arizona Press: Tucson. pp. 381-404.

[24] Kiselev, N.N., Chernova, G.P., 1981. Phase functions of polarization and brightness and the nature of cometary atmosphere particles. Icarus. 48(3), 473-481.

[25] Mukai, S., Mukai, T., Kikuchi, S. (editors), 1991. Scattering properties of cometary dust based on polarimetric data. Origin and Evolution of Interplanetary Dust: Proceedings of the 126th Colloquium of the International Astronomical Union; 1990 Aug 27-30; Kyoto. Netherlands: Springer. p. 249-252.

[26] Chernova, G.P., Kiselev, N.N., Jockers, K., 1993. Polarimetric characteristics of dust particles as observed in 13 comets: Comparisons with asteroids. Icarus. 103(1), 144-158.

[27] Levasseur-Regourd, A.C., Hadamcik, E., Renard, J.B., 1996. Evidence for two classes of comets from their polarimetric properties at large phase angles. Astronomy and Astrophysics. 313, 327-333.

[28] Dlugach, J.M., Ivanova, O.V., Mishchenko, M.I., et al., 2018. Retrieval of microphysical characteristics of particles in atmospheres of distant comets from ground-based polarimetry. Journal of Quantitative

Spectroscopy and Radiative Transfer. 205, 80-90.
[29] Halder, P., Ganesh, S., 2021. Modelling heterogeneous dust particles: An application to cometary polarization. Monthly Notices of the Royal Astronomical Society. 501(2), 1766-1781.
[30] Lyot, B., 1934. Polarisation des petites planets (French) [Polarization of minor planets]. Comptes Rendus de l'Académie des Sciences. 199, 774.
[31] Zellner, B., Gehrels, T., Gradie, J., 1974. Minor planets and related objects. XVI-Polarimetric diameters. The Astronomical Journal. 79, 1100-1110.
[32] Zellner, B., Gradie, J., 1976. Polarization of the reflected light of asteroid 433 Eros. Icarus. 28(1), 117-123.
[33] Grynko, Y., Shkuratov, Y., Alhaddad, S., et al., 2022. Negative polarization of light at backscattering from a numerical analog of planetary regoliths. Icarus. 384, 115099.
[34] Bohren, C.F., Huffman, D.R., 1998. Absorption and scattering of light by small particles. Wiley-VCH: Weinheim.
[35] Kiselev, N.N., Chernova, G.P., 1976. On a possible new version of the polarization-phase relation for comets. Astronomicheskij Tsirkulyar. 931, 5-7.
[36] Muñoz, O., Volten, H., Hovenier, J.W., et al., 2006. Experimental and computational study of light scattering by irregular particles with extreme refractive indices: Hematite and rutile. Astronomy & Astrophysics. 446(2), 525-535.
[37] Muñoz, O., Hovenier, J.W., 2011. Laboratory measurements of single light scattering by ensembles of randomly oriented small irregular particles in air. A review. Journal of Quantitative Spectroscopy and Radiative Transfer. 112(11), 1646-1657.
[38] Zubko, E., Petrov, D., Shkuratov, Y., et al., 2005. Discrete dipole approximation simulations of scattering by particles with hierarchical structure. Applied Optics. 44(30), 6479-6485.
[39] Steigmann, G.A., 1978. A polarimetric model for a dust-covered planetary surface. Monthly Notices of the Royal Astronomical Society. 185(4), 877-888.
[40] Steigmann, G.A., 1984. Application of a polarimetric model to the surface microstructure of particles in the B-ring of Saturn. Monthly Notices of the Royal Astronomical Society. 209(2), 359-371.
[41] Steigmann, G.A., 1986. Optical polarimetry of sulphur and the surface microstructure of Io. Monthly Notices of the Royal Astronomical Society. 219(4), 823-833.
[42] Steigmann, G.A., Dodsworth, M.B., 1987. Surface microstructure of the nucleus of Comet P/Halley. The Observatory. 107, 263-267.
[43] Shkuratov, Y.G., Muinonen, K., Bowell, E., et al., 1994. A critical review of theoretical models of negatively polarized light scattered by atmosphereless solar system bodies. Earth Moon and Planets. 65(3), 201-246.
[44] Wolff, M., 1975. Polarization of light reflected from rough planetary surface. Applied Optics. 14(6), 1395-1405.
[45] Wolff, M., 1980. Theory and application of the polarization-albedo rules. Icarus. 44(3), 780-792.
[46] Wolff, M., 1981. Computing diffuse reflection from particulate planetary surface with a new function. Applied Optics. 20(14), 2493-2498.
[47] Geake, J.E., Geake, M., Zellner, B.H., 1984. Experiments to test theoretical models of the polarization of light by rough surfaces. Monthly Notices of the Royal Astronomical Society. 210(1), 89-112.
[48] Dollfus, A., Wolff, M. (editors), 1981. Theory and application of the negative branch of polarization for airless planetary objects. Lunar and Planetary Science Conference; 1981 Mar 16-20; Houston. p. 232-234.
[49] Dollfus, A., Wolff, M., Geake, J.E., et al., 1989. Photopolarimetry of asteroids. Asteroids Ii. 594-616.
[50] Shkuratov, Y.G., 1982. A model for negative polarization of light by cosmic bodies without atmospheres. Soviet Astronomy. 26, 493-496.
[51] Shkuratov, I.G., Kreslavskii, M.A., Opanasenko, N.V., 1992. Analysis of a mechanism of the negative polarization of light scattered by atmosphereless celestial bodies. Astronomicheskii Vestnik. 26, 46-53.
[52] Jentzsch, F., 1927. Über die Beugung des Lichtes an Stahlschneiden (German) [On the diffraction of light on steel cutting edges]. Annalen der Physik. 389(18), 292-312.
[53] Wolfsohn G., 1928. Strenge theorie der interferenz und beugung (German) [Strict theory of interference and diffraction]. Handbuch der Physik. Springer Verlag: Berlin. pp. 263-316.
[54] Savornin, J., 1939. Étude de la diffraction éloignée (French) [Study of distant diffraction]. Annales de Physique. 11(11), 129-255.
[55] Horton, C.W., Watson, R.B., 1950. On the diffraction of radar waves by a semi-infinite conducting screen. Journal of Applied Physics. 21(1), 16-21.
[56] Watson, K.M., 1969. Multiple scattering of electromagnetic waves in an underdense plasma. Journal of Mathematical Physics. 10(4), 688-702.

[57] Akkermans, E., Wolf, P.E., Maynard, R., et al., 1988. Theoretical study of the coherent backscattering of light by disordered media. Journal de Physique. 49(1), 77-98.

[58] Barabanenkov, Y.N., Kravtsov, Y.A., Ozrin, V.D., et al., 1991. II enhanced backscattering in optics. Progress in optics. 29, 65-197.

[59] Mishchenko, M.I., Dlugach, J.M., Liu, L., 2009. Azimuthal asymmetry of the coherent backscattering cone: Theoretical results. Physical Review A. 80(5), 053824.

[60] Zhou, C., 2018. Coherent backscatter enhancement in single scattering. Optics Express. 26(10), A508-A519.

[61] Gorodnichev, E.E., Kondratiev, K.A., Rogozkin, D.B., 2022. Coherent backscattering of light from a Faraday medium. Physical Review B. 105(10), 104208.

[62] Shkuratov, Y.G., 1985. On opposition brightness surge and light negative polarization of solid cosmic surfaces. Astronomicheskij Tsirkulyar. 1400, 1.

[63] Shkuratov, I.G., 1988. The nature of the polarimetric inhomogeneity of the surface of the asteroid 4 Vesta. Astronomicheskii Vestnik. 22, 152-158.

[64] Muinonen, K. (editor), 1989. Electromagnetic scattering by two interacting dipoles. The 1989 URSI International Symposium on Electromagnetic Theory; 1989 Aug 14-17; Stockholm. p. 428-430.

[65] Frattin, E., Muñoz, O., Moreno, F., et al., 2019. Experimental phase function and degree of linear polarization of cometary dust analogues. Monthly Notices of the Royal Astronomical Society. 484(2), 2198-2211.

[66] Muñoz, O., Moreno, F., Gómez-Martín, J.C., et al., 2020. Experimental phase function and degree of linear polarization curves of millimeter-sized cosmic dust analogs. The Astrophysical Journal Supplement Series. 247(1), 19.

[67] Muinonen, K.O., Sihvola, A.H., Lindell, I.V., et al., 1991. Scattering by a small object close to an interface. II. Study of backscattering. Journal of the Optical Society of America A. 8(3), 477-482.

[68] Muinonen K., 1990. Light scattering by inhomogeneous media: Backward enhancement and reversal of linear polarization [PhD thesis]. Helsinki: University of Helsinki.

[69] Shkuratov, I.G., 1991. An interference model of the negative polarization of light scattered by solid surfaces of celestial bodies. Astronomicheskii Vestnik. 25, 152-161.

[70] Hapke, B.W., 1963. A theoretical photometric function for the lunar surface. Journal of Geophysical Research. 68(15), 4571-4586.

[71] Hapke, B., 1993. Theory of reflectance and emittance spectroscopy. Cambridge University Press: Cambridge.

[72] Hapke, B., 2008. Bidirectional reflectance spectroscopy: 6. Effects of porosity. Icarus. 195(2), 918-926.

[73] Shkuratov, Y.G., Melkumova, L.Y., 1991. Diffraction model of the negative polarization of light scattering by atmosphereless cosmic bodies. Lunar and Planetary Science Conference. 22, 1243.

[74] Zhuzhulina, E., Petrov, D., Kiselev, N., et al., 2022. Aperture polarimetry of selected comets in 2018-2020: Observations and computer simulation. Journal of Quantitative Spectroscopy and Radiative Transfer. 290, 108321.

[75] Petrov, D., Kiselev, N., 2018. Computer simulation of position and maximum of linear polarization of asteroids. Journal of Quantitative Spectroscopy and Radiative Transfer. 204, 88-93.

[76] Mishchenko, M.I., 1993. On the nature of the polarization opposition effect exhibited by Saturn's rings. The Astrophysical Journal. 411, 351-361.

[77] Ozrin, V.D., 1992. Exact solution for coherent backscattering of polarized light from a random medium of Rayleigh scatterers. Waves in Random Media. 2(2), 141.

[78] Amic, E., Luck, J.M., Nieuwenhuizen, T.M., 1997. Multiple Rayleigh scattering of electromagnetic waves. Journal de Physique I. 7(3), 445-483.

[79] Mishchenko, M.I., Luck, J.M., Nieuwenhuizen, T.M., 2000. Full angular profile of the coherent polarization opposition effect. Journal of the Optical Society of America A. 17(5), 888-891.

[80] Mishchenko, M.I., 1996. Diffuse and coherent backscattering by discrete random media-I. Radar reflectivity, polarization ratios, and enhancement factors for a half-space of polydisperse, nonabsorbing and absorbing spherical particles. Journal of Quantitative Spectroscopy and Radiative Transfer. 56(5), 673-702.

[81] Tishkovets, V.P., 1998. Backscattering of light by close-packed systems of particles. Optics and Spectroscopy. 85(2), 212-217.

[82] Petrova, E.V., Tishkovets, V.P., Jockers, K., 2007. Modeling of opposition effects with ensembles of clusters: Interplay of various scattering mechanisms. Icarus. 188(1), 233-245.

[83] Tishkovets, V.P., 2008. Light scattering by closely packed clusters: Shielding of particles by each other

in the near field. Journal of Quantitative Spectroscopy and Radiative Transfer. 109(16), 2665-2672.

[84] Tishkovets, V., Litvinov, P., Petrova, E., et al., 2005. Backscattering effects for discrete random media: theoretical results. Photopolarimetry in remote sensing. Springer: Netherlands. pp. 221-242.

[85] Shkuratov, Y.G., Zubko, E.S., 2008. Comment on "Modeling of opposition effects with ensembles of clusters: Interplay of various scattering mechanisms" by Elena V. Petrova, Victor P. Tishkovets, Klaus Jockers, 2007 [Icarus 188, 233-245]. Icarus. 194(2), 850-852.

[86] Born, M., Wolf, E., 1999. Principles of optics. Cambridge University Press: Cambridge.

[87] Petrova, E.V., Tishkovets, V.P., Jockers, K., 2008. Rebuttal to comment on "Modeling of opposition effects with ensembles of clusters: Interplay of various scattering mechanisms" by Elena V. Petrova, Victor P. Tishkovets, Klaus Jockers, 2007 [Icarus 188, 233-245]. Icarus. 194(2), 853-856.

NASS
NAN YANG ACADEMY OF SCIENCES

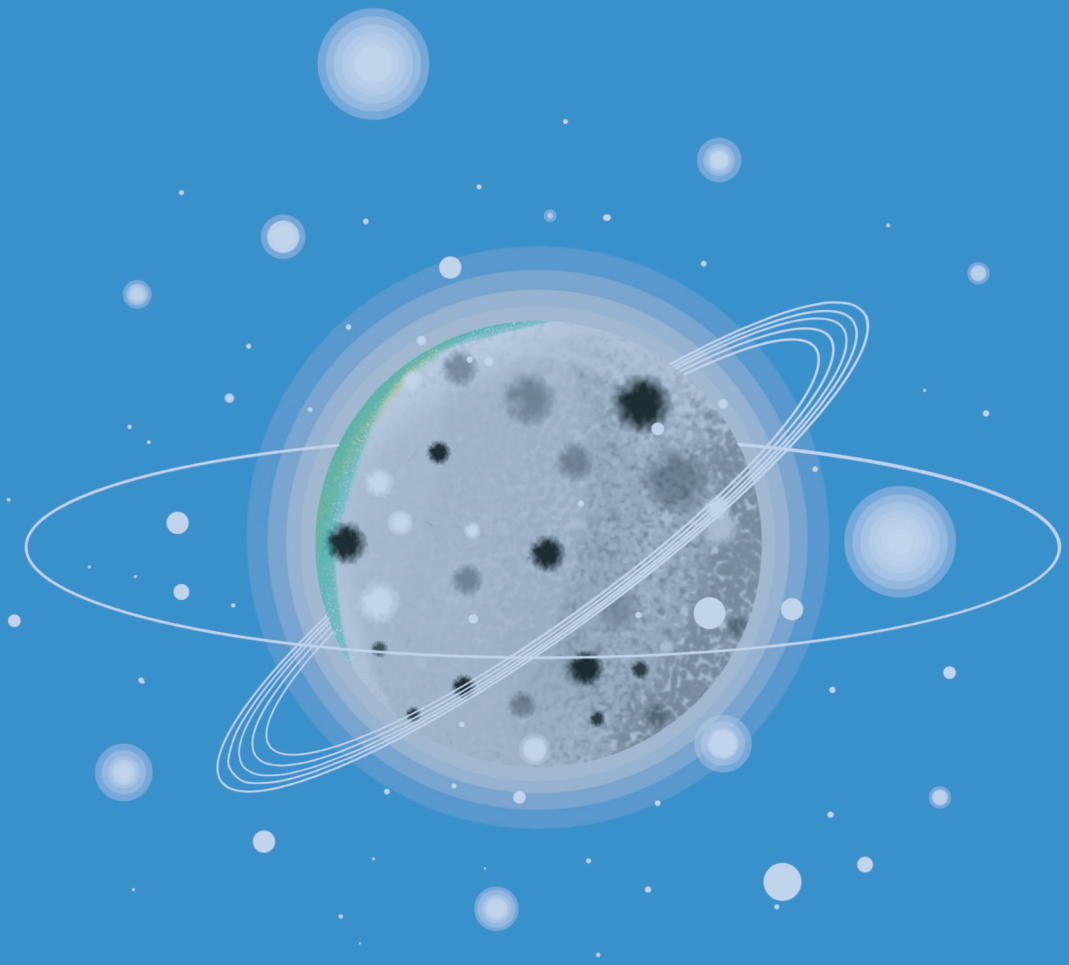

2810-9732
01
9 772810 973232

Tel.: +65 65881289
E-mail: eps@nassg.org
Website: ojs.nassg.org
Add.: 12 Eu Tong Sen Street #07-169 Singapore 059819